12-2008

Fluorescent conjugated polymer dots for single molecule imaging and sensing applications

Changfeng Wu
Clemson University, cwu@clemson.edu

FLUORESCENT CONJUGATED POLYMER DOTS FOR SINGLE MOLECULE IMAGING AND SENSING APPLICATIONS

A Dissertation
Presented to
the Graduate School of
Clemson University

In Partial Fulfillment
of the Requirements for the Degree
Doctor of Philosophy
Chemistry

---

by
Changfeng Wu
December 2008

Accepted by:
Jason McNeill, Committee Chair
Steven Stuart
Kenneth Christensen
Dvora Perahia

ABSTRACT

While single molecule imaging and sensing hold the promise of providing unprecedented detail about cellular processes, many advanced applications are limited by the lack of appropriate fluorescence probes. In many cases, currently available fluorescent labels are not sufficiently bright and photostable to overcome the background associated with various autofluorescence and scattering processes. This dissertation describes research efforts focused on the development of a novel class of fluorescent nanoparticles called conjugated polymers dots (CPdots) for single molecule fluorescence detection. The CPdots contain highly fluorescent π-conjugated polymers that have been refined over the last decades as the active material in polymer light-emitting devices. Quantitative comparisons of the optical properties of the CPdots indicate their fluorescence brightness is a factor of 10^2-10^4 higher than conventional fluorescent dyes, and a factor of 10-10^3 higher than colloidal quantum dots. Single particle fluorescence imaging and kinetic studies indicate much higher emission rates of the CPdots as compared to quantum dots, with little or no "blinking" behavior that is often encountered for fluorescent dyes and quantum dots. In addition, efficient intra-particle energy transfer has been demonstrated in blended CPdots and dye-doped CPdots, which provides a new strategy for improving the fluorescence brightness and photostability of the CPdots, and for designing novel sensitive biosensors based on energy transfer to sensor dyes. These combined features of the CPdots and the demonstration of cellular uptake indicate that CPdots are promising probes for demanding fluorescence-based applications such as single molecule detection and tracking in live cells.

ACKNOWLEDGMENTS

I would like to thank my advisor, Jason McNeill, for his constant support throughout my graduate career. He led me to this highly interdisciplinary field and gave me the opportunity to work on and learn from a variety of techniques. For my research projects, Jason's suggestion and guidance always drove the experiments from merely a demonstration to a more meaningful level, which in the beginning seemed quite impossible. To me, Jason is not only a brilliant motivator, but also the best kind of leader – one who lets his kindness, passion, commitment, and work ethic, run the group. For sure I will cherish the time and experience I have worked with him.

I am very grateful to the remaining members of the McNeill's group for their scientific skills, language support, and their friendship. In particular I thank Craig Szymanski for his useful discussions and advice. He is very nice and patient to help in single molecule imaging experiments.

I thank my committee members – professors Steven Stuart, Kenneth Christensen, Dvora Perahia. All have been supportive of my research and I am very fortunate to have them as a part of my graduate career. I am sincerely grateful to Dr. Christensen as well as his student Barbara Bull for their assistance and discussions in cellular imaging experiments.

My eternal thanks go to my wife, our dear daughters Jennifer and Judy, and my parents back in China for their unconditional love and care. The following research work could not have been realized without their support.

TABLE OF CONTENTS

Page

LIST OF TABLES

Table Page

LIST OF FIGURES

List of Figures (Continued)

Figure Page

List of Figures (Continued)

Figure Page

CHAPTER 1 OVERVIEW

During the past decades there has been a remarkable growth in the use of fluorescence in chemistry and life sciences. In particular, fluorescence-based methods for probing biomolecular interactions at the single molecule level have resulted in significant advances in our understanding of various biochemical processes. However, in many cases currently available fluorescent labels are not sufficiently bright and photostable for single molecule imaging and sensing in optically murky environments such as in living cells and tissues. Innovative approaches in designing brighter fluorescent probes are required for further advances in cellular imaging and sensing applications. In this chapter, a brief overview of single molecule approaches is presented, in combination with the discussion of the development of fluorescent probes for single molecule imaging and advanced sensing applications.

1.1 Single molecule approaches to biology

Single molecule optical detections, were first demonstrated in doped crystals at low temperatures,[1, 2] and later at room temperature using near-field microscopy,[3, 4] and confocal microscopy.[5] The extension of single molecule fluorescence techniques to biology has resulted in new, exciting insights into biomolecular structure, conformation dynamics, and regulation within living cells.[6, 7] In view of the complex structure-function relationship of proteins that are essential parts of organisms and participate in every

process within cells, studies on protein dynamics will be used as examples to address the unique advantages of single molecule approaches over conventional ensemble methods.

Proteins are linear biopolymers that consist of specific sequences of amino acids, spontaneously forming three-dimensional (3D) structures in physiological conditions. Only correctly folded proteins have long-term stability in biological environments and are able to function with their natural partners. One of the great challenges in modern molecular biology is to understand how proteins find their native conformation (folded) starting from an initially random coil state (unfolded). The total number of possible conformations of a typical polypeptide chain is so large that a systematic search for a particular native state would take an astronomical length of time.[8] It is now clear that the folding process does not involve a systematic search, but rather a stochastic selection of the many conformations accessible to a polypeptide chain,[8] which ends in a stable native fold through a complex interplay between entropic and enthalpic contributions to the free energy of the system. Although classical fluorescence techniques can be used to study protein folding, they cannot unravel its stochastic nature because of ensemble averaging. However, the heterogeneity of folding pathways can be studied by single molecule spectroscopy (SMS), which lets us watch one molecule at a time, possibly leading to new insights into mechanisms of protein folding. In combination with Förster resonance energy transfer (FRET), it has enabled us to investigate intra-molecular distances and conformational dynamics of single protein molecules, including their folding, unfolding, and related functions.[9, 10]

Enzymes are a special class of proteins that catalyze biochemical reactions, which are needed in essentially every process in a biological cell. In terms of enzyme mechanisms, single molecule spectroscopy can allow the observation of transient intermediates that may be lost in ensemble measurements.[11] For enzymatic reactions where multiple turnovers occur, molecules are not synchronized in their dynamic behavior – at a given time each enzyme molecule is at a different stage of the reaction sequence. With single molecule approaches, synchronization is not an issue since the reaction sequence of each molecule can be observed. This is particularly important for sequential reactions such as DNA synthesis, as well as a large number of other biological processes.[11] Another kind of fascinating proteins is the so-called molecular motors that can transform chemical energy into directed movement. For example, the cargo protein kinesin uses the network of cytoskeletal fibers as roads to transport organelles, RNA, or signaling molecules to specific places within the cell. Two controversial models were proposed for the "walking mechanism": the hand-over-hand model, in which the two heads alternate in the lead, and the "inchworm" model, in which one head always leads. Selvin and co-workers specifically labeled a single head of the kinesin dimer site with the fluorescent dye Cy3, and applied single molecule tracking to localize the kinesin position with high precision, successfully unraveling the hand-over-hand walking model for kinesin motility.[12]

The advancements in single molecule biophysics have resulted in an unprecedented understanding about cellular processes such as gene expression, protein transport, signaling, and regulatory processes.[12-16] The performance of these single

molecule techniques is strongly dependent on the selection of fluorescent probes. For example, the FRET technique in the study of protein dynamics requires careful selection of bright and photostable fluorescent donor-acceptor pair between which efficient energy transfer can occur. In single molecule fluorescence imaging and tracking of molecular motors, the imaging resolution and tracking accuracy is determined by the number of detected photons, since the position of a single emitter can be localized to almost arbitrarily high accuracy if a sufficient number of photons are collected.[17] There is currently much interest in the extension of single molecule methods to living cells. However, the currently available fluorescent labels are not sufficiently bright and photostable to overcome the auto-fluorescence and scattering within the cells, which reduces the signal-to-noise ratio, limits the imaging and tracking resolution, and therefore hinders further application of the single molecule approaches to a broad range of processes in living systems. This has generated considerable interest in the design and development of brighter and more photostable fluorescent probes.

1.2 Fluorescent probes: from small molecules to nanoparticles

The suitability of a fluorescent dye for single molecule detection is determined by a number of factors such as fluorescence brightness, emission rate, and photostability. A useful estimate of fluorescence brightness is given by the product of the peak absorption cross section and the fluorescence quantum yield – typical fluorescent dyes employed in fluorescence microscopy exhibit absorption cross sections in the range of 10^{-16}-10^{-17} cm^2 and fluorescence quantum yields ranging from a few percent to nearly 100%. The limited brightness of conventional dyes and cellular autofluorescence results in signal-to-

background ratio that is too low for single molecule fluorescence detection in living cells. If we assume a fluorescence quantum yield of 100% and a typical fluorescence lifetime of 5 ns, a fluorophore would have a maximum emission rate of 2×10^8 photons per second if it were always excited immediately after emitting a photon. However, owing to the intersystem crossing, a molecule may be transferred from the excited singlet state to the triplet that has a very slow decay rate due to the forbidden transition. A fluorophore in such state will not emit any photons and until it returns to the ground singlet state that can be re-excited. Because of the so-called triplet saturation, typical fluorescent dyes exhibit a saturated emission rate on the order of 10^6 s^{-1}.[18] Furthermore, fluorophores undergo irreversible photobleaching upon intense laser irradiation, due to photochemical reactions occurring in molecular excited states. The most photostable dyes such as Rhodamine 6G can emit only ~10^6 photons prior to irreversible photobleaching,[19] insufficient for long-term single molecule fluorescence tracking. In addition, the presence of long-lived triplet or charge-transfer states, which typically have little effect in bulk measurements, can cause sudden, reversible fluorescence intermittency ("blinking"), therefore complicating single molecule measurements.

A number of strategies for developing brighter fluorescent probes have been pursued. Green fluorescent proteins (GFP) and some derivatives can in favorable cases be detected at the single molecule level.[14] However, approximately 30 copies of GFP are required for long-term single molecule tracking inside cells.[20] Fluorescent nanoparticles such as colloidal semiconductor quantum dots are under active development.[21, 22] However, these nanoparticles typically require an inorganic shell and a thick

encapsulation layer to reach the required levels of stability and biocompatibility. As a result, the encapsulation layers produce hydrodynamic diameters on the order of 20-30 nm for a core/shell diameter of only 4-6 nm,[23] which are sufficiently large to significantly alter biological function and transport of the biomolecules. While there has been recent work to reduce the thickness of the biocompatibility and encapsulation layers,[24] low emission rates, blinking, and a significant fraction of "dark" particles continue to pose potential difficulties for single particle measurements.[25] Dye-loaded latex or silica beads also possess relatively large sizes (>20 nm),[26] and limited dye-loading concentration due to aggregation and self-quenching. These limitations of current luminescent particles provide clear motivation for exploring alternative strategies for the design of more highly fluorescent nanoparticles.

1.3 Conjugated polymer dots as fluorescent probes

Conjugated polymers are a special class of polymers that possess π electrons delocalized along their backbones. They have exhibited versatile electrical and optical properties, and have been widely used as active materials in a broad range of electronic devices including organic light emitting diodes for flat panel displays, photovoltaic devices for solar energy conversion, thin-film transistors and chemical sensors.[27-29] There is recent interest in the preparation and optoelectronic applications of conjugated polymer nanoparticles. A miniemulsion method was recently developed to prepare submicron sized conjugated polymer particles (~0.1 μm diameter),[30, 31] and device layers with controlled domain sizes were achieved by casting from mixtures of suspended particles.[32] Another approach based on reprecipitation has also been applied to obtain polythiophene

nanoparticles.[33] These approaches prepare particles with a diameter of ~30 nm or higher that consist of hundreds of polymer molecules. In addition, ultrasensitive biosensors based on efficient fluorescence quenching of π-conjugated polyelectrolyte in aqueous solution have also been demonstrated.[34, 35] However, a largely unexplored area is the use of π-conjugated polymer nanoparticles as fluorescent labels for advanced fluorescence imaging and sensing applications.

The present study is to develop small sized conjugated polymer dots (CPdots) for single molecule imaging and sensing applications. The idea of using conjugated polymer dots as fluorescent probes is owing to a number of favorable characteristics of conjugated polymer molecules, including their high absorption cross sections (typically 10^{-15}-10^{-14} cm^2), high radiative rates, high effective chromophore density, and minimal levels of aggregation-induced fluorescence quenching, resulting in fluorescence quantum yields in excess of 70%, even for pure solid films.[36] The use of conjugated polymers as the fluorescent labels also confers other useful advantages, such as the lack of small dye molecules or heavy metal ions that could leach out into solution. Highly fluorescent CPdots as fluorescent tags directly addresses the need for brighter, more photostable fluorescent probes for single molecule detection in living cells. On the other hand, conjugated polymer dots represent a typical multichromophoric system containing disordered, densely-packed chromophores. Currently, the complex photophysical processes occurring on the nanoscale in these systems such as exciton-exciton coupling, energy diffusion, energy transfer, and charge transfer are not well understood. Thus the CPdots present a unique model system for studying energy transfer in nanostructured,

multichromophoric systems. A fundamental understanding of the nanoscale photophysical processes occurring in the CPdots is of great benefit to rationally develop probes for single molecule imaging, tracking and sensing applications.

CHAPTER 2 BASIC PRINCIPLES OF CONVENTIONAL AND SINGLE MOLECULE FLUORESCENCE SPECTROSCOPY

2.1 Absorption and fluorescence

The suitability of fluorophores for single molecule imaging is dependent on their absorption and fluorescence properties. How readily a molecule or particle absorbs light at a given wavelength is characterized by molar extinction coefficient that is determined by the Beer-Lambert law

$$A = \varepsilon \cdot c \cdot l \,, \tag{2.1}$$

where A is the absorbance of the sample, ε is the molar extinction coefficient ($M^{-1}cm^{-1}$), c is the sample concentration (M) and l is the sample pathlength (cm). The absorption at the single molecule level is often described by an absorption cross-section that is related to the molar extinction coefficient as follows

$$\sigma = \frac{2303\varepsilon}{N_A}. \quad (\mathrm{cm}^2) \tag{2.2}$$

Having absorbed a photon, the molecule gains the energy, and jumps to an excited state, followed by various photophysical processes that can be illustrated in a Jablonski diagram. The Jablonski diagram in Figure 2.1 depicts the singlet ground state S_0, first singlet excited state S_1, first triplet excited states T_1, and their associated vibronic states as well. The depopulation of the S_1 state can occur with transition rate constants k via different channels:

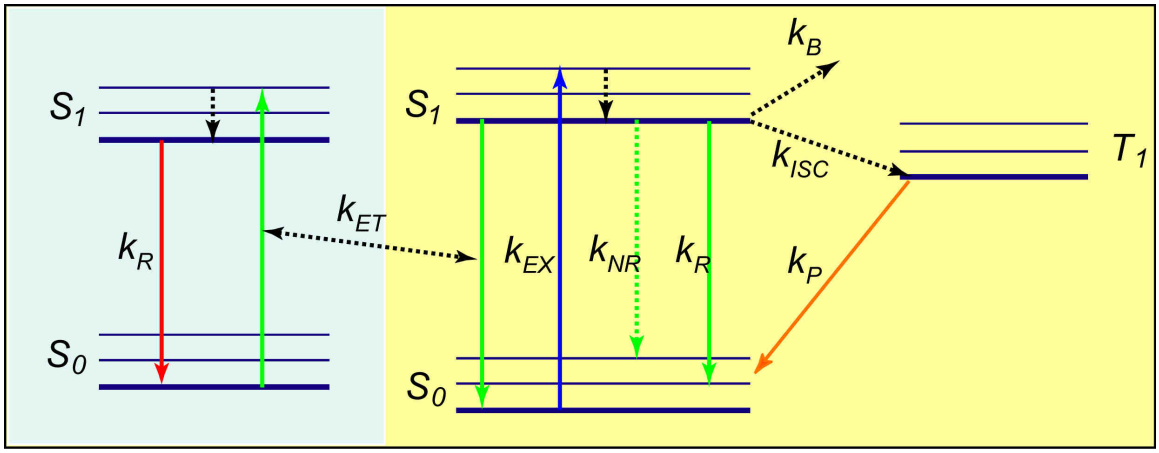

Figure 2.1 Jablonski diagrams for absorption, fluorescence, and energy transfer.

k_R: Radiative (fluorescence);

k_{NR}: Non-radiative (heat or phonon emission);

k_{ISC}: Intersystem crossing ($S_1 \rightarrow T_1$), followed by phosphorescence emission (k_P);

k_B: Photobleaching (photochemical reactions);

k_{ET}: Energy transfer to a different molecule (Discussed in section 2.2).

The fluorescence quantum yield is the ratio of the number of photons emitted to the number absorbed. Since all these rate constants could depopulate the S_1 excited state, the quantum yield ϕ_F, is given by

$$\phi_F = \frac{k_R}{k_R + k_{NR} + k_{ISC} + k_{ET} + k_B}. \tag{2.3}$$

The lifetime (τ) of the excited state is defined by the average time the molecule spends in the excited state prior to return to the ground state. It is usually expressed as the reciprocal value of the sum of all the transition rate constants of the involved processes

$$\tau = \frac{1}{k_R + k_{NR} + k_{ISC} + k_{ET} + k_B}. \tag{2.4}$$

Fluorescence quantum yield and lifetime can be experimentally determined by steady state and time-resolved fluorescence measurements, respectively. Considering a single fluorescent molecule ($k_{ET} = 0$, and generally, $k_R + k_{NR} >> k_{ISC} + k_B$), fluorescence radiative rate k_R can be estimated by combining the quantum yield [$\phi_F = k_R /(k_R + k_{NR})$] and fluorescence lifetime results [$\tau = 1/(k_R + k_{NR})$]. Typical fluorescent dyes exhibit fluorescence radiative rate constants on the order of ~10^8 s^{-1}, which indicates the theoretical maximum emission rates from single molecules. However, such large values

were observed very rarely (or only intermittently) in single molecule experiments. The solution of the rate equations leads to the well known fact that the actual average emission rate R of a fluorescent molecule saturates at high excitation intensities due to the presence of a nonfluorescent triplet state:[37]

$$R = \frac{I_e / I_s}{1 + I_e / I_s} R_\infty ,$$

$$I_s = \frac{(\sigma\tau)^{-1}}{1 + k_{ISC} / k_P} , \tag{2.5}$$

where the excitation saturation intensity I_s depends on the absorption cross-section σ, the fluorescence lifetime τ, and the triplet state population (k_{ISC}) and depopulation (k_P) rates. I_e is the excitation intensity, and R_∞ is the maximum fluorescence rate obtained asymptotically for infinite excitation rates.

2.2 Förster resonance energy transfer (FRET)

In multichromophoric systems such as conjugated polymers, a variety of photophysical processes occur on the nanoscale such as exciton diffusion and fluorescence quenching by dopant dye species or polarons. Different energy relaxation mechanisms account for these complex photophysical processes. Dexter transfer and Förster transfer are the two main mechanisms that describe the nonradiative energy transfer between two fluorophores in close proximity (<10 nm). Dexter transfer results from an electron exchange interaction, which requires an overlap in the wave functions of the energy donor and the energy acceptor. It is a short-range interaction (<2 nm), and must obey the spin conservation rules. Förster resonance energy transfer (FRET)

describes the energy transfer process between donor and acceptor due to a nonradiative dipole-dipole coupling, where the dipoles in this case represent the transition dipole moments of the molecules.[38] It is a relatively long-range interaction (up to 10 nm), and strongly dependent on the distance between the two chromophores. FRET has experienced a resurgence of interest due to a number of emerging applications such as studying protein dynamics, designing molecular beacon biosensors,[39, 40] and developing optoelectronic devices.[41] Here we focus on our discussion on the theoretical basics of Förster energy transfer.

The Förster theory of resonance energy transfer is best understood by considering a single donor and acceptor separated by a distance R. The energy transfer rate (k_{ET}) with the donor-acceptor separation R is given by [42]

$$k_{ET} = \frac{\phi_D \kappa^2}{\tau_D R^6}\left(\frac{9000(\ln 10)}{128\pi^5 N_A n^4}\right)\int_0^\infty F_D(\lambda)\varepsilon_A(\lambda)\lambda^4 d\lambda, \qquad (2.6)$$

where ϕ_D and τ_D are the fluorescence quantum yield and lifetime of the donor, respectively, in absence of the acceptor; κ^2 is a configurational factor describing the relative orientation of transition dipoles of the donor and acceptor, it can be replaced by its average value $<\kappa^2>$, which equals 2/3 for isotropic rotation; N_A is Avogadro's number; n is the refractive index of the medium; $F_D(\lambda)$ is the normalized emission spectra of the donor; $\varepsilon_A(\lambda)$ is the molar absorption coefficient of the acceptor. In order to simplify our discussion, we neglect the intersystem crossing rate k_{ISC} and photobleaching rate k_B of the donor (as expressed in Equation 2.3), since they are much smaller as compared to the radiative rate and energy transfer rates. Because the energy transfer rate k_{ET} depends on

R, it is convenient to define a distance R_0 (Förster radius) at which the energy transfer rate k_{ET} is equal to the total decay rate ($k_{ET}=\tau_D^{-1}=k_R+k_{NR}$) of the donor in absence of the acceptor. Thus, the FRET efficiency E can be expressed as

$$E = \frac{k_{ET}}{k_R + k_{NR} + k_{ET}} = [1 + (\frac{R}{R_0})^6]^{-1} \tag{2.7}$$

For single-molecule FRET, two approaches are generally used to experimentally determine the FRET efficiency E. One is the measurement of the fluorescence intensities from both the donor and the acceptor chromophores, and the calculation of the transfer efficiency according to Equation 2.7:

$$E = \frac{n_A}{n_A + \gamma n_D} \tag{2.8}$$

where n_A and n_D are the numbers of photons detected from the acceptor and donor chromophores, respectively, and γ is a correction factor that takes into account the quantum yields of the dyes and the efficiencies of the detection system in the corresponding wavelength ranges. The second approach is the determination of the fluorescence lifetime of the donor in the presence (τ_A) and absence (τ_D) of the acceptor, yielding the transfer efficiency as below

$$E = 1 - \frac{\tau_A}{\tau_D} \tag{2.9}$$

FRET efficiency determined by donor lifetime measurement or ratiometric measurement of the donor and acceptor emissions, is sensitive to the donor-acceptor distance and/or respective orientations. It is therefore extensively used to measure intermolecular interactions and to study molecular conformations.

2.3 Single molecule fluorescence detection

Single molecule fluorescence detection is based on thousands to millions of laser-induced excitation-emission cycles of the fluorophore. The basic principle and experimental design of single molecule imaging have been reviewed during the past few years.[9, 43, 44] Here we limit ourselves to describe schematically the two typical microscope geometries that are commonly used: confocal microscopy and wide-field microscopy (Figure 2.2). In the confocal geometry (a), a laser beam is focused onto the back focal plane of a high numerical aperture objective lens, which focuses the excitation light into a diffraction limited volume (focal volume) in the sample. Fluorescence emitted by molecules present in this volume is collected by the same objective and transmitted through dichroic mirrors, lenses, and color filters to one or several single channel detectors such as single photon avalanche photodiodes (APD) operating in Geiger mode. An important aspect of this geometry is the presence of a pinhole in the detection path (at the back focal plane of the objective), whose size and position is chosen such as to reject light originating from outside the focal volume. In the case of APD detectors, a pinhole is often not required due to the small active area of the detector. The wide-field geometry can be used in two different modes: (b) epifluorescence, and (c, d) total internal reflection fluorescence (TIRF). In wide-field epifluorescence (b), a laser beam focused at the back aperture of the objective, which illuminates large sample volume (large beam size at the sample focal plane) as compared to the confocal geometry. In TIRF, a laser beam is shaped in such a way that a collimated beam reaches the glass-air interface at an angle above the critical angle [$\theta = sin^{-1}(n_{air}/n_{glass})$], where n designates the index of refraction.

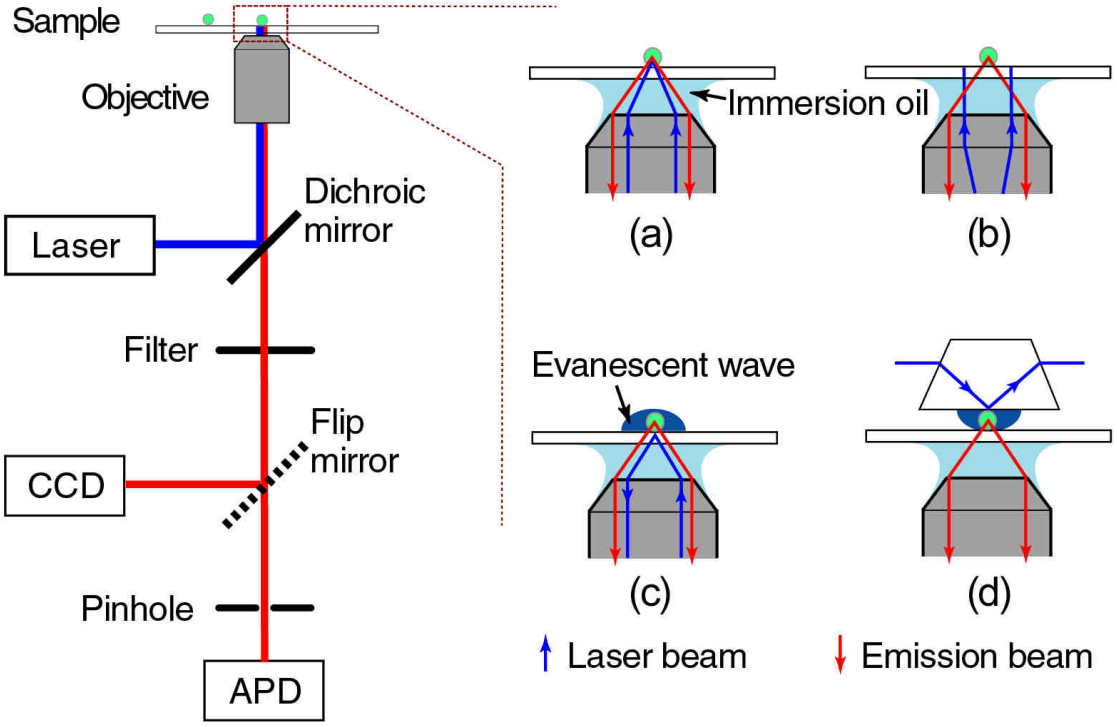

Figure 2.2 Experimental geometries in single-molecule fluorescence detection.

This creates an evanescent wave (decay length of a few hundreds nanometers) in the sample, which only excites the fluorescence of the molecules in the vicinity of the surface, resulting in reduced background as compared to standard epifluorescence. TIRF can be obtained either with illumination through the objective (c) or by coupling the laser through a prism (d). A wide-field detector (CCD camera) is generally used in all the three wide-field geometries, allowing the recording of several single-molecule signals in parallel. Individual intensity trajectories can be extracted from movies, resulting in similar information as that obtained with the confocal geometry.

We now discuss the optical components of the microscope, which determine the overall collection efficiency and ultimately affect the signal-to-noise ratio in the experiment. A key optical component of single molecule setup is the microscope objective, which on one hand focuses the excitation laser beam into a small volume, and on the other hand collects the emission light from the sample. Numerical aperture (*NA*) is the most important parameter associated with each objective. It provides a measure of its light gathering ability, and can be expressed as

$$NA = n \cdot \sin\theta , \tag{2.10}$$

where n is the refractive index of the immersion oil/glass coverslip (n = 1.515) and θ is the maximum incident light half angle. Numerical apertures in single molecule experiments typically range from *NA* = 0.9 to 1.45, with higher *NA* objectives being able to gather more light. For example, an objective with *NA* of 1.25 shows a maximum half angle θ = 55.6°. Based on this objective and assuming an isotropic point emission

source, the collection efficiency of the objective can be determined by the following expression

$$\eta_{obj} = \frac{1}{4\pi}\int_0^{2\pi} d\phi \int_0^{55.6} \sin\theta d\theta \,. \tag{2.11}$$

This equation can be readily integrated to yield η_{obj} = 0.22, which implies that the objective collects 22% of any isotropically emitted light. In practice, however, both the orientation of the transition dipole as well as the presence of a higher-refractive-index substrate will modify the objective's actual collection efficiency. The overall microscope detection efficiency η is now a product of η_{obj} along with the transmission efficiencies of other optical elements in the system. The efficiencies of both a dichroic beamsplitter and a dielectric barrier filter can be estimated based on their transmission curves. The last element to consider is the quantum efficiency of the detector. Despite the use of high-efficiency filters and dichroic mirrors, as well as single-photon-sensitive detectors, the typical collection efficiency of single-molecule imaging microscopes ranges from 1% to 10%.

Once the emission light from a fluorophore has been collected, the signal-to-noise ratio is the last factor dictating whether single-molecule detection is feasible. We can estimate the signal-to-noise ratio (SNR) in a hypothetical single molecule experiment. Based on the discussions in Section 2.1, we first calculate the number of detected photons *N*, which can be expressed as

$$N = \left(\frac{I\sigma}{h\nu}\right) \cdot \phi_F \cdot \eta \cdot \tau_{\text{int}}\,, \tag{2.12}$$

where I is the excitation intensity (Watt/cm^2), $h\nu$ is the photon energy of the excitation light, η is the total collection efficiency of the microscope, and τ_{int} is the integration time of the detector. Rhodamine 6G dye molecule is used as an example in the hypothetical experiment, which exhibits a molar extinction coefficient of 1.1×10^4 M^{-1}cm^{-1} at 532 nm and quantum yield approaching unity. The absorption cross-section can be converted from Equation 2.2, and the obtained value is $\sigma = 4.3\times10^{-16}$ cm^2. Assuming the excitation intensity I = 100 W/cm^2, the collection efficiency η = 5%, and the integration time τ_{int} = 0.2 s, which are typical values in a single molecule experiment, the number of detected photons N is estimated to be 1.0×10^3 photons. However, there are actually many potential sources of unwanted noise in an experiment. A general SNR expression in a single molecule experiment can be written as [45]

$$SNR = \frac{N}{\sqrt{N + n_{bkg} + n_{dark} + n_{read}^2}}. \tag{2.13}$$

While background noise (n_{bkg}) from other parts of the sample or from other undesired fluorophores will all reduce the signal-to-noise ratio, their contributions are generally suppressed by a careful choice of optics, solvents, substrates, and sample preparation conditions. The detector also contributes noise through dark counts (n_{dark}) and readout noise (n_{read}); however, the former can be practically eliminated by cooling the detector, in the case of CCD and APD detectors. For CCDs, the major detector contribution to noise is therefore readout noise, which originates in the amplifiers in the detector circuitry, and which is typically on the order of a few photons. For the case of EMCCDs (electron multiplied CCDs), the readout noise is well below a single photon. Therefore, as can be

seen from Equation 2.13, the major source of noise in a carefully constructed measurement is Poisson (shot) noise due to the signal itself. In most cases, the Poisson noise alone can be used to determine the possible SNR value, resulting in the expression as below

$$SNR = \sqrt{N} \quad . \tag{2.14}$$

For the hypothetical experiment using Rhodamine 6G molecule, the number of detected photons in 0.2 s is 1.0×10^3, and then SNR is calculated to be ~32, thus indicating that it is possible to view single molecules with reasonable contrast under these typical conditions.

CHAPTER 3 EXPERIMENTAL

3.1 Nanoparticle preparation

The conjugated polymers employed in this study are polyfluorene derivative poly(9,9-dihexylfluorenyl-2,7-diyl) (PDHF, average MW 55,000, polydispersity 2.7), poly(9,9-dioctylfluorenyl-2,7-diyl) (PFO, MW 147,000, polydispersity 3.0), the copolymer poly[{9,9-dioctyl-2,7-divinylene-fluorenylene}-alt-co-{2-methoxy-5-(2-ethylhexyloxy)-1,4-phenylene}] (PFPV, MW 270,000, polydispersity 2.7), Poly[(9,9-dioctylfluorenyl-2,7-diyl)-co-(1,4-benzo-{2,1',3}-thiadiazole)] (PFBT, MW 10,000, polydispersity 1.7), and the polyphenylenevinylene derivative Poly[2-methoxy-5-(2-ethylhexyloxy)-1,4-phenylenevinylene] (MEH-PPV, MW 200,000, polydispersity 4.0). These polymers were purchased from ADS Dyes, Inc. (Quebec, Canada). Another polymer Poly(2,5-di(3′,7′-dimethyloctyl)phenylene-1,4-ethynylene (PPE), fluorescent dyes such as perylene, nile red, and tetraphenylporphyrin (TPP), and the solvent tetrahydrofuran (THF, anhydrous, 99.9%) were purchased from Sigma-Aldrich (Milwaukee, WI). The phosphorescent dye platinum (II) octaethylporphine (PtOEP) was purchased from Frontier Scientific, Inc. Coumarin 1 and Coumarin 6, and [2-[2-[4-(dimethylamino)phenyl]ethenyl]-6-methyl-4H-pyran-4-ylidene]-propanedinitrile (DCM) were purchased from Exciton (Dayton, OH). All chemicals were used without further purification. Figure 3.1 shows the chemical structures of the conjugated polymers.

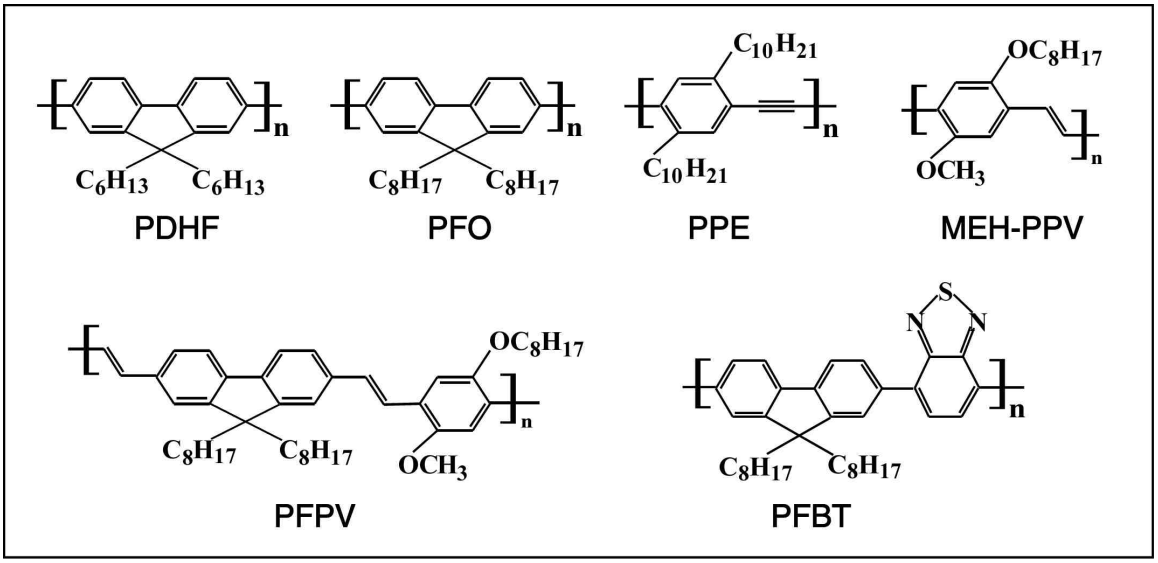

Figure 3.1 Chemical structures of the conjugated polymers.

We have demonstrated a facile method for preparation of a variety of conjugated polymer nanoparticles.[46, 47] The procedure is modified from the reprecipitation methods employed by Kurokawa and co-workers.[33] The preparation involves a rapid mixing of a dilute solution of polymer dissolved in a water-miscible organic solvent with water. The rapid mixing with water leads to a sudden decrease in solvent quality, resulting in the formation of a suspension of hydrophobic polymer nanoparticles. In a typical preparation, 20 mg of conjugated polymer was dissolved in 10 g of HPLC grade tetrahydrofuran (THF) by stirring overnight under inert atmosphere and the solution was filtered through a 0.7 micron glass fiber filter in order to remove any insoluble material. For preparation of small sized particles, the solution was further diluted to a concentration of 20 ppm. A quantity of 2 mL polymer/THF solution was added quickly to 8 mL of deionized water while sonicating the mixture. The suspension was filtered with a 0.2 micron membrane filter. The THF was removed by partial evaporation under vacuum, followed by filtration through a 0.2 micron filter. Overall yield of the nanoparticles was typically higher than 90%. The resulting nanoparticle dispersions are clear, with colors similar to those of the polymers in THF solution.

The reprecipitation process involves a competition between aggregation and chain collapse to form nanoparticles. Therefore, the particle size can be controlled by adjusting the polymer concentration in the precursor solution. To obtain nanoparticles with different sizes, three concentrations of a given polymer precursor were prepared, and the solutions (2 mL of 20 ppm, 100 μL of 1000 ppm, and 100 μL of 2000 ppm, respectively) were injected to 8 mL water, respectively. The THF was removed by partial vacuum

evaporation, and a small fraction of aggregates were removed by filtration through a 0.2 micron membrane filter. Higher precursor concentrations resulted in larger particle sizes.

Since the hydrophobic interaction is the primary driving force for nanoparticle formation, it is possible to introduce different hydrophobic fluorescent species during nanoparticle formation. Blended and dye-doped CPdots were prepared as follows. The host polymer solution was diluted to a concentration of 40 ppm. A given fluorescent dopant species (either conjugated polymers or fluorescent dyes such as perylene, coumarin 6, nile red, TPP, or PtOEP) was also dissolved in THF to make a 100 ppm solution. Varying amounts of a dopant dye solution were mixed with a polymer host solution to produce solution mixtures with a constant host concentration of 40 ppm and dopant/host fractions ranging from 0-10 weight percent. The mixtures were agitated to form homogeneous solutions. A 2 mL quantity of the solution mixture was added quickly to 8 mL of deionized water while sonicating the mixture. The resulting suspension was filtered through a 0.2 micron membrane filter. The THF was removed by partial vacuum evaporation, followed by filtration through a 0.2 micron filter. The resulting nanoparticle dispersions are clear and stable for months with no signs of aggregation.

3.2 Characterization methods

A variety of spectroscopic and microscopic techniques were employed to characterize the CPdots. The nanoparticle morphology and size distribution were characterized by atomic force microscopy (AFM). Steady-state and time-resolved spectroscopy were used to investigate the optical properties of the CPdots. Finally, single

particle fluorescence and cellular imaging were performed to evaluate the CPdots for single molecule applications.

3**.2.1 Atomic force microscopy.** The atomic force microscopy (AFM) is one of the family of techniques known as "scanning probe microscopy," which also includes such techniques as scanning-tunneling microscopy (STM). The AFM was developed in 1986 by Binnig, Quate, and Gerber, a few years after the development of STM.[48] In a general sense, these microscopes reveal information about the surface properties of materials by scanning the surface with a small probe. The AFM consists of a small tip or probe mounted in a piezoelectric scanner, a positioning stage supporting the scanner, an electronic interface unit (EIU) and a computer controlling the entire system. As the probe is "rastered" over the surface, the EIU maintains a condition of constant force between surface and probe by adjusting the height (Z dimension) of the probe. The movement of the tip over the surface is controlled by a piezoelectric ceramic, which can move in the X, Y, and Z directions in response to applied voltages. The tip is attached to a spring in the form of a cantilever. As the tip moves over the surface, the cantilever bends back and forth in the Z direction. A laser beam is directed onto the cantilever and as the cantilever bends, the movement of the reflected beam is detected by a photo diode. A feedback circuit integrates this signal and applies a feedback voltage so that the bending of the probe cantilever is held constant as the tip is scanned across the surface. The image of the surface morphology is built up as a series of scan lines, as the piezo moves along the X and Y directions to scan the sample. Each line displaced in the Y direction from the

previous one, which is a plot of the voltage applied to the Z piezo as a function of the voltage applied to the X piezo.

Depending on the application, the AFM can be operated in a number of modes, which require different cantilevers with different mechanical properties. The principal imaging modes are: contact mode, non-contact mode, and intermittent contact mode (also known as AC or “tapping” mode). In the contact mode, the tip is in contact with the sample and the tip-sample distance is in the steep, repulsive part of the tip-sample force curve. The cantilever deflection is used as a feedback signal and the repulsive force between the tip and the surface is kept constant during scanning by maintaining a constant deflection. Contact mode works best in situations where the material to be imaged is reasonably hard and the surface topography does not have abrupt edges or tall, steep features. Non-contact mode is similar to contact mode, but the tip-sample distance is maintained in the attractive part of the tip-sample force curve. Typically, non-contact mode suffers from difficulties in maintaining stable feedback conditions and reduced resolution due to the relatively weak attractive forces involved. In the intermittent contact mode, the cantilever is externally oscillated at or close to its fundamental resonance frequency. The oscillation amplitude and phase are modified by (primarily repulsive) tip-surface interaction forces. These changes in oscillation with respect to the external reference oscillation provide information about the surface's characteristics. Intermittent contact mode typically yields better resolution than non-contact mode and generally works better than contact mode for soft surfaces, surfaces with steep features, and loosely bound materials such as particles and biomolecules loosely adsorbed to a

surface – in contact mode, the tip often tends to push molecules and particles, resulting in movement of particles during scanning.

For the AFM measurements, one drop of the nanoparticle dispersion was placed on a freshly cleaned glass substrate. After evaporation of the water, the surface topography was imaged with an Ambios Q250 multimode AFM in intermittent contact mode. Since the properties of the piezoelectric scanner change with age, temperature and use, calibration must be performed periodically. Calibration using a standard of known dimensions (e.g., a diffraction grating) is a necessary procedure which sets the ability of the instrument to accurately measure distances in X, Y and Z. Detailed calibration procedure can be found in the operator's manual of the Ambios Q250 AFM. The tip effect in AFM is another factor affecting the measurement accuracy in X, Y directions. The lateral dimension of a nanometer object measured by AFM is closely correlated with the tip width: a fresh and sharp tip may result in apparent lateral dimension close to the actual size (still slightly larger), while a used and degraded tip may lead to much larger lateral size. Therefore, the Z height is a more reliable measure of the particle diameter when characterizing the diameters of spherical particles such as the CPdots. A number of scanning parameters such as scan size, scan rate, and scan resolution can also affect the measurement accuracy. For AFM in our lab (Ambios Q250 multimode), a detailed description of each scanning parameter is given in Chapter 3 of the AFM operator's manual. In a typical AFM measurement of small sized CPdots (<30 nm), the typical parameters were set as: scan size: 2 μm, scan rate: 0.5 Hz, and scan resolution: 500 lines.

3.2.2. UV-Vis and fluorescence spectroscopy. UV-Vis absorption spectra were recorded with a Shimadzu UV-2101PC scanning spectrophotometer using 1 cm quartz cuvettes. The fluorescence spectra were obtained using a commercial fluorometer (Quantamaster, PTI, Inc.). Fluorescence quantum yields of various CPdots were determined by a comparative method employing standard fluorescent dyes with known quantum yield values. Essentially, solutions of the standard and CPdot samples with identical absorbance at the same excitation wavelength can be assumed to be absorbing the same number of photons. Hence, a simple ratio of the integrated fluorescence intensities of the two solutions (recorded under identical conditions, and assuming similar emission spectra) will yield the ratio of the quantum yield values. Since quantum yield of the standard dyes are known, it is straightforward to calculate the quantum yields for the CPdots. In practice, however, we need to take into account a number of considerations: (1) using dilute solution (absorbance ~0.1) of both the standard and CPdots to avoid the inner filter effect; (2) including the solvent refractive indices in the quantum yield calculation $\phi_{F,x} = \phi_{F,std} (I_x/I_{std})(n_x/n_{std})^2$, where the subscripts *std* and *x* denote standard and CPdot respectively, ϕ_F is the fluorescence quantum yield, I is the integrated fluorescence intensity, and n is the refractive index of the solvent.

Photobleaching measurements were performed using methods similar to those described elsewhere,[19] but using the light source built in the fluorometer. The slit widths on the excitation monochromator of the fluorometer were adjusted slightly to generate illumination light (wavelength corresponding to the peak absorption of the CPdots) with a power of 1.0 mW as determined by a calibrated photodiode (Newport model 818-sl). The

light was focused into a quartz cuvette containing constantly stirred nanoparticle dispersion with an absorbance of 0.10. The fluorescence intensity at a specific wavelength was recorded continuously over a time period of 2 hours. By comparison of the photobleaching kinetics of a sample to the photobleaching kinetics of a standard of known absorbance, the photobleaching quantum yield of a given sample was determined. From the photobleaching quantum yield and the fluorescence quantum yield, the photon number N was determined using equation $N = \phi_F / \phi_B$.

3.2.3 Two-photon excited fluorescence. The fluorescence brightness for two-photon excited fluorescence is characterized by the two-photon action cross-section, which is the product of the two-photon absorption cross-section σ_{2p} and the fluorescence quantum yield ϕ_F. The two-photon action cross sections were determined as a function of wavelength using a home-built two-photon fluorescence spectrometer. A mode-locked, tunable Ti:sapphire laser (Coherent Mira 900) providing ~100 fs pulses at a repetition rate of 76 MHz with a tuning range of 770 to 870 nm was used as the light source for two-photon excitation. The laser beam was focused by a glass lens (f.l.=30 mm) into a quartz cuvette containing an aqueous dispersion of CPdots. The two-photon excited fluorescence was collected in a perpendicular geometry using a 50 mm focal length lens, filtered by the combination of a Schott glass BG-38 filter and two 700 nm short-pass filters (Andover 700 FL07) in order to remove scattered laser light, and focused onto a single photon avalanche diode module (Perkin Elmer, SPCM-AQR). The count rate was determined using a 100 MHz bandwidth frequency counter (EZ Digital, FC7015). As shown in Figure 3.2, the sample holder, lens, filters, and the detector were placed in a

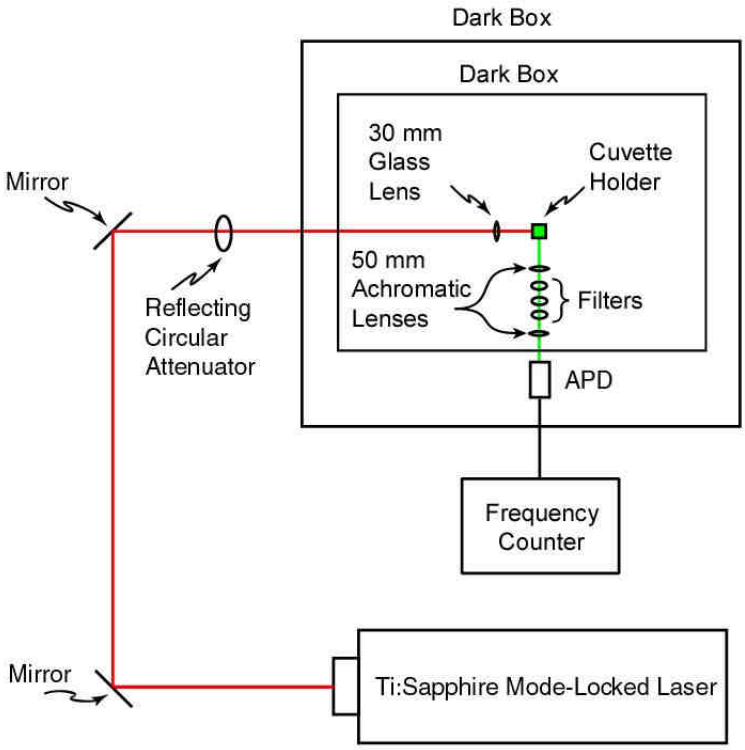

Figure 3.2 Experimental setup for measuring two-photon action cross section.

small dark box, and then covered by a larger dark box to reduce the amount of background signal due to leakage of room light to acceptable levels. A dilute dispersion of polystyrene beads was used to estimate the contribution of scattered laser light to the background signal, which was determined to be less than 500 Hz under typical laser excitation conditions. In actual measurement, laser power was attenuated with a variable neutral density filter wheel, and measured using a calibrated photodiode (Coherent LaserCheck). The count rate due to fluorescence is in the range of 20-300 kHz, much higher than the count noise and well below the saturation of the detector. Fluorescence counts were recorded and plotted versus various excitation powers to confirm the two-photon excited process and calculate the two-photon action cross section at a given excitation wavelength. The process was repeated for several wavelengths in order to determine the two-photon excitation spectrum. The above method was validated by determining the two photon excitation spectrum of Rhodamine B using Lucifer yellow as a standard. The determined two photon action spectrum for rhodamine B is consistent with literature results for the absolute two-photon action cross-section.[49] Finally, Rhodamine B and Lucifer yellow were used as standard dyes to measure the two-photon action cross-sections and excitation spectra of the CPdots.

3.2.4 Time-correlated single-photon counting. The fluorescence lifetimes of the CPdots were measured using time-correlated single-photon counting (TCSPC). The principle of TCSPC is based on pulsed optical excitation of a sample, the detection of single photons of the periodic sample fluorescence signal, the measurement of the time difference between excitation pulse and fluorescence photon, and the reconstruction of

the fluorescence decay waveform from the individual time measurements. The schematic diagram of TCSPC is shown in Figure 3.3. The experiment starts with an optical pulse that excites the samples and sends a timing pulse to the electronics. This signal pulse is passed through a constant fraction discriminator (CFD), which generates an accurate timing pulse of proper voltage and polarity from a source with pulse-to-pulse amplitude variations (in effect, it “cleans up” the timing pulse). This output pulse of the CFD is passed to the “start” input of a time-to-amplitude converter (TAC), which then starts a voltage ramp that increases linearly with time on the nanosecond timescale. A second detector detects a single emission photon (associated with the excitation pulse), and generates a pulse. The detector pulse is passed to a CFD, which sends a pulse to the “stop” input of the TAC to signal it to stop the voltage ramp. The TAC now contains a voltage proportional to the time delay between the excitation and emission pulses. The voltage signal from the TAC was digitized using a multichannel analyzer to construct a histogram of individual photon arrival times which represents the fluorescence decay waveform.

In our experiment, a given CPdot sample was excited by the second harmonic (400 nm, ~100 fs pulse duration, ~76 MHz repetition rate) generated from a mode-locked femtosecond Ti:Sapphire laser (Coherent Mira 9000) using a BBO doubling crystal (beta barium borate crystal, 100 microns, AR-coated, cut for type I SHG). The output of a fast PIN diode (Thorlabs, DET210) monitoring the laser pulse was used as the start pulse for a time-to-amplitude converter (TAC, Canberra Model 2145). Fluorescence signal from the aqueous nanoparticle dispersion was collected in perpendicular to the excitation,

passed through appropriate emission filters (selected to match the fluorescence wavelengths of the various CPdots), and detected by a high speed single photon counting module (id Quantique, ID100-50, ~20-30 ps timing resolution). The output pulse of the detector was used as the stop pulse for the TAC. The TAC can only accept one stop pulse per start pulse (subsequent stop pulses are ignored), so the laser was attenuated to maintain the count rate below 20 kHz in order to reduce nonlinearities by ensuring that the probability of two photons arriving at the detector due to a single laser pulse was well below 1%. The signal from the TAC was digitized using a multichannel analyzer (FastComTec, MCA-3A). The instrument response function was measured before and after each fluorescence lifetime measurement using the scattered laser light from a dilute suspension of polystyrene beads. The combination of the detector and electronics results in an instrument response function with a width of ~50 ps (FWHM). By using appropriate fitting methods based on comparing the time-resolved fluorescence to the convolution of the instrument response function with an exponential decay function, fluorescence time constants as short as 20-30% of the FWHM of the instrument response function can be reliably extracted.[42] Custom software written in the MATLAB environment (Mathworks) employing fast fourier transform methods to perform the required convolutions and using Nelder-Mead (downhill simplex) optimization [50] or a custom multigrid search method was employed to determine fluorescence lifetimes from the TCSPC data.[42] Statistical analyses yielded an estimated uncertainty in lifetime of roughly 10% (somewhat higher for lifetimes of less than 100 ps). At least 6 experimental runs were performed on each sample (alternating between the fluorescent sample and the

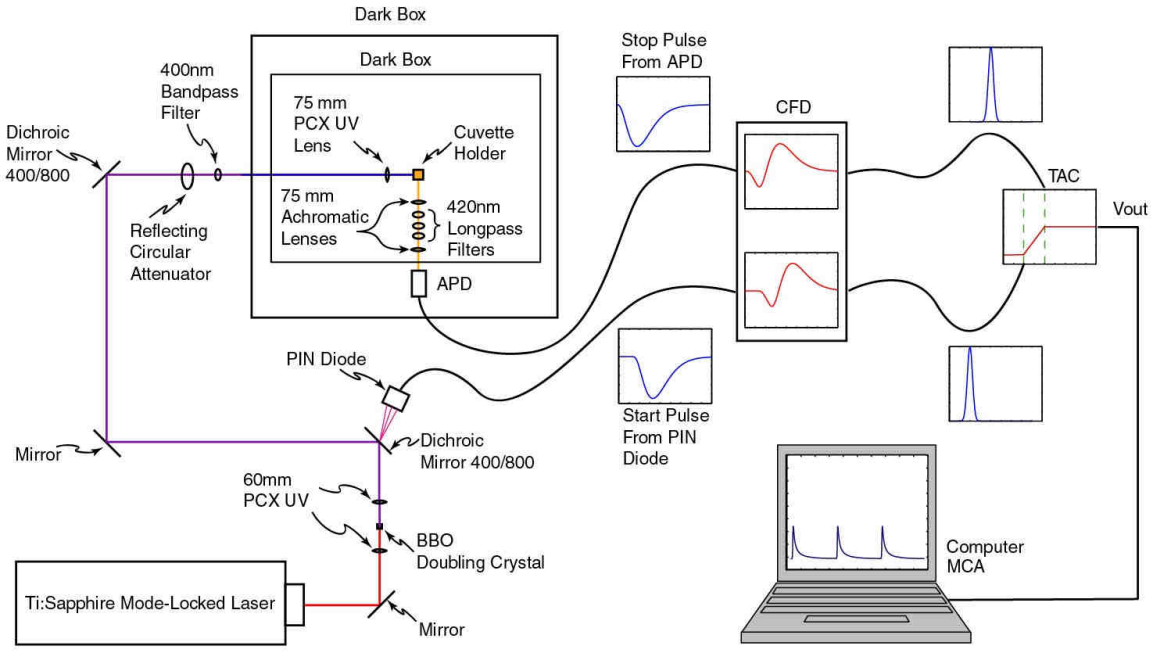

Figure 3.3 Schematic diagram of time-correlated single-photon counting.

nonfluorescent scattering sample used for determination of the instrument response function), and coumarin 6 dissolved in ethanol was used as a lifetime standard in order to validate proper functioning of the instrument. In addition, the timing of the TCSPC apparatus was precisely calibrated periodically by comparing the time between subsequent laser pulses on the TCSPC setup with the repetition rate of the mode-locked Ti:Sapphire laser as determined by a precision frequency counter.

3.3 Single particle imaging/spectroscopy setup

3.3.2 Wide-field microscope for single particle imaging and kinetics. Sample preparation for single particle fluorescence imaging experiments consists of drop-casting a dilute CPdot suspension onto a cleaned microscope cover glass. Single particle fluorescence imaging was performed on a customized wide-field epifluorescence microscope described as follows. The 488 nm laser beam from an argon laser (or 405 nm laser beam from a diode laser) is guided onto the epi-illumination port of an inverted fluorescence microscope (Olympus IX-71). Inside the microscope, the laser beam is reflected by an appropriate longpass dichroic mirror (Chroma 420 DCLP or Chroma 500 DCLP), and focused onto the back aperture of a high numerical aperture objective (Olympus Ach, 100X, 1.25 NA, Oil). The laser excitation at the sample plane exhibits a Gaussian profile with full width at half maximum of ~5 microns. Fluorescence from CPdots is collected by the same objective lens, passes through the dichroic mirror, and is focused by the microscope optics to form an image at the side port of the microscope. Outside the microscope, the fluorescence light is then filtered by appropriate longpass filters and then refocused by an additional lens (achromat, 75 mm focal length, placed

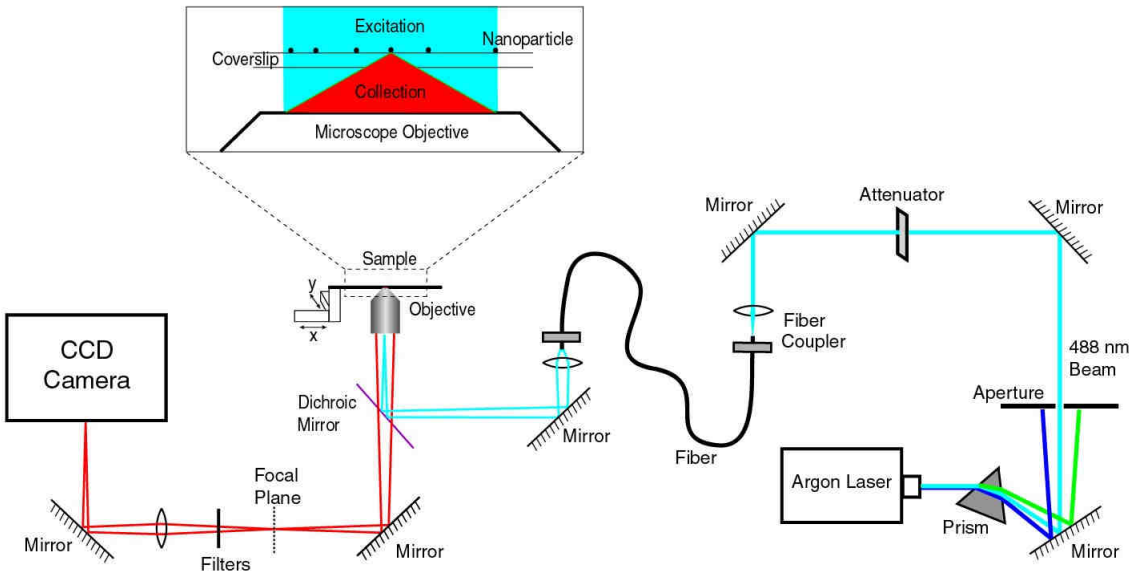

Figure 3.4 Wide-field microscope for single particle imaging and kinetics.

150 mm after the side port and 150 mm before the CCD) onto a back-illuminated frame transfer CCD camera (Princeton Instruments, PhotonMAX: 512B). The CCD camera possesses a square sensor chip with 512×512 pixels (pixel size: 16×16 μm). A spherical object with diameter of 70 μm on a calibration slide was imaged on the CCD chip using white-light illumination (transmission image). The pixel resolution of the microscope was determined by comparing the image size (object width in pixels multiplied by the pixel size) with the actual size, resulting in a pixel resolution of 105 nm/pixel. The overall fluorescence collection efficiency was estimated according to the collection efficiency of the microscope objective (provided by the manufacturer) along with the transmission curves of the dichoric mirror, filters, and the quantum yield of the detector, yielding the total collection efficiency of 3-5%. This value is confirmed by using Nile red loaded polystyrene spheres (Molecular Probes). The absorption cross-section and fluorescence quantum yield were estimated according to the specification of this probe (Molecular Probes). The laser excitation intensity for a given particle was calculated based on the measured laser power and laser excitation profile. The number of detected photons per second (under excitation conditions maintained well below saturation) was calculated from the integrated CCD intensity for a given particle based on the quantum efficiency of the CCD detector (provided by the manufacturer) and the ADC gain of the CCD chip. The calculated value was compared with the theoretical number of photons emitted per particle per second, leading to a value consistent with the estimated collection efficiency.

3.3.2 Confocal microscope for single particle imaging and kinetics with two-photon excitation. Single particle two-photon fluorescence imaging was performed

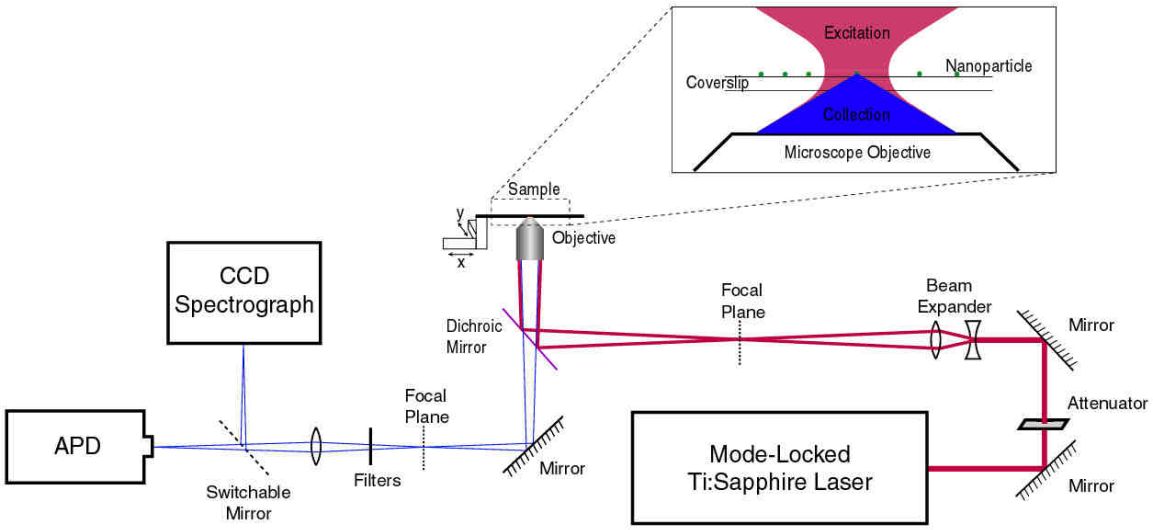

Figure 3.5 Confocal microscope for single particle imaging and kinetics with two-photon excitation.

on a custom-built sample-scanning confocal microscope described as follows. The light source for two-photon imaging is a mode-locked Ti:sapphire laser (Coherent Mira 900) providing ~100 fs pulses at a repetition rate of 76 MHz and tunable from 770 to 870 nm. The laser beam is expanded and focused onto the focal plane of the epi-illumination port of an inverted fluorescence microscope (Olympus IX-71). Inside the microscope, the laser beam is reflected by a shortpass dichroic mirror (Chroma 675DCSX) towards the back of a high numerical aperture objective (Olympus Ach, 100X, 1.25 NA, Oil) and is focused to a nearly diffraction-limited spot. Fluorescence from CPdots is collected by the same objective lens and filtered by the combination of a BG-38 filter (Schott glass) and two 700 nm shortpass filters (Andover 700 FL07). The fluorescence is then focused onto a single photon avalanche diode module (Perkin Elmer, SPCM-AQR) and the fluorescence counts are recorded using a 100 MHz counter card (NI-PCI-6602, National Instruments). The coverslip is mounted on a piezoelectric XYZ scanner (P-517.3CL, Polytec PI) connected to the analog outputs of a multifunction data acquisition card (NI-PCI-6036E, National Instruments). Images were acquired by raster scanning the sample under the control of custom data acquisition software written in the LabView environment (National Instruments). A schematic of the apparatus is shown in Figure 3.2. After an image is obtained, a particular particle can be placed into the focus (under computer control) so that single particle spectroscopy and photobleaching kinetics measurements can be performed.

3.3.3 Cellular Imaging. For cellular imaging, J774.A1 macrophages (ATCC, Manassas, VA) were plated at 2×10^5 cells/dish onto 35 mm glass-bottom microscope

dishes (Matek, Ashland, MA), and allowed to incubated overnight (5% CO_2, 37°C). Next, 300 μL of sterile filtered nanoparticle dispersions (~ 1 nM) were added to the cells and allowed to incubate for 12 hours. The cells were then washed three times with warm Ringer's buffer before viewing. Images were acquired on an inverted microscope (Olympus IX71) using Xe arc lamp excitation and appropriate filters and beam-splitters (Chroma).

CHAPTER 4 MULTICOLOR CONJUGATED POLYMER DOTS FOR SINGLE MOLECULE IMAGING

In this chapter, we present the preparation of multicolored CPdots (conjugated polymer nanoparticles), and their photophysical characteristics relevant for demanding applications such as single particle imaging in living cells. These CPdots were characterized in terms of their size, per-particle fluorescence brightness, emission rate, and photostability. Single particle fluorescence imaging and kinetic studies indicate much higher emission rates (~10^8 s^{-1}) and little or no blinking of the CPdots as compared to typical results for single dye molecules and quantum dots. Photobleaching results for various CPdots reveal excellent photostability – as many as 10^9 or more photons emitted per nanoparticle prior to irreversible photobleaching. Cellular uptake of the nanoparticles via endocytosis was observed. The extraordinary brightness of the CPdots, high emission rates, small particle diameters, and the demonstration of cellular uptake indicate that CPdots are promising probes for demanding fluorescence applications such as single molecule detection and tracking in live cells. The major results presented in this chapter have appeared in journal articles that have been published. [46, 51]

4.1 Nanoparticle size and morphology

We have first demonstrated the preparation of small nanoparticles (~10 nm) of a variety of hydrophobic conjugated polymers.[46, 47] Aqueous dispersion of PDHF, PFPV, and MEH-PPV dots were prepared by the procedure that is modified from the

reprecipitation methods employed by Kurokawa and co-workers.[33] The nanoparticles are stable for weeks, with no evidence of aggregation or decomposition. The CPdot dispersions were drop-cast onto silicon substrates for analysis of nanoparticle size and morphology by an AFM in intermittent contact mode. Figure 4.1 shows the AFM images of various nanoparticles on silicon substrates. The nanoparticles exhibit a roughly spherical morphology and they can form either a densely packed layer (Figure 4.1a) or a sparse layer of well-separated nanoparticles (Figure 4.1b and 4.1c) depending on drop-casting conditions. Detailed analysis of the particle morphology indicates that the majority of particles are approximately spherical in shape. Further indication that most particles are approximately spherical is that the aspect ratio obtained from the AFM images of the nanoparticles is similar to that obtained for 20 nm latex spheres (Molecular Probes). In addition, the nearest-neighbor spacing of dense arrays is similar (within measurement uncertainty) to the particle height. The observation of approximately spherical morphology is somewhat surprising considering that the rigid, planar, sp^2 hybridized backbone of conjugated polymers is known to exert a large influence over polymer conformation.[52] However, given the large interfacial tension between the polymer and water and the large surface-to-volume ratio of the nanoparticles, a collapsed, roughly spherical polymer conformation is thermodynamically favored, even for somewhat rigid polymers, according to theory[53] and experiment.[54] Additionally, there is evidence that the vinylene linkages are not as rigid as previously believed – some calculations have indicated that the energy required to bend a conjugated polymer chain

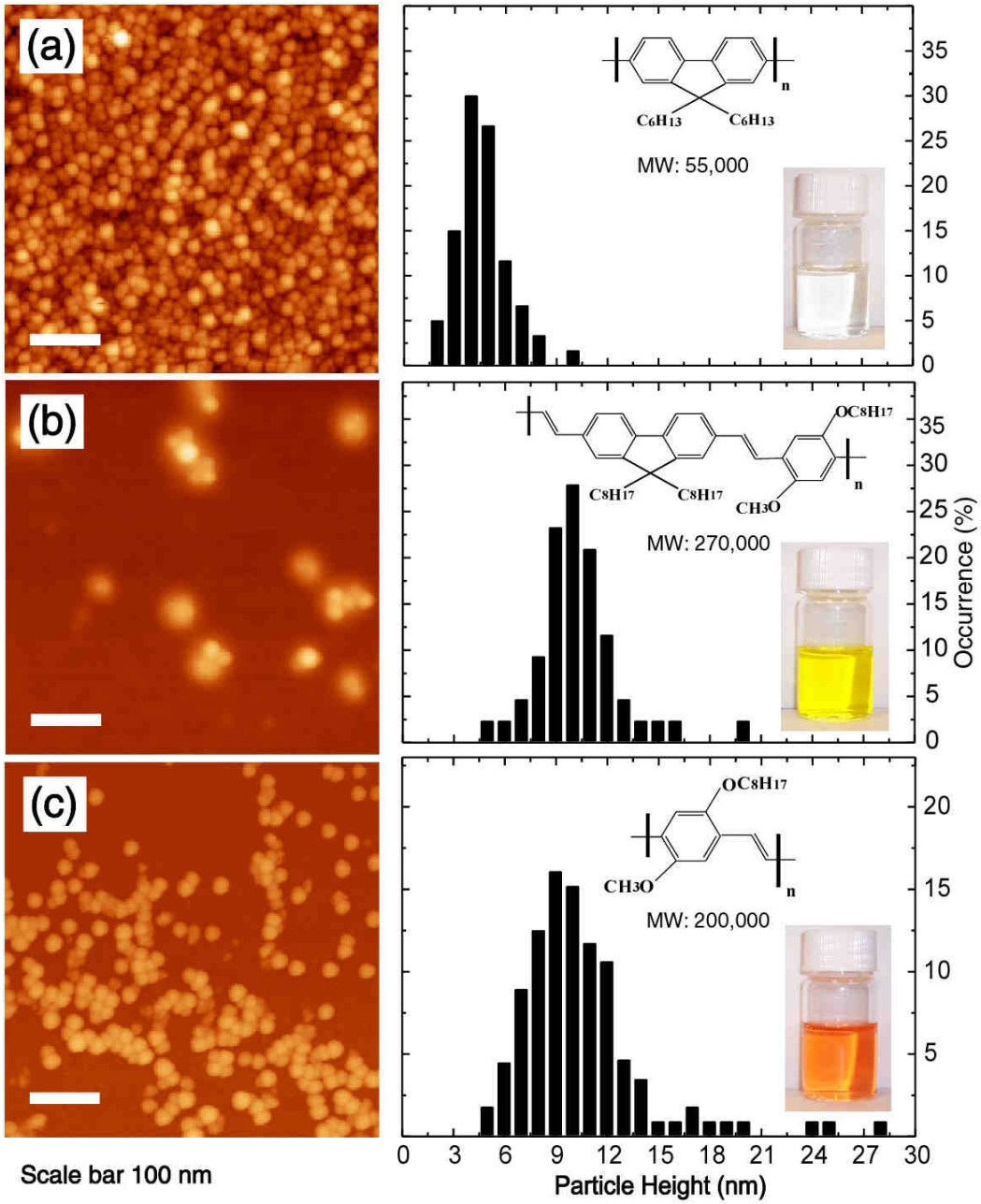

Figure 4.1 Nanoparticle size and morphology of conjugated polymer dots.

by generating a tetrahedral defect is thermally accessible.[55] However, while this result helps explain the morphology of phenylene-vinylene conjugated polymers, the nature and thermodynamics of kinks in phenylene-ethynylene and fluorene-based polymers remains unclear.

A particle height analysis was done on AFM images of sparse layers, and the corresponding histograms are shown in Figure 4.1 (right). The majority of nanoparticle diameters are in the range of 3-7 nm, 8-12 nm, and 5-14 nm for PDHF, PFPV, and MEH-PPV nanoparticles, respectively. The average diameters of the nanoparticles are consistent with roughly spherical single molecules of conjugated polymer, assuming tight packing of the polymer chain. For MEH-PPV, the much larger size range is attributable to the large polydispersity of the precursor polymer. While there are batch-to-batch variations (with a small fraction of aggregates), the size distributions of the nanoparticles prepared from starting solution less than 20 ppm are consistent with roughly spherical single molecules of conjugated polymer with the molecular weight and polydispersity of the precursor polymer.

Since the reprecipitation process involves a competition between aggregation and chain collapse to form nanoparticles, the particle size can be controlled by adjusting the polymer concentration in the precursor solution. To explore the effect of precursor concentration on particle size, we focus our discussion on two polymers that form highly photostable nanoparticles: PPE and PFBT. PPE dots were prepared using different concentrations of the polymer in the precursor solution ranging from 20 ppm to 2000 ppm. As shown in the AFM image of Figure 4.2a, the PPE nanoparticles also exhibit an

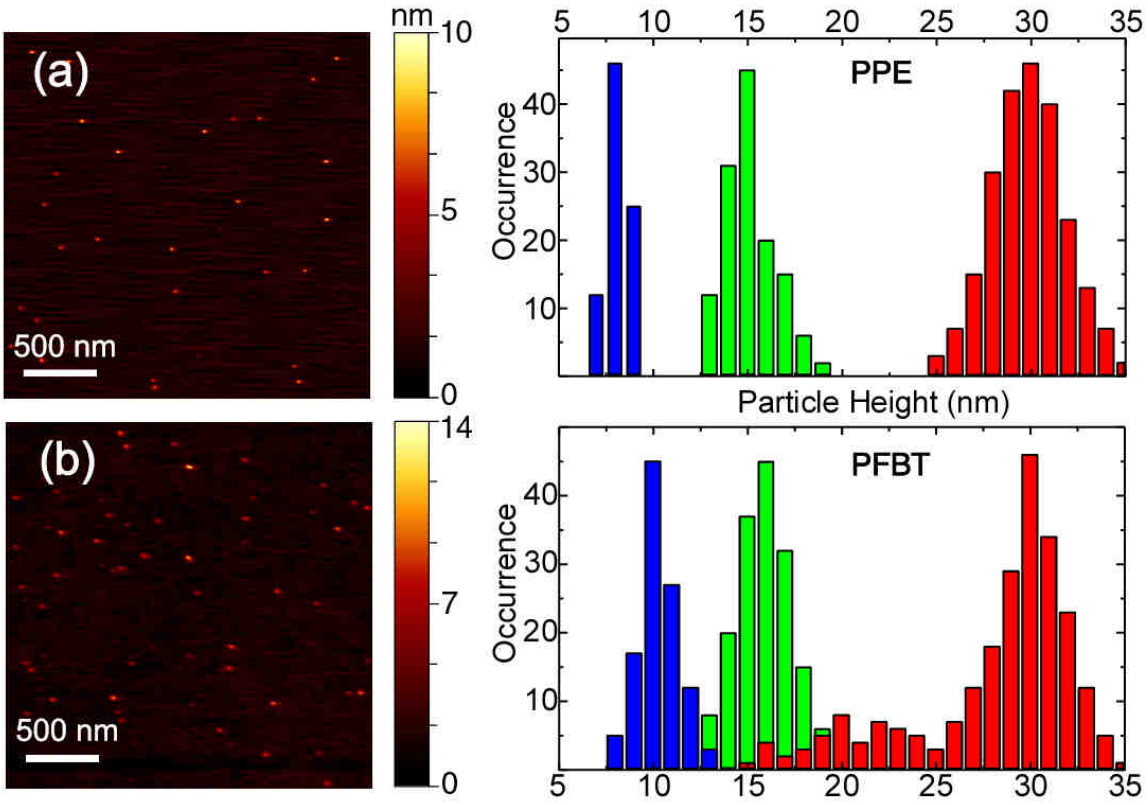

Figure 4.2 Nanoparticle size distributions of PPE and PFBT dots prepared with different precursor conditions.

approximately spherical shape. Analysis of particle height indicates that the nanoparticles produced using the lowest precursor concentration possess small particle size and a relatively narrow size distribution (8±1 nm diameter), while those prepared from more concentrated precursor solutions exhibited larger diameters. PFBT dots that were prepared using a range of concentrations of the precursor solution exhibit a similar trend – the PFBT dots obtained using a dilute solution exhibit relatively small particle size and size distribution (10±3 nm), while those prepared using higher precursor concentrations exhibit larger size (Figure 4.2b). The specific particle size and size distribution are also dependent on the polymer species (as well as other conditions that may affect the mixing and aggregation rates). For example, the larger PFBT dots in Figure 4.2b exhibit a relatively broad size distribution (25±10 nm) and a substantial fraction of small dots. PFPV dots prepared under the same conditions exhibited much larger particle sizes, in the range of 50-70 nm. The size differences are likely due to differences in the molecular weight, polydispersity, and interchain interactions of the different polymers.

4.2 Steady state and time-resolved fluorescence spectroscopy

The aqueous CPdot suspensions obtained from various conjugated polymers are stable and clear (not turbid), presenting colors associated with their visible absorption spectra. Under UV lamp illumination (365nm), the nanoparticle dispersions exhibit strong fluorescence with a wide variety of colors, as shown in Figure 4.3 (top). The changes in the absorption spectra and fluorescence spectra upon particle formation vary depending on the polymer (Figure 4.3a and 4.3b). For PFBT, PFPV, and MEHPPV, the absorption spectra are broadened and blue-shifted as compared to those of the polymer in

THF solution, which is consistent with an overall decrease in the conjugation length due to bending, torsion, and kinking of the polymer backbone. The nanoparticles also (in most cases) exhibit a slightly red-shifted fluorescence and a long red tail as compared to the polymer in organic solvent. This is attributable to increased interchain interactions due to chain collapse, resulting in a fraction of red-shifted aggregate species.[46] The resulting energetic disorder, combined with multiple energy transfer, would result in a net red-shift in the fluorescence spectrum as compared to that of the polymer in THF solution, as has often been observed in thin films.[56] For PFO nanoparticles, the additional absorption feature and the red-shifted fluorescence are attributed to the β-phase conformation.[57] The relatively complex absorption and fluorescence structures observed for PPE dots may be due to the complex packing and phase behavior of polymer chains, as was previously observed in thin films of similar PPE derivatives.[58] However, due to the complex phase behavior of PPE derivatives, additional studies are required to obtain definitive information about the internal structure of the nanoparticles.

CPdots exhibit broad absorption bands ranging from 350 nm to 550 nm (depending on the polymer), a wavelength range that is convenient for fluorescence microscopy and laser excitation. The absorption at single molecule level is often characterized by absorption cross-section. To determine absorption cross section per polymer molecule in water, an aqueous CPdot suspension was prepared by injecting 200 μL of 20 ppm polymer/THF solution to 8 mL water, removing THF by partial vacuum evaporation at room temperature, and then filtering the solution through 100 nm membrane filter. Under such preparation conditions, the nanoparticle yield is nearly

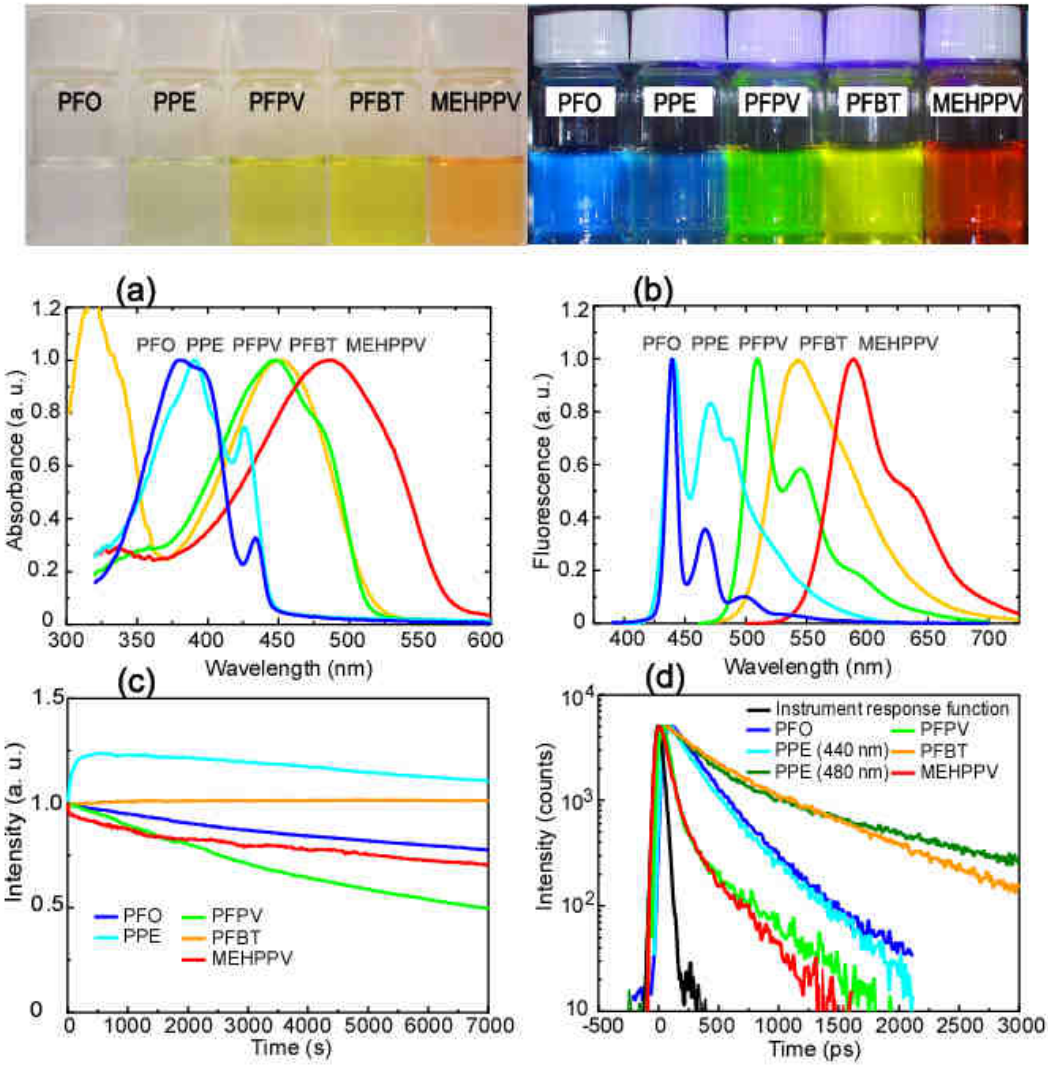

Figure 4.3 Steady state and time-resolved fluorescence spectroscopy of the CPdots. The top shows photographs of aqueous CPdots suspensions under room light (left) and UV light (right) illumination. The bottom presents absorption spectra (a), fluorescence spectra (b), photobleaching curves (c), and fluorescence decay traces (d) of various conjugated polymer dots.

100% (no apparent aggregrates remained in the filter) so that we know the polymer molar concentration in the suspension based on the weight concentration and the average molecular weight of the polymer. The absorption cross section per polymer molecule in water was determined according to UV-Vis absorption measurement and the Beer-Lambert law (Equations 2.1 and 2.2). In preparation of larger particles containing several or many polymer molecules, a small fraction of aggregates usually formed and was filtered out from the CPdot suspension. After removal of the aggregates, UV-Vis measurements were performed to determine the actual polymer molar concentration in the suspension based on the above-determined polymer absorption cross section and the Beer-Lambert law (Equations 2.1 and 2.2). The nanoparticle diameter was measured by AFM, and the nanoparticle weight was determined by the product of nanoparticle volume (assuming a spherical particle) and the polymer density (for most of the conjugated polymers: ~1g/cm^3). Now we can calculate the average number of polymer molecule per particle (nanoparticle weight divided by average weight per polymer molecule) and the nanoparticle concentration (polymer molar concentration divided by the average number of molecules per particle). Analysis of the UV-Vis absorption spectra at a known particle concentration indicated that the peak absorption cross section of single particles (~15 nm diameter) were on the order of ~10^{-13} cm^2, roughly ten to hundred times larger than that of CdSe quantum dots in the visible and near-UV range, and roughly three orders of magnitude larger than typical organic fluorescent dyes.

Fluorescence quantum yields (ϕ_F) ranged from a few percent to as high as 40%, depending on the polymer. The absorption cross section and quantum yield results are

summarized in Table 1. These results indicate that, to the best of our knowledge, the fluorescence brightness of the CPdot nanoparticles exceeds that of any other nanoparticle of the same size under typical conditions. The size of the particle does not appear to have an appreciable effect on the shape of the absorption and fluorescence spectra – the principal effect of increased particle size is an increase in the absorption cross-section. This property facilitates adjustment of particle size and brightness to meet the demands of a particular application, and is in contrast with colloidal semiconductor quantum dots, which exhibit pronounced variations in band gap due to the quantum size effect. For a given polymer, particle size was also found to affect fluorescence quantum yield. For example, a quantum yield of ~0.10 was determined for small PFPV dots (~10 nm), while larger PFPV particles (~60 nm) exhibit a decreased quantum yield of ~0.04. The size-dependence of the quantum yield is likely due to the effect of particle size on the efficiency of energy transfer to various fluorescence quencher species present in the nanoparticle, consistent with both the results of exciton diffusion and energy transfer simulations and the size-dependent energy transfer efficiency we have previously observed in dye-doped CPdots.[59] The effect of particle size on exciton-phonon coupling may also play a role.[60]

The photostability of the CPdot nanoparticles is critically important for many fluorescence-based imaging applications, particularly for long-term imaging and tracking experiments.[61, 62] The photostability of a fluorescent dye or nanoparticle can be characterized by photobleaching quantum yield (ϕ_B), which is the number of molecules that have been photobleached divided by the total number of photons absorbed over a

given time interval.[19] Typical fluorescent dyes exhibit photobleaching quantum yields in the range of 10^{-4} to 10^{-6},[19] and exhibit single exponential photobleaching kinetics under low excitation intensity. The photobleaching of conjugated polymers is more complicated due to the complex set of interactions involving a large number of species such as excitons, polarons, molecular oxygen, and fluorescence-quenching sites of unknown structure and optical properties.[63-65] Photobleaching kinetics of the aqueous CPdot suspensions were observed to vary substantially from one polymer to another (Figure 4.3c). While PFO and PFPV dots exhibit single exponential photobleaching decays, the photobleaching kinetics of MEH-PPV dots contains a fast component and a slow component. The PPE dots exhibit unusual photobleaching behavior: initial light excitation increases the fluorescence quantum yield, resulting in a rapid increase in fluorescence followed by slow photobleaching. The PFBT dots appear to be remarkably photostable – photobleaching for two hours does not result in observable decrease in fluorescence intensity. These observations indicate complex photophysics in these nanoscale multichromophoric systems, and more detailed investigations are needed to better understand how these phenomena are determined by the polymer structure and environment. An estimate of both the photobleaching quantum yield and the photon number (total number of photons that a particle emits prior to photobleaching) can be obtained from the rate constants obtained from the photobleaching kinetics measurements.[19] As shown in Table 4.1, the photon numbers of the CPdots are 3-4 orders of magnitude larger than those of typical fluorescent dyes,[19] indicating promise for long-term imaging and tracking applications.

Table 4.1 Figures of merit evaluating the multicolor conjugated polymer dots as single molecule fluorescent probes.

CPdots (Ave. dia. 15 nm) (Absorption/fluorescence max, nm)	PFO (380/435)	PPE (390/440)	PFPV (445/510)	PFBT (450/545)	MEHPPV (485/590)
Absorption cross section (σ, cm^2)	5.4×10^{-13}	4.6×10^{-13}	5.5×10^{-13}	2.8×10^{-13}	4.4×10^{-13}
Quantum yield (ϕ_F)	0.40	0.12	0.08	0.07	0.01
Fluorescence lifetime (τ, ps)	270	242	133	595	127
Radiative rate (k_r, s^{-1})	1.5×10^{9}	5.0×10^{8}	6.0×10^{8}	1.2×10^{8}	7.9×10^{7}
Photobleaching quantum yield (ϕ_B)	$\sim10^{-8}$	$\sim10^{-9}$	$\sim10^{-8}$	$\sim10^{-10}$	$\sim10^{-8}$
Photon number (photons)	$\sim10^{7}$	$\sim10^{8}$	$\sim10^{7}$	$\sim10^{9}$	$\sim10^{6}$

For high speed applications such as flow cytometry and high-speed imaging and tracking, a key figure of merit is the fluorescence radiative rate. Fluorescence decay kinetics (Figure 4.3d) were obtained using the time-correlated single photon counting technique (TCSPC) and excited state lifetimes were extracted from the kinetics traces using software written for the MATLAB environment. All decay traces of the CPdots (with the exception of the 480 nm emission band of PPE dots) can be fit adequately with a single exponential function, and the lifetime results are listed in Table 1. The lifetimes of PFPV and MEHPPV dots were determined to be ~130 ps, while β-phase PFO and PFBT dots show longer lifetimes around ~270 ps and ~600 ps, respectively. PPE dots display complex fluorescence decay kinetics, the 440 nm emission peak shows a single exponential decay with time constant of 242 ps, while the 480 nm emission exhibits a bi-exponential decay with time constants of 276 ps and 1.56 ns. This observation is similar to previously observed fluorescence decay kinetics of PPE thin films, which are characterized as a heterogeneous system containing ordered and disordered polymer chains.[58] The fluorescence radiative rate constant k_R and non-radiative rate constant k_{NR} were estimated by combining the quantum yield [$\phi = k_R/(k_R+k_{NR})$] and fluorescence lifetime results [$\tau = (k_R+k_{NR})^{-1}$]. Typical fluorescent dyes exhibit fluorescence radiative rates on the order of ~10^8 s^{-1}. As shown in Table 1, the CPdots exhibit a fluorescence radiative rate (10^{8}-10^{9} s^{-1}) similar to or somewhat higher than that of typical fluorescent dyes, while single quantum dots emit at rates about two orders of magnitude lower.[66] The fluorescence radiative rates of the CPdots are at or above those of other fluorophores used in flow cytometry and imaging.

4.3 Single particle imaging and kinetics

Single particle fluorescence imaging and kinetics studies provide further evidence of the CPdots as fluorescent probes for single molecule applications. Photobleaching studies of single PFBT dots (particle size: 10±3 nm) dispersed on a glass coverslip were performed using a custom built wide-field epifluorescence microscope. Bright, near-diffraction-limited spots corresponding to individual PFBT dots were observed (Figure 4.4a). Single particle photobleaching measurements were obtained by acquiring a series of consecutive frames. The number of fluorescence photons emitted per frame for a given particle was estimated by integrating the CCD signal over the fluorescence spot, and then scaling that value with the detector quantum efficiency and amplification factor of the analog-digital converter and the overall collection efficiency of the microscope. The photobleaching trajectories could be roughly categorized into two types exemplified by the curves shown in Figure 4.4b. Most of the particles exhibit continuous photobleaching behavior with no observable fluorescence blinking, as indicated by the green curve, while some blinking was often observed in dimmer particles (blue curve). This is consistent with the size dependent blinking observed in other conjugated polymers:[67, 68] the fluorescence of the smaller (dimmer) particles fluctuates due to the small number of emitting chromophores and the reversible on-off dynamics resulting in sizable fluctuations in the fraction of chromophores in the "on" state, while larger particles (> 10 nm dia.) result in relatively steady fluorescence there are contributions from a larger number of chromophores, resulting in smaller fluctuations. As fluorescent probes for imaging or single particle tracking, the steady fluorescence of the larger CPdots compares

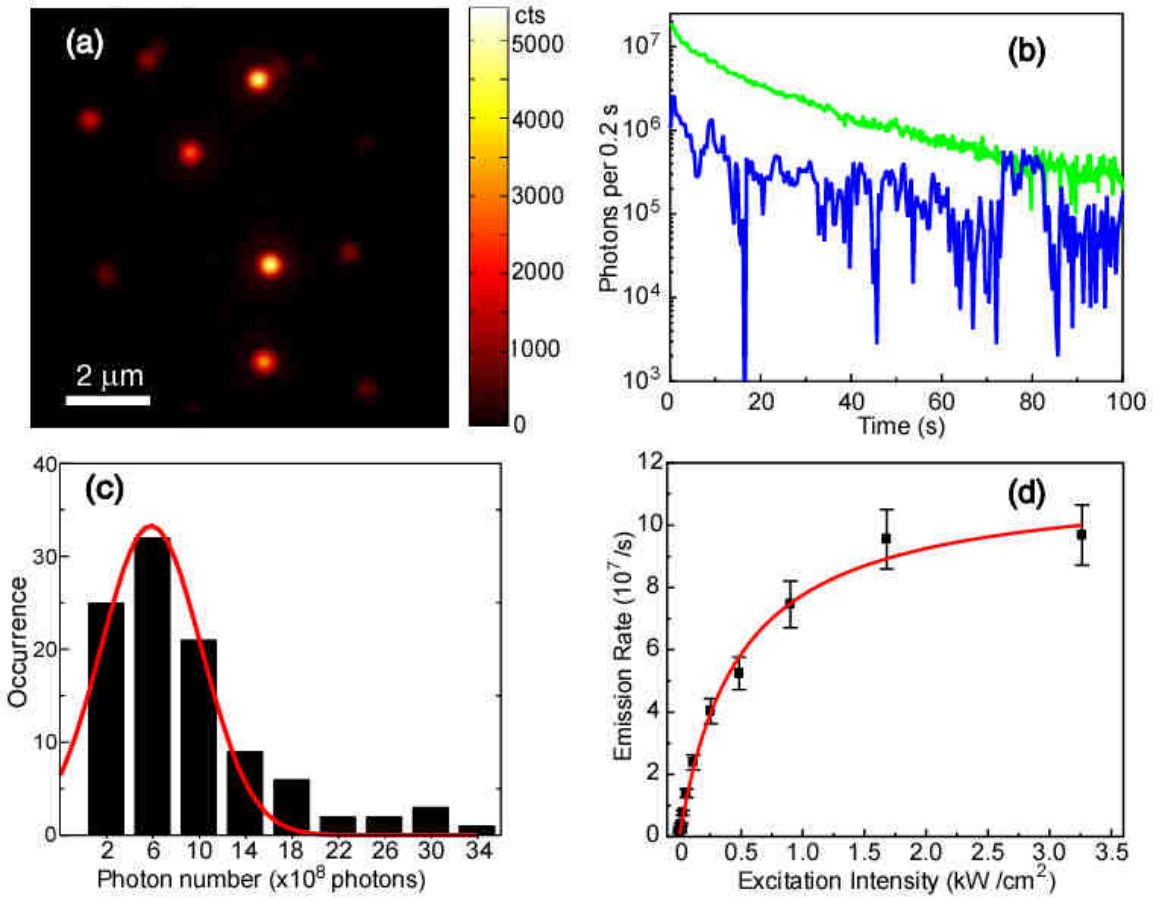

Figure 4.4 Single particle fluorescence imaging and kinetic studies of PFBT dots. (a) A 10μm×10μm fluorescence image of single PFBT dots immobilized on a glass coverslip. (b) Photobleaching trajectories of single PFBT dots. No obvious blinking was observed for larger PFBT dots (green), while it was sometimes observed for smaller particles (blue). (c) Histogram of the photon numbers of several individual PFBT dots (~10 nm) prior to irreversible photobleaching. (d) Fluorescence saturation of single PFBT dots with increasing excitation intensity. The scattered points are experimental data, while the solid curve represents a fit to the saturation equation $R = R_{\infty}(I / I_s)(1 + I / I_s)^{-1}$.

favorably to that of conventional dyes and quantum dots, which often exhibit pronounced blinking on time scales of microseconds to hundreds of seconds,[25] although there are reports that such blinking can be suppressed in some cases.[69] Statistical analyses of several photobleaching trajectories indicate that approximately ~6×10^8 photons per particle (~10 nm diameter) were emitted prior to photobleaching (Figure 4.4c). The average photon number (number of photons emitted prior to photobleaching) obtained from single particle measurements is roughly consistent with the bulk photobleaching results (given an estimated uncertainty of ~20% in the determined photon number). Additional photobleaching experiments performed under nitrogen resulted in photon numbers roughly two orders of magnitude higher, indicating that oxygen is likely involved in the photobleaching mechanism.

In single molecule experiments and other measurements involving high excitation intensities, the emission rate is often determined by saturation due to the presence of triplets and other long-lived nonfluorescent species. Typical fluorescent dyes exhibit a saturated emission rate on the order of 10^6 s^{-1} due to triplet saturation.[18] This picture is complicated for multichromophoric systems such as conjugated polymers, as evidenced by photon antibunching studies and single molecule blinking studies that indicate roughly between 1 and 3 independent emitters for single conjugated polymer chains.[70, 71] This value is much lower than the chromophore number that is expected based on the extinction coefficients and conjugation lengths of conjugated polymers, and the discrepancy can be attributed to energy transfer resulting in the funneling of excitons to a small number of emitters. Other important factors are the presence of photoinduced, long-

lived hole polarons that can act as fluorescence quenchers (typically resulting in single molecule blinking),[65, 72, 73] and exciton collisions (which can result in photon anti-bunching).[70]

Fluorescence saturation studies of single PFBT dots were performed under nitrogen protection so that photobleaching was negligible (however, the absence of oxygen also tends to increase triplet lifetimes, resulting in increased triplet saturation [74]). As shown in Figure 4.4d, the fluorescence signal of a PFBT particle shows power saturation behavior that is well described by the saturation equation $R = R_\infty (I / I_s)(1 + I / I_s)^{-1}$, where I and I_s are the excitation and the saturation intensities, respectively. From the fit of this particle, we obtain a saturation emission rate R_∞ = 1.1×10^8 s^{-1} and I_s = 0.5 $kWcm^{-2}$. Statistical analysis of several particles yielded saturation emission rates ranging from 10^7 to 10^9 s^{-1}. The mean saturation emission rate is roughly 100 times higher than that of typical molecular dyes, and at least 3 orders of magnitude higher than that of colloidal semiconductor quantum dots. The single particle saturation emission rate is markedly lower than the expected per-particle radiative rate based on the results of prior single molecule studies[70] and the number of polymer chains per nanoparticle (~40). This apparent discrepancy is likely due to the larger number of available pathways for exciton diffusion in the nanoparticles relative to single conjugated polymer molecules, resulting in additional energy funneling.

4.4 Fluorescence cellular imaging

The high absorption cross-sections, bright fluorescence, and large photon numbers of the CPdots indicate great potential for single molecule imaging and tracking

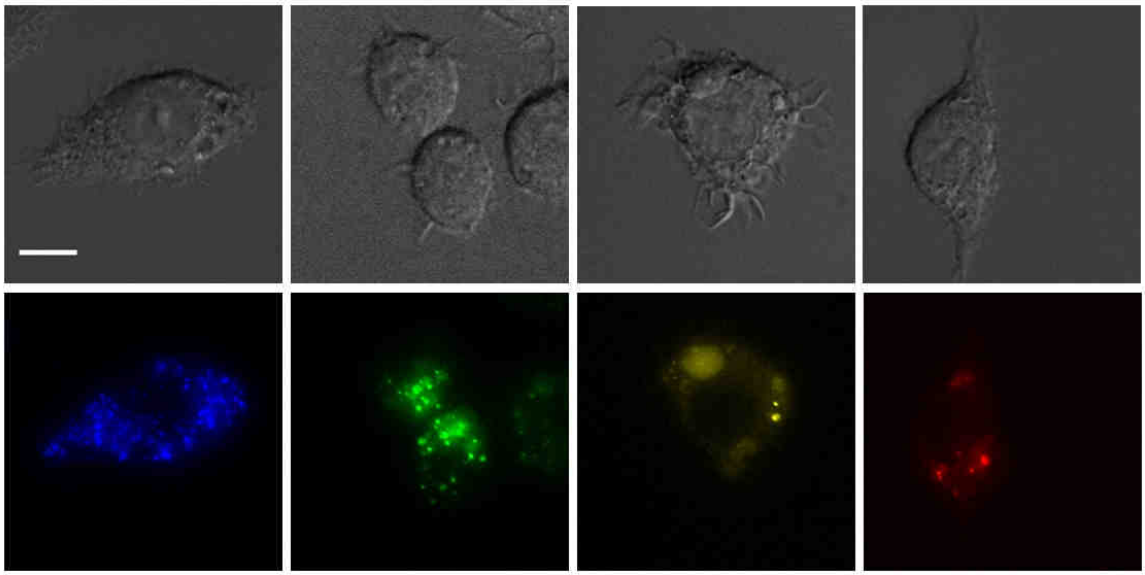

Figure 4.5 Fluorescence imaging of conjugated polymer dots in living cells. Differential interference contrast (DIC) images (top), and fluorescence images (bottom) of macrophage cells labeled with macrophage cells labeled with PPE, PFPV, PFBT and MEHPPV dots, respectively. Scale bar: 10 μm.

in living cells. As compared to membrane-permeable organic dyes, the use of nanoparticles for intracellular imaging is generally complicated by the challenge of delivering the nanoparticles to the interior of the cell.[75] A variety of strategies including invasive methods such as electroporation and microinjection have been demonstrated for intracellular delivery of inorganic quantum dots.[76] Here we demonstrate the effective use of CPdots as an extremely bright fluid phase marker of pinocytosis in J774.A1 cells. The selection of the cell system is based on the ability of macrophages to efficiently ingest cellular debris, pathogens, and small particles such as CPdots. Figure 4.5 shows differential interference contrast (DIC) images and fluorescence images of these mouse macrophage-like cells that had been incubated with PPE, PFPV, PFBT, and MEH-PPV dots, respectively. These images clearly indicate internalization of the CPdots by the cells and show a staining pattern consistent with other widely used fluid-phase markers such as an organic dye conjugated to a high molecular weight dextran. Consistent with fluid-phase uptake of CPdots, these representative images show perinuclear labeling and brightly fluorescent vacuoles and organelles (e.g. pinosomes and lysosomes). More diffuse nanoparticle fluorescence was apparently localized in the cytoplasm. This may be due to a population of CPdots that are able to cross cell membranes. Preliminary co-localization studies with Texas Red dextran and Lysotracker Red favor fluid-phase uptake as the most likely mechanism. The CPdots do not appear to exhibit appreciable cytotoxicity under the current incubation time and loading concentration. The nanoparticles also appear to be stable (no evidence of degradation) in cell growth medium. Clearly, a detailed understanding of the factors affecting nanoparticle uptake as

well as the fate of the nanoparticles requires additional investigation. In addition, imaging or tracking specific intracellular species will require targeting of the CPdots via encapsulation and bioconjugation.

4.5 Encapsulation for bioconjugation

Encapsulation is a widely used strategy to facilitate biofunctionalization of nanoparticles, and can yield improvements in photostability and quantum yield.[77-79] Condensation of active silica or alkoxysilanes on a particle surface to form a silica shell is a proven method for particle encapsulation and also provides a surface that can be further functionalized by a variety of methods.[22, 77-79] The presence of oxide or hydroxy groups on the surface of the nanoparticle is required to promote adhesion and polymerization of a silica shell. Therefore a promoter is required for shell formation on noble metal or hydrophobic polymer particles.[80, 81] Here we choose octyltrimethoxysilane (OTMOS) to promote silica shell formation. Hydrolysis of the alkoxy groups results in the formation of a rigid micelle-like structure around the polymer core with oxygen bridges between silicon atoms and silanol groups on the surface as illustrated in Figure 4.6 (Top).[82] A 4-5 nm thick silica shell is grown by subsequent addition and polymerization of tetraethyl orthosilicate (TEOS). The amine or thiol functionalization is further achieved by reaction of amine-silane or thiol-silane with the silica surface. Poly(ethylene glycol) (PEG) groups can be introduced at the same time to make the particles biocompatible and avoid non-specific interactions. Certain biomolecules are finally conjugated with the polymer nanoparticles through a biolinker molecule such as succinimidyl-4-(N-maleimidomethyl)cyclohexane-1-carboxylate (SMCC).

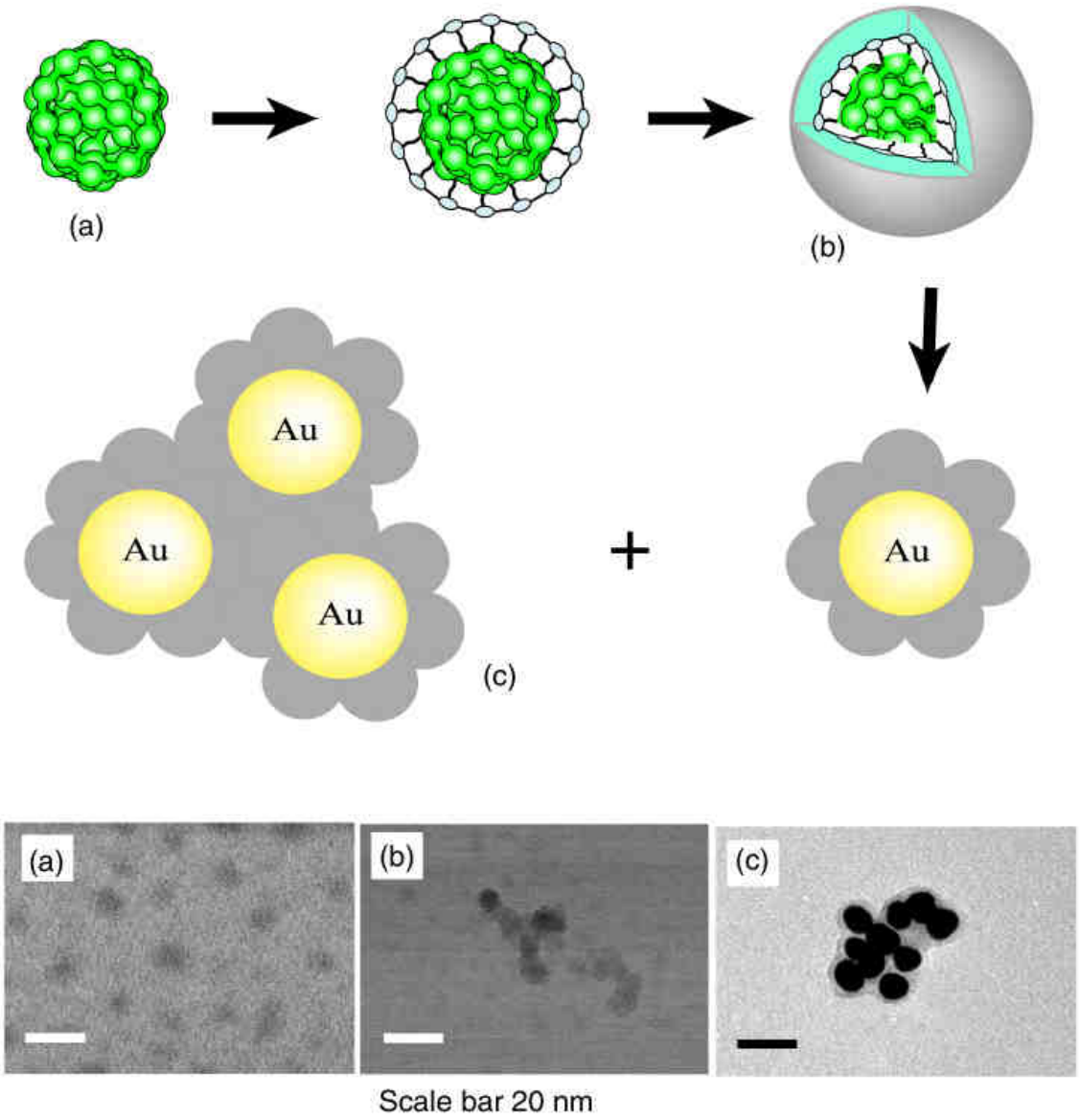

Figure 4.6 Encapsulation scheme of conjugated polymer dots. The bottom shows TEM images of bare MEH-PPV nanoparticles (a), silica-encapsulated nanoparticle (b), and assembled MEH-PPV/Au nanostructures (c).

As an additional test of the silica encapsulation of the nanoparticles, the binding of surface-functionalized nanoparticles to gold nanoparticles was characterized by fluorescence spectroscopy and TEM. Gold nanoparticles have been found to efficiently quench the fluorescence of water-soluble conjugated polymers, as indicated by extremely large Stern-Volmer constants (K_{SV}).[35] The gold nanoparticles (15 nm) were prepared according to the standard sodium citrate reduction method.[83] The silica-encapsulated polymer nanoparticles were functionalized with amine groups using a silane coupling agent 3-aminopropyltrimethoxysilane (APTMS). Amines are known to bind strongly to the surface of gold nanoparticles.[81, 84] TEM observations (Figure 4.6c) indicate the coexistence of single gold/polymer nanostructures and some gold/polymer aggregates. It is clearly observed that each gold nanoparticle was coated with a rough shell composed of several silica-encapsulated polymer nanoparticles. Spectroscopic measurements were performed on the two aqueous dispersions of the Au/PFPV and Au/MEH-PPV nanostructures, one of which contains PFPV (8 nM) and gold nanoparticles (0.5 nM), the other has MEH-PPV (12 nM) and gold (0.5 nM), respectively. Binding with gold nanoparticles resulted in fluorescence quenching of ~33% for PFPV and ~50% for MEH-PPV nanoparticles, respectively. Assuming a linear Stern-Volmer relation in the experimental concentration range, the K_{SV} values were estimated to be quite large: $\sim 1\times10^{9}$ M^{-1} for PFPV and $\sim 2\times10^{9}$ M^{-1} for MEH-PPV, similar to the "hyperquenching" reported for conjugated polymer electrolytes complexed with Au nanoparticles.[35] Fluorescence spectra of free polymer and gold nanoparticle mixtures in absence of APTMS indicated no quenching except for a small inner filter effect. While the

quenching mechanism has not yet been fully investigated, it is likely that the efficient quenching is due to the large extinction coefficient of the Au nanoparticle, with perhaps some contribution due to fast intraparticle energy transfer within the conjugated polymer nanoparticle. Electron transfer has also been observed as a mechanism for quenching of conjugated polymer fluorescence,[34] but in this case electron transfer is likely blocked by the silica shell.

CHAPTER 5 CONJUGATED POLYMER DOTS FOR MULTIPHOTON FLUORESCENCE IMAGING

Multiphoton fluorescence microcopy has recently emerged as a powerful technique for three-dimensional imaging in biological systems.[85-88] The nonlinear dependence of excitation probability on light intensity results in a highly localized excitation and improved spatial resolution. The small effective excitation volume also reduces background signal due to autofluorescence and the fluorescence of dye molecules outside of the laser focal volume, while the ability to employ near IR wavelengths for excitation can reduce photodamage to the sample as well as facilitate imaging of biological specimens due to the near-transparency of many tissues in this spectral range.[88] The widespread adoption of multiphoton fluorescence imaging and microscopy has been hindered by the bulky and expensive pulsed laser sources typically required for excitation due to the relatively low multiphoton excitation cross-sections of available dyes.[49, 89] Interest in the development of brighter probes has led to the design and synthesis of dyes with two-photon action cross sections larger than 1000 Göppert-Mayer units (GM).[90] Gold nanorods have also been demonstrated as contrast agent for *in vitro* and *in vivo* two-photon luminescence imaging, and the two-photon action cross sections were determined to be ~2000 GM.[91] Colloidal CdSe quantum dots appear to be very promising probes for two-photon microscopy due to their excellent photostability and large two-photon action

cross sections (from 2000 to 47000 GM),[92] although single particle blinking and a significant fraction of "dark" dots are drawbacks for some applications.[25]

In this chapter, we investigate the two-photon excited fluorescence of CPdots. As a new class of two-photon fluorescent probes, CPdots exhibit two-photon action cross sections as high as 2.0×10^5 GM, to our knowledge the largest reported thus far for a nanoparticle. The cross section values are three to four orders of magnitude higher than conventional fluorescent dyes, and an order of magnitude higher than inorganic quantum dots. Demonstration of single particle imaging using relatively low laser excitation levels demonstrates the potential utility of CPdots for multiphoton fluorescence microscopy applications and raises the possibility of employing small, inexpensive near infrared diode lasers for two-photon excited fluorescence imaging. The major results presented in this chapter have appeared previously in a published journal article.[68]

5.1 Two-photon excited fluorescence

The CPdots exhibit one-photon absorption in the wavelength range of 350 nm - 550 nm, as shown in Chapter 4. However, when the output of a mode-locked Ti:sapphire laser (100 mW, 800 nm, 100 fs) is focused into aqueous dispersions of PFPV and MEH-PPV dots (8 ppm, 3 nM), strong fluorescence in the vicinity of the focus is clearly visible (Figure 5.1a). Power-dependent excitation efficiencies provide further evidence for the two-photon excited fluorescence (Figure 5.1b). At a given laser intensity *I*, two-photon fluorescence intensity is proportional to $\sigma_{2p}\phi_F I^2$, where σ_{2p} is the two-photon absorption cross-section and ϕ_F is the fluorescence quantum yield. A convenient measure of the two-photon fluorescence brightness is the two-photon action cross section, $\sigma_{2p}^{*}=\sigma_{2p}\phi_F$.[88, 92]

The measurements were performed on CPdots of ~20 nm diameter (Figure 5.1c), consisting of PDHF, PFPV, and MEH-PPV, respectively. A custom built photon-counting spectrometer (described in Chapter 3.2) was used to determine the two-photon action cross sections, which were obtained from the fluorescence data as follows.

The time-averaged detected fluorescence photon flux *F(t)* can be expressed as

$$\langle F(t)\rangle \approx \frac{1}{2}\eta C\sigma_{2p}^{*}\frac{g_p}{f\tau}\frac{8n\langle P(t)\rangle^2}{\pi\lambda}, \tag{5.1}$$

where η is the fluorescence collection efficiency of the instrument; *C* is the fluorophore concentration; σ_{2p}^{*} is two-photon action cross section of the probe; g_p is a unitless factor related to pulse shape (0.66 for Gaussian laser pulse); *f* is the laser repetition rate; τ is the width (FWHM) of the laser pulse; *n* is the refractive index of the lens focusing the laser beam; λ is the laser wavelength; and <*P(t)*> is the average power of the laser.[49] The factor $g_p/(f\tau)$ is approximately 10^5 for a Ti:sapphire laser with a 76 MHz repetition rate and 100 *fs* pulses. Only *C* and σ_{2p}^{*} are related to the sample, and all other parameters are determined by the measurement system and conditions. Varying the laser power <*P(t)*> and recording the fluorescence intensity <*P(t)*> yields a quadratic dependence of fluorescence intensity on laser power. According to the above equation, a plot of $Ln\langle F(t)\rangle$ versus $Ln\langle P(t)\rangle$ results in a straight line with slope of 2 and an intercept *b*, given by the expression,

$$\mathrm{b} = Ln(\frac{1}{2}\eta C\sigma_{2p}^{*}\frac{g_p}{f\tau}\frac{8n}{\pi\lambda}) \tag{5.2}$$

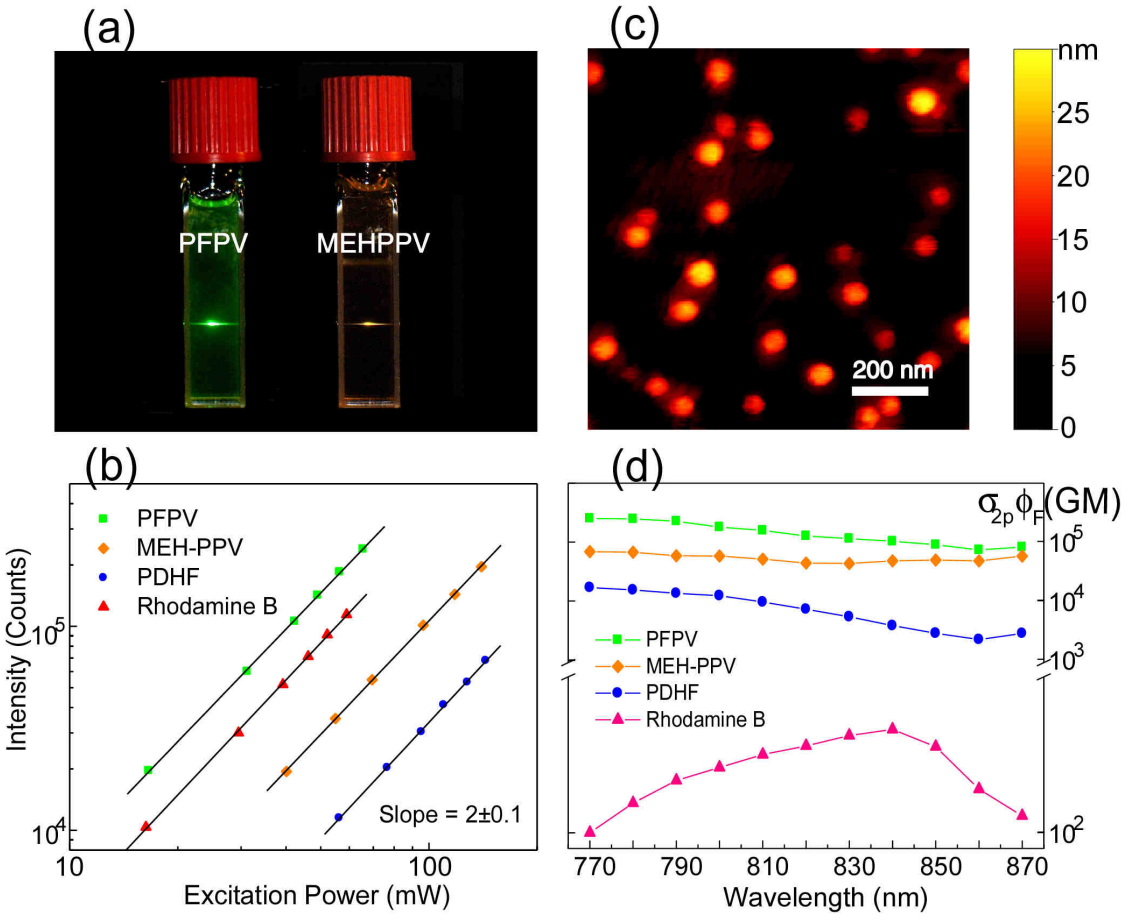

Figure 5.1 Two-photon excited fluorescence from conjugated polymer dots. (a) Photograph of the fluorescence from aqueous CPdot dispersions under two-photon excitation of an 800 nm mode-locked Ti:sapphire laser. (b) Log-log plot of two-photon fluorescence intensities versus the excitation power for the CPdots and rhodamine B (reference compound). (c) A typical AFM images of the PFPV dots on a silicon substrate. (d) Semi-log plot of two-photon action cross sections ($\sigma_{2p}\phi$) versus the excitation wavelength for the CPdots and rhodamine B.

Provided that a standard dye with known two-photon action cross-section is available, a relative determination of the two-photon action cross section of the species of interest is given by the expression,

$$\sigma_{2p}^{*} = \sigma_{2p,0}^{*} \frac{C_0}{C} \exp(b - b_0) \tag{5.3}$$

where b and b_0 are obtained from log-log plots of laser intensity versus fluorescence intensity for the fluorophore of interest and the standard, respectively, and $\sigma_{2p,0}^{*}$ is the two-photon action cross-section of the standard. The above method was validated by determining the two photon action spectrum of rhodamine B using Lucifer yellow as a standard. The determined two photon action spectrum for rhodamine B is consistent with literature results for the absolute two-photon action cross-section.[49] Figure 5.2b shows the log-log plot of the fluorescence intensities of the CPdots and rhodamine B solutions versus the laser power at 800 nm wavelength. Fits to the experimental data yield a slope of 2.0±0.1, consistent with two-photon excited fluorescence. The sample concentrations were determined by UV-Vis absorption measurement (The method for determining the nanoparticle concentration was described in Chapter 4).

The experimentally determined two-photon action cross sections (λ_{ex}=770 nm) are 1.4×10^4 GM, 5.5×10^4 GM, and 2.0×10^5 GM for PDHF, MEH-PPV, and PFPV dots, respectively (Figure 5.1d). The two-photon action cross-section for MEH-PPV dots is about one order of magnitude larger than that of the polymer molecules in solution,[93] consistent with the particle size results that indicate 10-20 molecules per particle. Significantly, the results show that, as two-photon fluorescent probes, the PFPV dots are

three to four orders of magnitude brighter than conventional fluorescent dyes,[49] and an order of magnitude brighter than quantum dots.[92] It is somewhat surprising that PFPV dots were determined to have the highest brightness of the three polymers, given that under one-photon excitation PDHF dots are brighter than both PFPV and MEH-PPV dots. However, the higher two-photon cross sections of PFPV and MEH-PPV are consistent with theoretical and experimental results indicating that π-conjugated systems with alternating donor-π-donor structures exhibit relatively large two-photon absorption cross sections due to the increased hyperpolarizability of such structures.[90, 94] The alkoxy side groups in PFPV and MEH-PPV act as electron donors, forming the donor-π-donor motif associated with relatively high two-photon cross sections, while PDHF does not possess alkoxy side groups.

5.2 Single particle imaging with two-photon excitation

To demonstrate the potential of the CPdots for multiphoton fluorescence imaging, single particles on a glass substrate were imaged using a custom built confocal fluorescence microscope employing the attenuated output of a mode-locked Ti:sapphire laser (800 nm, 100 fs, 76 MHz repetition rate) for excitation. Figure 5.2a shows a 5μm×5μm fluorescence image of the PFPV dots sparsely dispersed on a glass coverslip. Each bright spot in the Figure 5.2a corresponds to a single PFPV dot. The high per-particle brightness is evident in the relatively low average laser power (260 μW, at the sample) employed to obtain high contrast images. The fluorescence detection efficiency was determined to be 5-7%, using dye-loaded nanospheres (Invitrogen) as standards. Typical single particle fluorescence count rates of 25 kHz were observed. Analysis of

fluorescence spots in the single molecule image (Figure 5.2a) yields an estimate of the full-width at half-maximum of around 450 nm, somewhat above the diffraction limit. Based on visual inspection of the laser mode and consideration of the optics used to couple the laser to the microscope, we believe that improved resolution could be achieved by spatial filtering of the output of the Ti:Sapphire laser, as has been demonstrated.[95] Based on the determined focal characteristics of the laser and the two-photon action cross-section (2.0×10^4 GM for ~10 nm nanoparticle), it is estimated that ~32 μW average power (at the sample) would be required to attain this 25 kHz signal level (assuming 100 fs pulses and 6% detection efficiency). This factor of 8 discrepancy is reasonable given that there are a number of factors that are difficult to quantify and were not taken into account, such as group velocity dispersion due to passage of the laser pulse through various optics resulting in stretched pulses, non-ideal beam profile, and non-optimal alignment. Typically, pulsed laser light is required to generate sufficient two-photon fluorescence signal for single fluorophore detection. However, the observed modest intensity requirements for multiphoton imaging raise the possibility of employing CW excitation for multiphoton imaging. Based on these results, we estimate it should be possible to obtain two-photon fluorescence images of single CPdot nanoparticles using ~10 mW CW laser illumination provided by an inexpensive semiconductor diode laser. Indeed, focusing several tens of mW of 800 nm CW laser light (Ti:sapphire laser operating in CW mode) onto a single layer of nanoparticles generated fluorescence that was readily visible to the unaided eye.

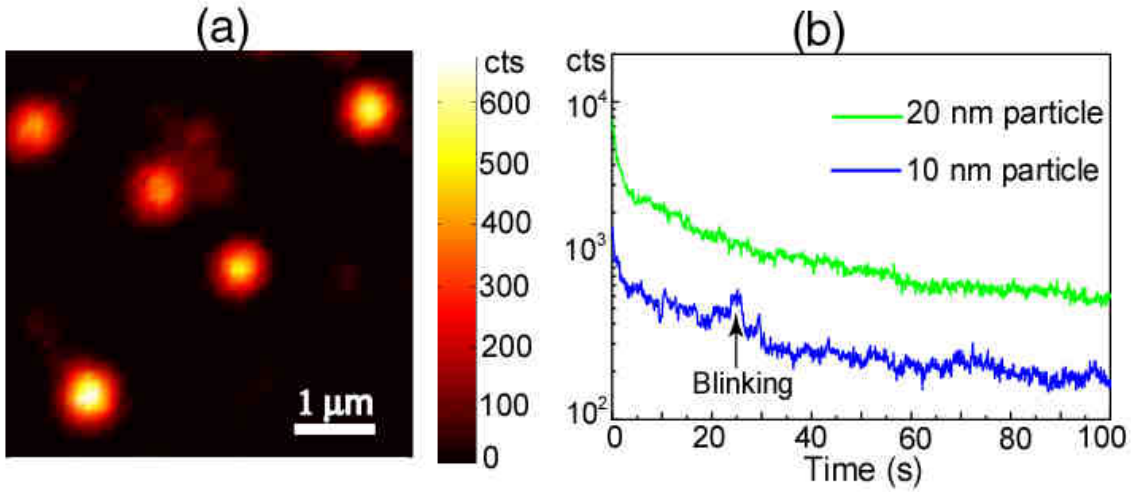

Figure 5.2 Single particle fluorescence imaging and kinetics of PFPV dots with two-photon excitation. (a) A 5μm×5μm fluorescence image of single PFPV dots immobilized on a glass coverslip obtained using two-photon excitation (800 nm). (b) Photobleaching kinetics of single PFPV dots under two-photon excitation. No obvious blinking was observed for ~20 nm PFPV dots, while it is often observed for smaller particles (<10 nm).

Single conjugated polymer molecules typically exhibit complex photophysics such as fluorescence intermittence (blinking) and photon antibunching.[70, 96] Single particle fluorescence kinetics traces (Figure 5.2b) obtained with two-photon excitation indicated no observable blinking for 20 nm PFPV dots, while it was often observed in smaller particles (<10 nm), consistent with single particle results with one-photon excitation. As fluorescent probes for imaging or single particle tracking, the relatively steady fluorescence of CPdots compares favorably to that of quantum dots, which typically exhibit pronounced blinking on time scales of milliseconds to hundreds of seconds.[25] Analyses of single particle kinetics traces indicate that approximately ~10^6 photons per particle (~10 nm diameter) were detected prior to photobleaching. This is lower than the photostability under one-photon excitation (~10^7 photons detected), consistent with prior observations that single fluorophores exhibit lower photostability under two-photon excitation than under one-photon excitation.[95] The demonstration of single particle imaging and the large two-photon action cross sections clearly indicate the potential utility of CPdots for multiphoton fluorescence microscopy applications.

CHAPTER 6 ENERGY TRANSFER MEDIATED FLUORESCENCE IN BLENDED CONJUGATED POLYMER DOTS

Single conjugated polymer molecules and conjugated polymer aggregates exhibit complex photophysics and surprising phenomena such as blinking and photon antibunching,[70] which are attributable to a variety of photophyical processes that occur in such complex systems.[97-101] Energy transfer in nanoscale systems has recently been demonstrated as the basis of molecular beacons for efficient detection of biomolecule interactions and dynamics.[40, 102, 103] Our understanding of the photophysics of such systems is currently limited by the lack of experimental results on well-behaved model systems and by difficulties in interpreting their behavior. Nanoparticles and nanoparticle assemblies are typically heterogeneous systems. Analysis of energy transfer in nanoparticles of mixed composition or in donor-acceptor nanoparticle assemblies is complicated by the fact that, in many cases, there are a small number of quenchers per molecule, resulting in a statistical distribution of energy acceptors and significant particle-to-particle variations in quenching efficiency. In such systems, there can be significant deviations from Stern-Volmer quenching theory.[35, 104, 105]

In this chapter, we report on energy transfer mediated fluorescence from conjugated polymer nanoparticles consisting of polyfluorene (PDHF) doped with three different conjugated polymer acceptors. The blended conjugated polymer nanoparticles exhibit fluorescence excitation spectra characteristic of the host polymer, and the

fluorescence emission spectra characteristic of the dopant polymer. Stern-Volmer analysis of the host fluorescence as a function of dopant concentration indicates efficient energy transfer from a hundred or more host polymer molecules to a *single* dopant polymer molecule. We present an energy transfer model which yields population-averaged quenching efficiencies for the case of a statistical distribution of a small number of highly efficient energy acceptors per nanoparticle. For the doped conjugated polymer nanoparticles, the model successfully reproduces the observed dependence of quenching efficiency on average particle composition over a wide range. The major results presented in this chapter have appeared previously in a published journal article.[106]

6.1 Blended conjugated polymer dots

Since the hydrophobic interaction is the primary driving force for nanoparticle formation, it is possible to introduce different hydrophobic polymer species during nanoparticle formation. Blended polymer dots were obtained by quickly adding a solution mixture to water under simultaneous sonication to improve mixing, as described in Chapter 3.1. PDHF was chosen as the host polymer in view of its high absorptivity in the near ultraviolet region and favorable spectral overlap with the dopant polymers employed in this study. After removal of a small fraction of aggregates by filtration and removal of THF by partial vacuum evaporation, the composition of the resulting dispersion is consistent with the relative amounts of PDHF and dopant in the precursor solution mixture, as determined by UV-Vis absorption spectroscopy. The nanoparticle dispersions were drop-cast onto silicon substrates for analysis of particle size and morphology by tapping-mode AFM. A representative AFM image of polymer blend nanoparticles is

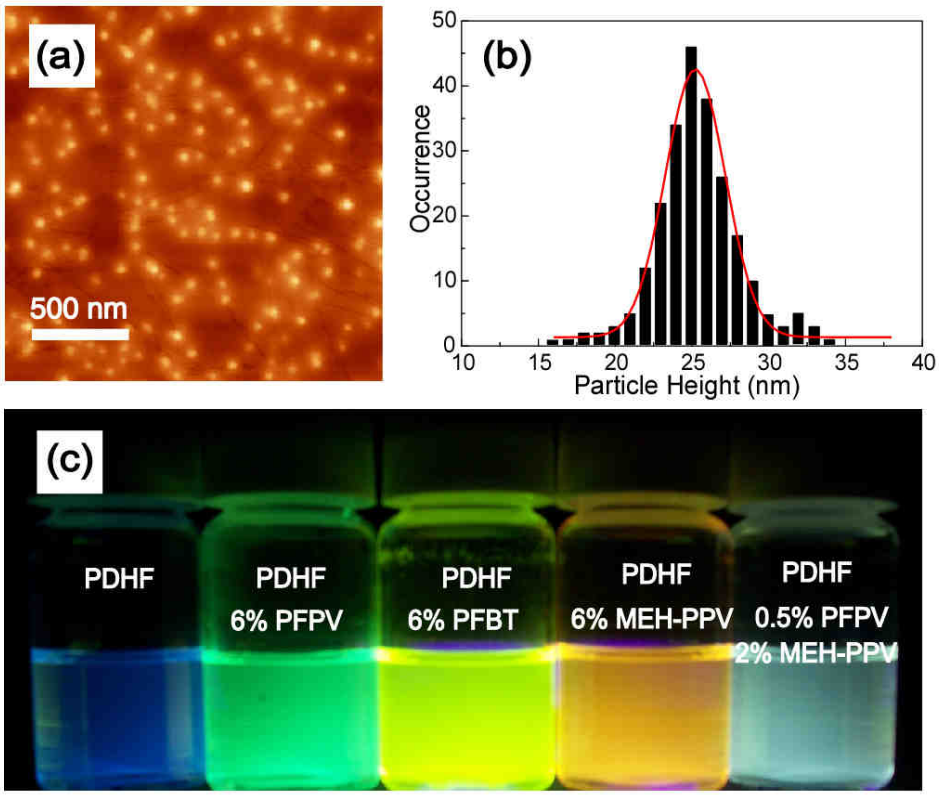

Figure 6.1 Nanoparticle size and morphology of blended conjugated polymer dots. (a) A representative AFM image of blend dots. (b) Histogram of particle height taken from AFM image. (c) Photograph of fluorescence emission from aqueous suspensions of the blend nanoparticles taken under a UV lamp (365 nm).

shown in Figure 6.1a. A particle height histogram obtained from the AFM image indicates that most particles possess diameters in the range of 20-30 nm, as shown in Figure 6.1b. The lateral dimensions are also in the range of 20-30 nm after the tip width is taken into account.[107] The morphology is consistent with the recent observation that the equilibrium shape for small sized PDHF nanoparticles (<30 nm) tends to be spherical because surface tension effects determine the morphology in this size range.[108] There are an estimated 100-200 polymer molecules per nanoparticle, assuming densely packed spherical particles. The presence of dopant has no apparent effect on particle size and morphology.

6.2 Energy transfer in blended polymer dots

Energy transfer in conjugated polymer blends has recently been demonstrated as a viable strategy for improving the quantum efficiency and tuning the emission color of optoelectronic devices.[109-112] However, segregation of the polymer species frequently occurs, causing low energy transfer efficiency. Unlike previously reported methods of producing blended conjugated polymer nanostructures,[31, 113] in which there is spectroscopic evidence of polymer segregation, the nanoparticles reported here are produced by a rapid mixing process which apparently reduces the degree of segregation, as evidenced by the efficient energy transfer from the host to guest molecules and the lack of dopant aggregate features in the spectrum. Figure 6.1d illustrates the evolution of the fluorescence color as the dopant species is varied for aqueous suspensions of nanoparticles under UV lamp excitation (365 nm). At a dopant fraction of 6 weight percent, the fluorescence from PDHF is almost completely quenched and the blend

nanoparticles present strong fluorescence from the dopant species. This result indicates highly efficient energy transfer from the host to dopant polymers. Fluorescence spectroscopy and energy transfer phenomena in these blend nanoparticles are discussed in detail below.

Figure 6.2 (left) presents the normalized absorption and fluorescence emission spectra of the conjugated polymers PDHF, PFPV, PFBT, and MEH-PPV in THF solutions. PDHF, PFPV, PFBT, and MEH-PPV exhibit their peak fluorescence at around 415 nm, 500 nm, 535 nm, and 550 nm, respectively. Conjugated polymers typically have a small Stokes shift between absorption and fluorescence, similar to that of many organic fluorescent dyes, though the combined effects of energetic disorder, energy transfer and the presence of aggregate species can lead to larger shifts.[56, 114] The pure PDHF dots (Figure 6.2, right) show a broadened and blue-shifted absorption as compared to that of the PDHF in THF solution, which is consistent with an overall decrease in the conjugation length induced by bending or kinking of the polymer backbone.[115] The fluorescence spectrum of the PDHF dots is red-shifted by 15 nm relative to that of PDHF in THF solutions. Since the nanoparticles possess a compact structure, the red-shift in fluorescence can be attributed to increased interchain interactions, leading to energy transfer to low-energy chromophores and weakly-fluorescent aggregates.[46] The fluorescence emission spectrum of the nanoparticles also has a long red tail, consistent with the presence of aggregate species. Similar features are observed in the fluorescence emission spectra of PDHF thin films.[116, 117] The fluorescence of the host polymer overlap

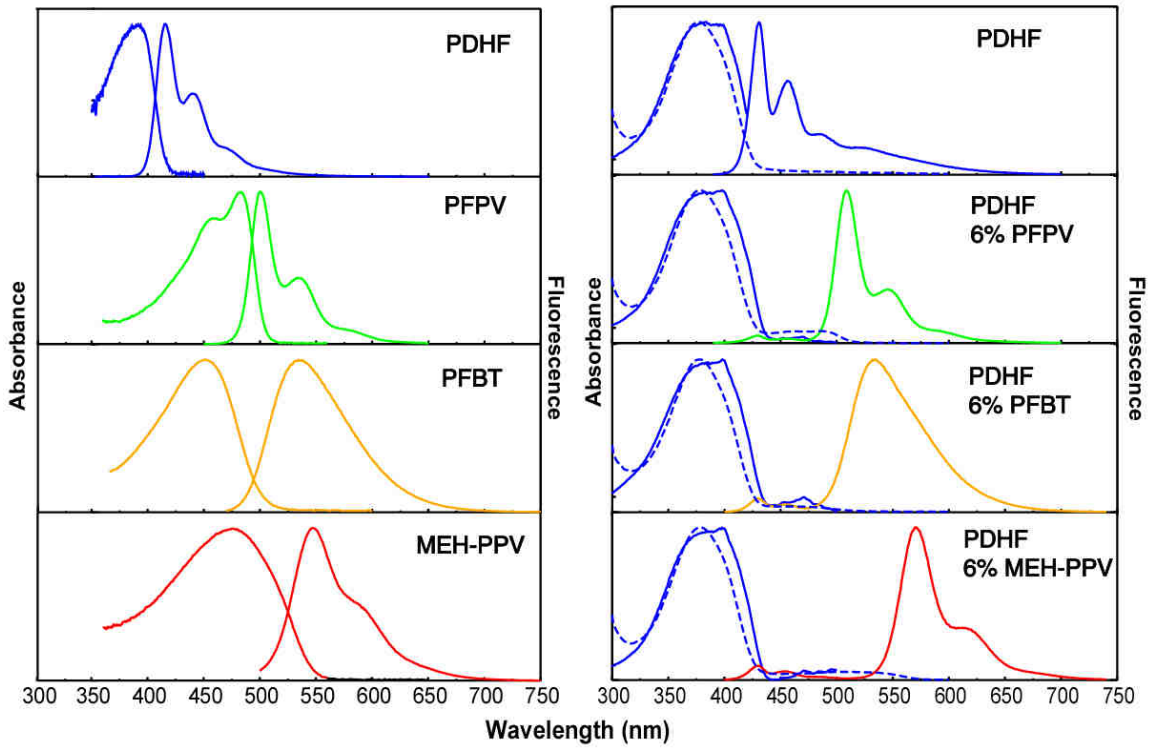

Figure 6.2 Normalized absorption (dashed), fluorescence excitation and emission spectra (solid) of blended conjugated polymer dots. The left shows the normalized absorption and emission spectra of the conjugated polymer in THF solutions.

with the absorption spectra of the three dopant polymers, as required for efficient energy transfer via the Förster mechanism.

Figure 6.2 (right) shows the normalized absorption (dashed curves), fluorescence excitation and emission spectra (solid curves) of the pure PDHF and three different blended polymer dots containing 6wt% dopant PFPV, PFBT, and MEH-PPV, respectively. The dominant absorption peaks (around 375 nm) of the blend nanoparticles are consistent with PDHF, while the weak absorption peaks in the 400-500 nm range originate from the dopant polymers. With 375 nm excitation, where >95% of the absorption is due to PDHF, the fluorescence from PDHF is almost completely quenched, and the nanoparticles exhibit fluorescence emission spectra characteristic of the dopant species. Fluorescence excitation spectra (obtained with the collection wavelength set to match the dopant emission) are very similar to the normalized absorbance spectra of PDHF (with minor differences attributable to the spectrum of the Xe lamp of the fluorometer). These observations indicate efficient intra-particle energy transfer from the PDHF host to the dopant polymer and are consistent with a low degree of segregation of the dopant polymer. For comparison, the mixed THF solutions of PDHF and dopant polymers with the same concentration were prepared and no quenching can be observed in solution phase, indicating that the host and dopant are required to be in close proximity for substantial energy transfer to occur. The observed energy transfer is consistent with a Förster mechanism,[118] though other mechanisms, such as Dexter transfer,[119] cannot be ruled out due to the close proximity of host and guest molecules. A significant feature of the blend nanoparticles is the enlarged energy gap between absorption and fluorescence

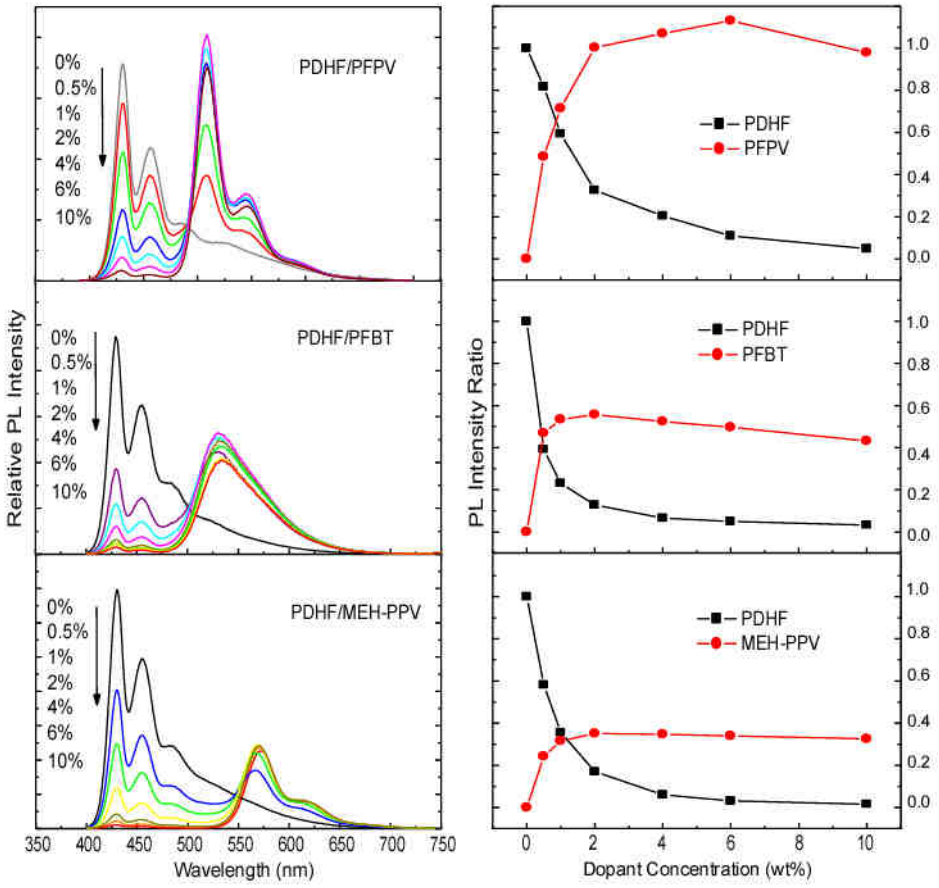

Figure 6.3 Concentration dependent fluorescence spectra of blended polymer dots under 375 nm excitation. The right shows fluorescence intensity change of PDHF host and dopant polymers as a function of dopant concentration in blend nanoparticles. All fluorescence intensities were normalized to the 430 nm emission of pure PDHF dots.

as compared to the polymers in THF solutions and pure polymer nanoparticles.[46] In addition, nanoparticles with different emission wavelengths can be simultaneously excited using a single light source, a useful feature for multiplexed fluorescence detection.

Highly efficient energy transfer is evident in the evolution of the fluorescence spectra with increasing dopant concentration. Figure 6.3 (left) shows the fluorescence emission spectra of the three types of blend nanoparticles as dopant concentration is increased. As exemplified by PDHF/PFPV system, the fluorescence from the PDHF host decreases with increasing PFPV content, while that from PFPV increases and reaches a maximum around 6wt%, after which a further increase in dopant concentration causes a slight reduction in fluorescence intensity. Over a concentration range of 2%-6%, the PDHF/PFPV nanoparticles present an intense characteristic emission (510 nm) from PFPV, which is slightly larger than the 430 nm emission from pure (undoped) PDHF nanoparticles. The other two types of blend nanoparticles show a similar trend in the host fluorescence, but lower dopant fluorescence intensity, consistent with the lower fluorescence quantum yields of PFBT and MEH-PPV as compared to PFPV. In view of the low dopant concentration and rapid nanoparticle formation, together with spectroscopic evidence which indicates an absence of aggregate species, we conclude that the dopant polymer molecules are likely uniformly distributed in the PDHF host, without significant segregation or aggregation. In addition, the lack of aggregate features (which are typically associated with reductions in quantum yield) indicates that a higher

fluorescence quantum yield can be achieved in polymer blend system as compared with the pure polymer nanoparticles.

6.3 Nanoparticle energy transfer model

The dependence of host polymer fluorescence intensity on the concentration of dopant (quencher) was modeled using the Stern-Volmer relation, which can be expressed as,[118]

$$F_0 / F = 1 + K_{SV}[Q] \tag{6.1}$$

where F_0 and F are fluorescence intensities in the absence and presence of quencher, respectively, K_{SV} is the Stern-Volmer quenching constant, and [Q] is the concentration of the quencher. The quenching constant is obtained from the slope of a linear fit to a plot of F_0 / F versus [Q]. However, deviations from the linear relationship can be observed when quenching efficiencies are very high, as observed in the super-quenching of conjugated polyelectrolytes by gold nanoparticles.[35] For the polymer blend nanoparticles using PFPV or MEH-PPV as quenchers, the F_0 / F data deviated substantially from the linear Stern-Volmer relation, while those of PFBT quenchers follow a linear Stern-Volmer behavior over a wide concentration range (Figure 6.4). If the quencher concentration is expressed as a molecule fraction, the K_{SV} obtained from the plot then represents the number of host molecules quenched by a single quencher. This analysis (Figure 6.4, solid) indicated that ~65 PDHF molecules are quenched by a single PFBT molecule, and more than 500 PDHF molecules are quenched by single molecules of either PFPV or MEH-PPV.

The combination of highly efficient energy transfer and statistical variations in the number of quencher molecules per nanoparticle are likely to cause significant deviations from the Stern-Volmer relationship. Here we introduce a nanoparticle energy transfer model which takes into account the effect of multiple quencher species per nanoparticle and the statistical distribution of quenchers. If we assume that the overall energy transfer rate scales linearly with the number of quenchers, then the host quantum yield is given by the expression

$$\phi = \frac{k_R}{k_R + k_{NR} + nk_{ET}}, \tag{6.2}$$

where k_R and k_{NR} are the radiative and non-radiative rates of the host, k_{ET} is the energy transfer rate of a single quencher, and n is the number of quenchers present in the nanoparticle. The fraction of nanoparticles with n quenchers per nanoparticle can be described by the Poisson probability distribution function

$$P(n,\bar{n}) = \frac{(\bar{n})^n}{n!\exp(\bar{n})}, \tag{6.3}$$

where $\bar{n}$ is the average number of donor molecules per nanoparticle. Combining this with the above rate expression and introducing a quenching efficiency parameter q given by

$$q = \frac{k_{ET}}{k_{ET} + k_R + k_{NR}}, \tag{6.4}$$

which yields the expression,

$$\frac{F}{F_0} = \sum_n \frac{P(n,\bar{n})}{1 + nq/(1-q)}. \tag{6.5}$$

This equation relates the relative fluorescence intensity (F/F_0) to the quenching efficiency per quencher molecule (q) and the statistical distribution of quencher molecules per nanoparticle. While the model yields results similar to the linear Stern-Volmer model for small values of q, above q = 0.5 there are substantial deviations associated with the Poisson statistics. A similar approach, with somewhat different assumptions, was developed by Turro and Yekta for applying fluorescence quenching methods to determine the aggregation number of surfactant micelles.[120]

In applying the nanoparticle energy transfer model to the data of Figure 6.3, it was assumed that $\bar{n} = fN$ where f is the molecular fraction of quenchers (estimated from the dopant weight fraction and the molecular weights of the PDHF and quencher) and N is the number of donor molecules. The quencher efficiency q and the nanoparticle particle size N were adjusted to obtain the best fit to the data. Figure 6.4 shows the experimental (scattered squares) and fit results (dashed lines) for the fluorescence quenching of PDHF donor by three different quenchers in polymer blend nanoparticles. In each case, the fit is better than that obtained from the Stern-Volmer analysis, particularly at high quencher fractions. For the case of PFBT as quencher, the fit yielded parameters N = 125 and q = 0.32. N = 125 represents the average number of molecules per nanoparticle, which is in good agreement with the value estimated from AFM measurements. q = 0.32 indicates that 32% of the fluorescence of a PDHF nanoparticle would be quenched by a single PFBT molecule, similar to the phenomenon of superquenching observed in nanoparticle assembled dye aggregates.[105, 121] The model was also fit to the results obtained using PFPV and MEH-PPV as quenchers. The N parameter obtained from the fit is ~200

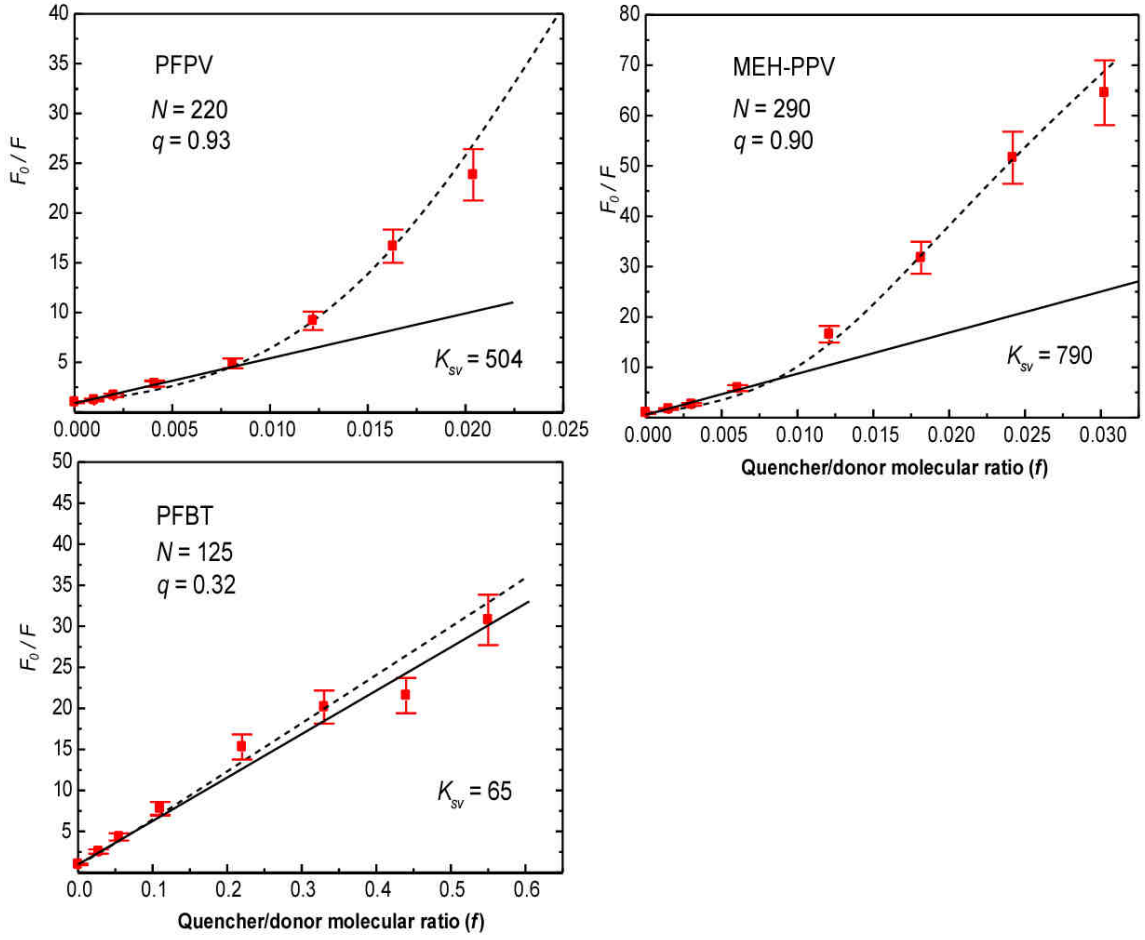

Figure 6.4 Fluorescence quenching of PDHF donor versus molar fraction of quenchers in blended polymer dots. The scattered squares are experimental data, while the black dashed curves are model results given by Equation 6.5. The solid lines represent linear Stern-Volmer plots of PF fluorescence quenched by three quenchers in low concentration range. The parameters used in the fitting are listed in the figure.

molecules per nanoparticle, corresponding to a particle diameter of ~30 nm, slightly larger than that obtained from AFM measurements. It is likely that the deviation in N is related to the quencher polydispersity and other factors not taken into account in the model. Interestingly, the large quenching efficiency (q = ~0.9) obtained for PFPV and MEH-PPV molecules indicates that the fluorescence from a PDHF nanoparticle consisting of 100-200 molecules could be nearly completely quenched by a single PFPV or MEH-PPV molecule. Considering Förster resonance energy transfer as the dominant mechanism in the quenching process, the difference between the quenching efficiency of PFBT and that of PFPV and MEH-PPV can be attributed to differences in the extinction coefficients. The peak molar extinction coefficients for PFPV, PFBT and MEH-PPV molecules in THF were determined by absorption measurements to be 5.7×10^{7} $M^{-1}cm^{-1}$, 4.6×10^{5} $M^{-1}cm^{-1}$, and 1.5×10^{7} $M^{-1}cm^{-1}$, respectively. Although all the three quenchers show good spectral overlap between their absorptions and the PDHF fluorescence, the large extinction coefficients of PFPV and MEH-PPV lead to their higher quenching efficiency as compared to PFBT molecules. According to the predictions of the energy transfer model, for quenchers with a relatively low quenching efficiency (q < 0.5) the ratio F_0/F depends approximately linearly on the quencher fraction over a wide range, while for highly efficient quenchers, the ratio F_0/F does not have a linear dependence on the quencher fraction. This agrees with our experimental observation that PFBT, the least efficient quencher due to its low molecular absorptivity, closely follows the linear Stern-Volmer relation, while the larger, highly efficient PFPV and MEH-PPV quenchers exhibit substantial deviations from linear Stern-Volmer behavior. Based on the success of

the nanoparticle energy transfer model in providing quantitative agreement with the spectroscopic results and the simple, intuitive picture it provides for describing the effect of highly efficient quenchers and the statistical variability in the number of quenchers per nanoparticle on the overall energy transfer efficiency, we believe this model will be useful for related systems such as superquenching-based sensors.[34, 35, 105, 122-124]

Both the Stern-Volmer analysis and analysis using the energy transfer model indicate that a single quencher molecule can effectively quench the fluorescence of hundreds of host molecules. In terms of a quenching volume or radius, this yields a result similar to those observed for doped fluorescent molecular crystals [125, 126] and quenching by charge carriers in MEH-PPV films.[72] If the quenching were described by one-step Förster energy transfer, the number of PDHF molecules that can be quenched by a single PFBT molecule would be determined by the Förster radius, which is in the range of 5-10 nm, not sufficient to account for the large quenching volumes observed. Because of the substantial spectral overlap between the absorption and emission of the PDHF donor, there is also the possibility of multiple energy transfer between molecules of PDHF, a process characterized by an energy diffusion length, which has been observed to be typically on the order of 5-15 nm for conjugated polymers.[127] Thus we conclude that the large quenching efficiency is likely due to a combination of energy diffusion and host-guest energy transfer that can effectively result in the quenching of hundreds of host polymers by a single quencher. Based on these considerations and the experimental evidence of relatively long-range energy transfer, it appears possible to construct probes

based on energy transfer quenching using ~10-20 nm diameter conjugated polymer nanoparticles.[40]

We previously observed that the conjugated polymer nanoparticles suffered from a reduction in fluorescence quantum yield as compared with the polymers in organic solvent.[46] Similar reductions in fluorescence quantum yield are typically observed for thin films of conjugated polymer (as compared to solution) and are attributed to interactions between polymer chain segments which can result in the formation of red-shifted, weakly fluorescent aggregate species. A fluorescence quantum yield of 10% was determined for pure PFPV nanoparticles, as described in our previous report.[46] However, for the case of blended nanoparticles, the polymer acceptors are uniformly distributed, with no discernable aggregate features in the fluorescence spectrum. If energy transfer to aggregate species is the primary loss mechanism, then one might expect that a higher quantum yield could be achieved in the PDHF/PFPV blend nanoparticles as compared to pure PFPV nanoparticles. Furthermore, nearly all of the excitation energy absorbed by hundreds of PDHF molecules is transferred to the PFPV, resulting in a large increase in absorptivity and therefore large improvements in fluorescence brightness as compared to smaller particles consisting of single polymer molecules. A fluorescence quantum yield of 14% and absorption cross-section of 1.9×10^{-12} cm^2 (assuming 200 molecules per nanoparticle) was determined for PDHF nanoparticles doped with PFPV (6 wt%) suspended in water, using a solution of Coumarin 1 in ethanol as a standard.[128] The calculated fluorescence brightness of PDHF/PFPV blend nanoparticles is more than 2000 times higher than that of rhodamine 6G. For comparison, the fluorescence brightness of

quantum dots has been reported to be in the range of 20 times that of rhodamine dyes,[129] and dye-loaded silica particles of ~30 nm in diameter have a reported brightness equivalent to approximately 100 rhodamine molecules.[78] The high brightness of the conjugated polymer blend nanoparticles compares favorably with quantum dots and dye-loaded silica colloids. We previously demonstrated that encapsulating small conjugated polymer nanoparticles with silica can improve photostability.[46] The high brightness, combined with the improved photostability, is very promising for biological labeling and sensing applications.

CHAPTER 7 ENERGY TRANSFER IN FLUORESCENT DYE DOPED CONJUGATED POLYMER DOTS

Energy transfer has been exploited in the design of fluorescent dyes and polymers,[130, 131] and has also been used to improve the functionalities of dye loaded latex or silica colloids. Some commercially available beads incorporate a series of two or more dyes which undergo excited energy transfer and exhibit a highly red-shifted emission spectrum. Triple-dye-doped silica nanoparticles have been demonstrated in which FRET-mediated emission features could be tuned by varying the doping ratio of the three tandem dyes.[132] Many conjugated polymers have high fluorescence quantum yields and broad emission spectra with full widths at half maximum (FWHM) of 50-100 nm, meeting the requirements for an efficient, versatile donor. Conjugated polymers also possess extraordinary "light harvesting" ability due to their large extinction coefficients and also exhibit very fast intra- and inter-chain photoexcitation transport. These characteristics offer possible advantages for the development of novel fluorescent nanoparticles.

In this chapter, we study the fluorescence and energy transfer photophysics of PDHF nanoparticles doped with a variety of fluorescent dyes. The dye-doped CPdots exhibit improved brightness, highly red-shifted emission spectra, and excellent photostability. The high experimentally observed energy transfer efficiency is not adequately described by Förster energy transfer alone. A model was developed which

includes the combined effects of exciton diffusion, Förster transfer, and particle size in determining the energy transfer efficiency. Comparisons of experimental results to the results of simulations based on the model yielded an exciton diffusion length within the range of accepted literature values. The CPdots could serve as a model system for studying energy transfer in complex nanoscale systems consisting of densely-packed chromophores. The major results presented in this chapter have appeared previously in a published journal article.[59]

7.1 Fluorescent dye doped conjugated polymer dots

In the preparation of CPdots, the rapid mixing with water leads to a sudden decrease in solvent quality, resulting in the formation of a suspension of hydrophobic polymer nanoparticles. It is possible to introduce hydrophobic fluorescent dyes during nanoparticle formation. Here, a variety of fluorescent dyes were chosen as dopant species based on their fluorescent quantum yield and spectral overlap with the donor's emission. Figure 7.1a presents the chemical structures of the dyes employed in this study. The doping concentration and the possibility of dye leakage were investigated by the following procedure. A nanoparticle suspension in which the nanoparticles contain 9 wt% of coumarin 6 and 91% of PDHF were prepared as described in the previous section. The dye to polymer ratio in the nanoparticles was determined by UV-Vis absorption spectroscopy, indicating that the dye to polymer ratio of the nanoparticle precursor mixture is preserved in the resulting nanoparticle suspension (i.e., neither species was preferentially precipitated or segregated during the preparation procedure). The overall preparation yield of the dye doped nanoparticles was typically higher than 80%. In order

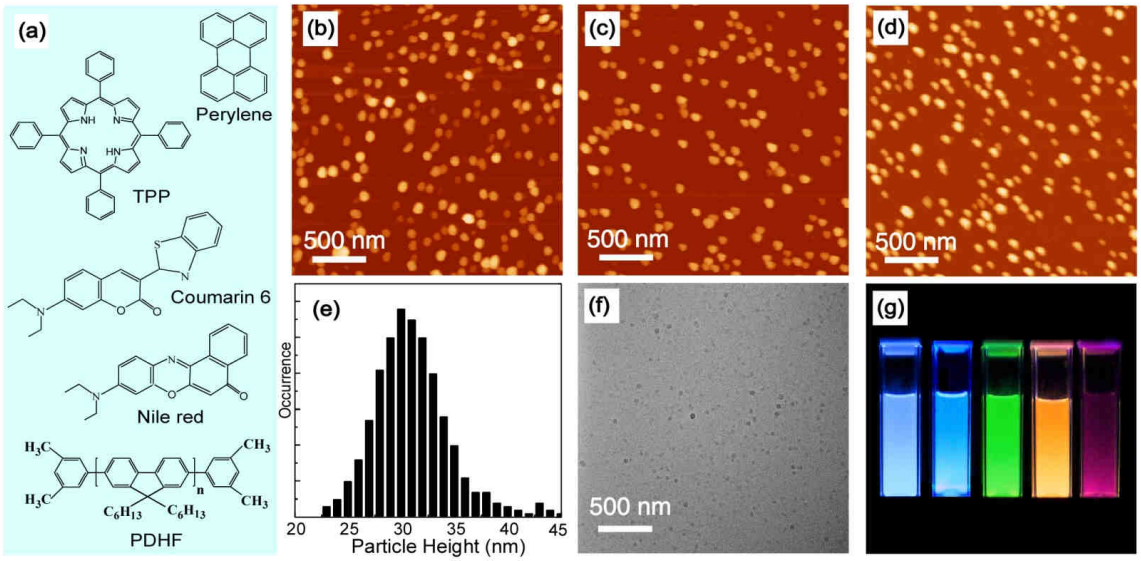

Figure 7.1 Nanoparticle size and morphology of fluorescent dye doped conjugated polymer dots. (a) Chemical structures of the fluorescent dye dopants and the host conjugated polymer PDHF. Representative AFM images of pure (b), perylene-doped (c), and coumarin 6-doped (d) PDHF nanoparticles dispersed on silica substrate. (e) Histogram of particle height data taken from AFM image (b). (f) TEM image of the pure PDHF nanoparticles. (g) Photograph of fluorescence emission from aqueous suspensions of the dye-doped PDHF nanoparticles taken under UV lamp excitation (365 nm).

to determine whether the dye was located primarily within the nanoparticles or as free dye molecules in solution, a series of tests were performed on the nanoparticle suspension as follows. The sample was concentrated by a factor of 6 using centrifugal concentrators (Pall Corp.) with a molecular weight cutoff of 30,000. A negligible absorption and very weak fluorescence from coumarin 6 were observed in the filtrate, which indicates that nearly all of the dye was embedded within the nanoparticles, with only a negligible fraction present as free dye in solution. The concentrated sample was diluted and the above procedure was repeated a few weeks later. The results indicate no observable dye leakage. The nanoparticle dispersions were drop-cast onto silica substrates for analysis of particle size and morphology by AC mode AFM. A representative AFM image of undoped PDHF nanoparticles is shown in Figure 7.1b. A particle height analysis obtained from the AFM image indicates that most particles possess diameters in the range of 30±5 nm (Figure 7.1e). The lateral dimensions from the AFM image are somewhat larger than the height due to the radius of curvature of the AFM tip.[133] The size and morphology were also characterized by TEM (Figure 7.1f), which indicated well-dispersed, spherical nanoparticles with diameters of ~30 nm. Our observations are consistent with the recent report that the equilibrium shape for small sized PDHF nanoparticles (~30 nm) tends to be spherical because polymer-water interfacial tension is the dominant factor which typically determines the polymer morphology in this size range, even for somewhat rigid polymers such as PDHF.[108] There are an estimated 100-300 polymer molecules per nanoparticle, assuming a densely packed spherical morphology. As shown in Figure 7.1c and 7.1d, the perylene-doped and coumarin 6-doped PDHF nanoparticles were

characterized by AFM. Height analysis indicates that the presence of dopant has no apparent effect on particle size and morphology.

7.2 Energy transfer from conjugated polymer to dye acceptors

As a promising class of conjugated polymers for organic light-emitting devices, many polyfluorene derivatives exhibit blue emission with high fluorescence quantum yield.[36, 116] In this study, PDHF was chosen as the host polymer in view of its high absorptivity in the near ultraviolet region and broad emission spectrum which provides favorable spectral overlap with a number of different dopant species. Figure 7.2 presents the normalized fluorescence emission spectrum of the PDHF nanoparticles in water and absorption spectra of perylene, coumarin 6, nile red, and TPP in THF solutions. The fluorescence of the host polymer PDHF in 400-550 nm range possesses good overlap with the absorption spectra of the fluorescent dye molecules, as required for efficient energy transfer via the Förster mechanism. Figure 7.1g shows the strong fluorescence emission from aqueous suspensions of undoped and various doped PDHF nanoparticles under UV excitation (365 nm). At a few percent doping fraction, the fluorescence from PDHF is almost completely quenched and the nanoparticles present strong fluorescence from the dopant species, indicating efficient energy transfer from the host polymer to dopant molecules.

Figure 7.3 shows the normalized absorption (dashed curves), fluorescence excitation and emission spectra (solid curves) of the undoped PDHF and four dye-doped nanoparticles containing varying concentrations of perylene, coumarin 6, nile red, and TPP. The dominant absorption peaks (around 375 nm) of the dye-doped nanoparticles are

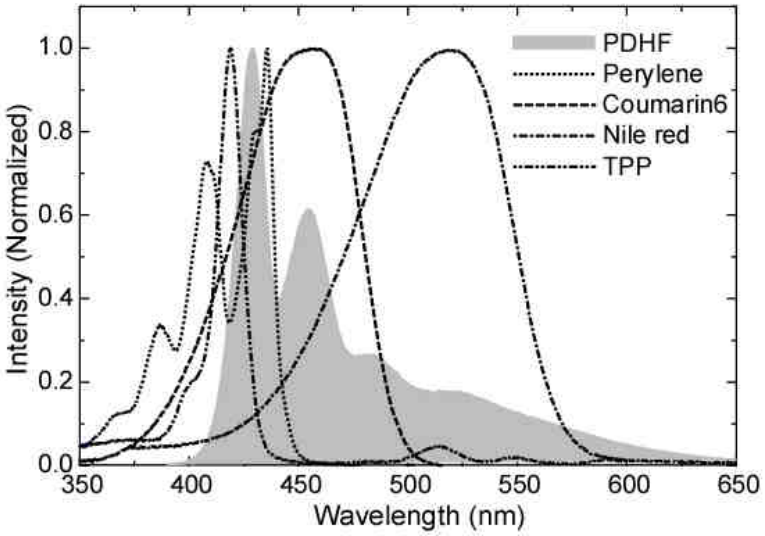

Figure 7.2 Normalized fluorescence emission spectrum of PDHF nanoparticles and absorption spectra of the fluorescent dyes.

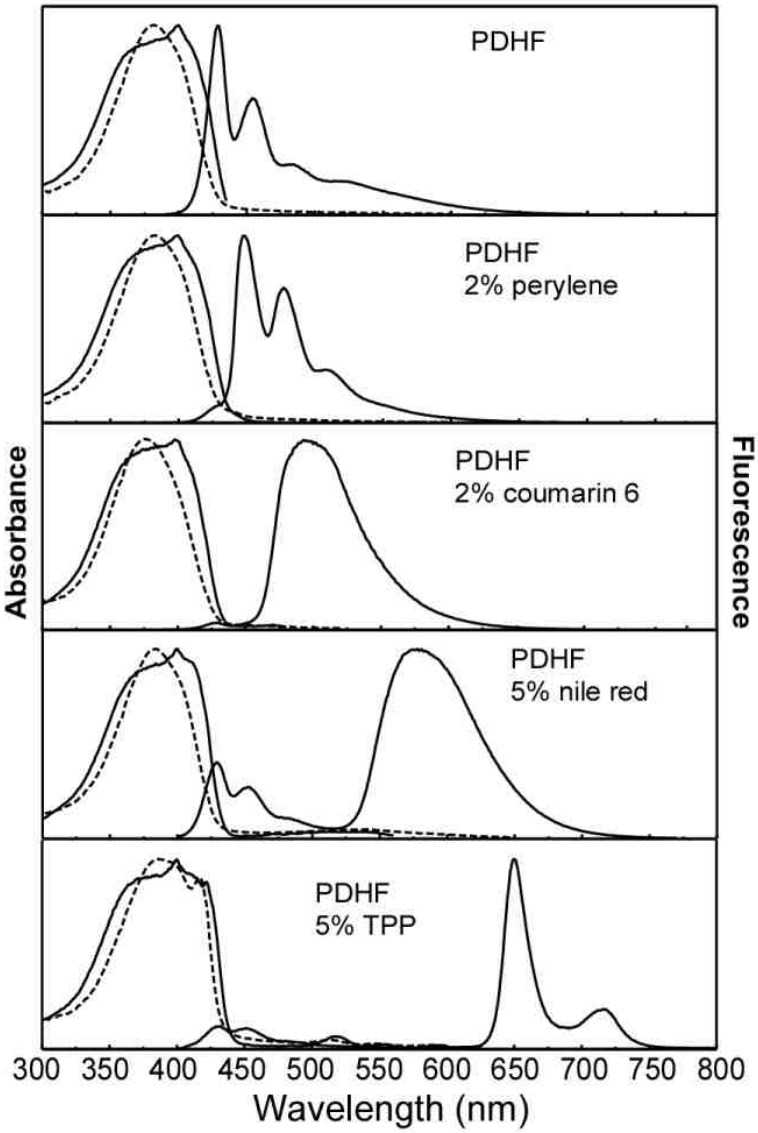

Figure 7.3 Normalized absorption (dashed), fluorescence excitation and emission spectra (solid) of pure and dye-doped PDHF nanoparticles.

due to PDHF, while relatively weak absorption from the dopant molecule can also be observed. With 375 nm excitation, where >95% of the absorption is due to PDHF, the fluorescence from PDHF is almost completely quenched, and the nanoparticles exhibit fluorescence emission spectra characteristic of the dopant species. Fluorescence excitation spectra obtained while monitoring dopant emission are very similar to the normalized absorbance spectra of PDHF, with minor differences attributable to the spectrum of the Xe lamp of the fluorometer. These observations indicate efficient intra-particle energy transfer from the PDHF host to the dopant fluorescent dyes. The observed energy transfer efficiencies are roughly similar to the energy transfer efficiencies observed for dye-doped polyfluorene thin films,[134-136] supporting the conclusion that the nanoparticles consist of polymers essentially in the solid state with dye molecules randomly distributed throughout the polymer.

Highly efficient energy transfer is evident in the evolution of the fluorescence spectra with increasing dopant concentration. Figure 7.4 shows the fluorescence emission spectra of the three types of dye-doped nanoparticles as dopant concentration is increased. For the case of PDHF nanoparticles doped with coumarin 6, the fluorescence from the PDHF host decreases with increasing dye content, while fluorescence from the dye increases and reaches a maximum around 1.0 wt%, after which a further increase in dopant concentration causes a pronounced reduction in fluorescence intensity. Over the concentration range of 0.2-1wt%, the nanoparticles present an intense green emission (~500 nm) from coumarin 6, which is clearly more intense than the 430 nm emission of undoped PDHF nanoparticles. It is also clearly observed that the green emission from

coumarin 6 consists of two emission peaks around 500 nm. Very similar spectral features were observed in coumarin 6-doped polyfluorene and PVK thin films.[137] As the doping concentration is increased from 2 to 5 wt%, the intensity of the dye emission starts to drop and the spectra change shape, consistent with the formation of dye aggregates with low fluorescence quantum yield. The perylene-doped system shows a similar trend in the evolution of the fluorescence as the fraction of dye is increased, but no additional spectral features from the perylene due to aggregation were observed, nor was quenching due to aggregates observed. The TPP-doped particles have a lower overall fluorescence quantum yield as compared to the other doped particles, consistent with the lower quantum yield of TPP as compared to coumarin 6 and perylene. While we have successfully demonstrated the doping strategy for a few fluorescent dyes, it should be noted that acceptor emission was not observed for some other dyes. For the nile red-doped case, nanoparticles prepared with 5 wt% doping exhibit moderate fluorescence from the PDHF host, as indicated in Figure 7.3. The donor's fluorescence is not completely quenched even in more heavily doped samples (10 wt%). Another dye, DCM, was observed to quench the host fluorescence, but no obvious fluorescence from the dye was observed. This is somewhat contradictory to other reports on DCM-doped nanoparticles and thin films.[138-140] However, the results support the tentative conclusion that the rigid, nonpolar polymer matrix would inhibit formation of the twisted intramolecular charge transfer state considered to be the dominant fluorescence pathway for DCM.[141]

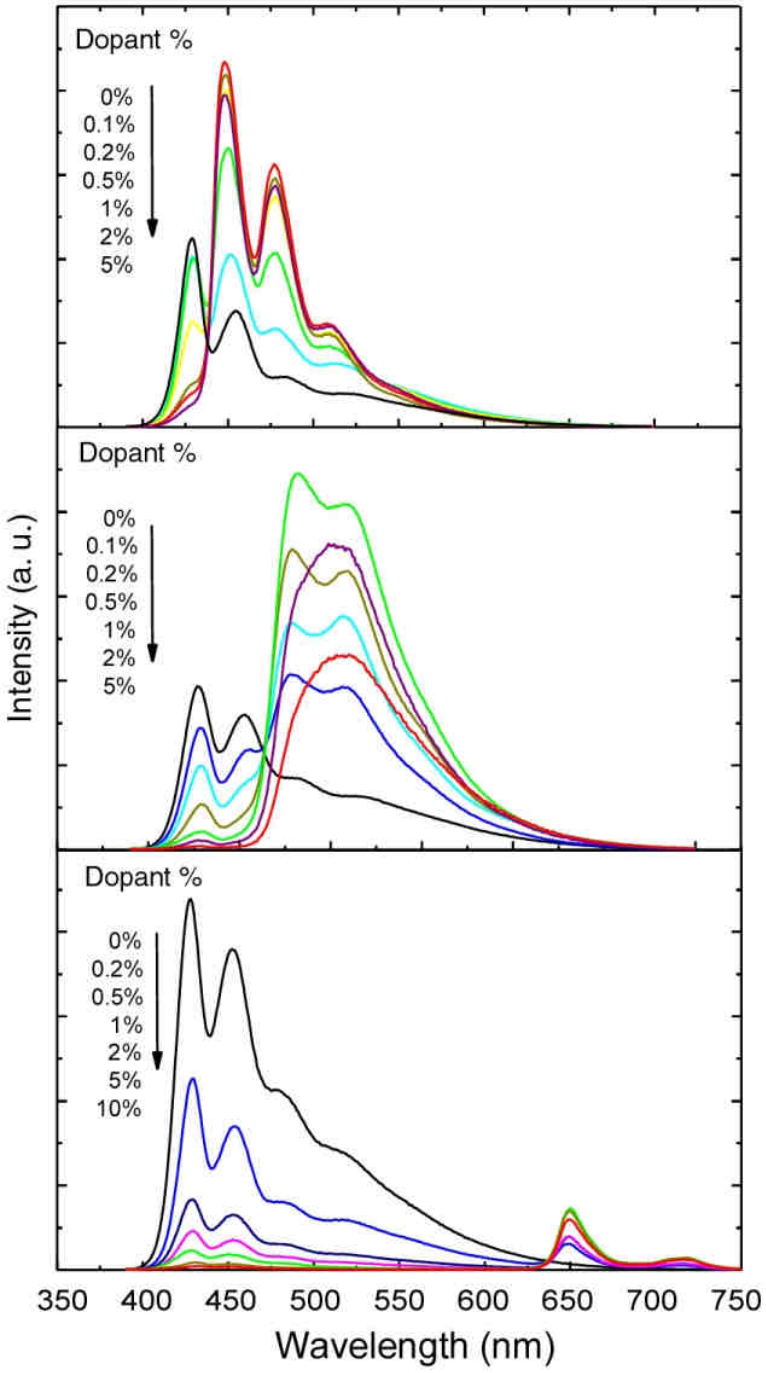

Figure 7.4 Concentration dependent fluorescence spectra of PDHF nanoparticles doped with perylene (top), coumarin 6 (middle), and TPP (bottom).

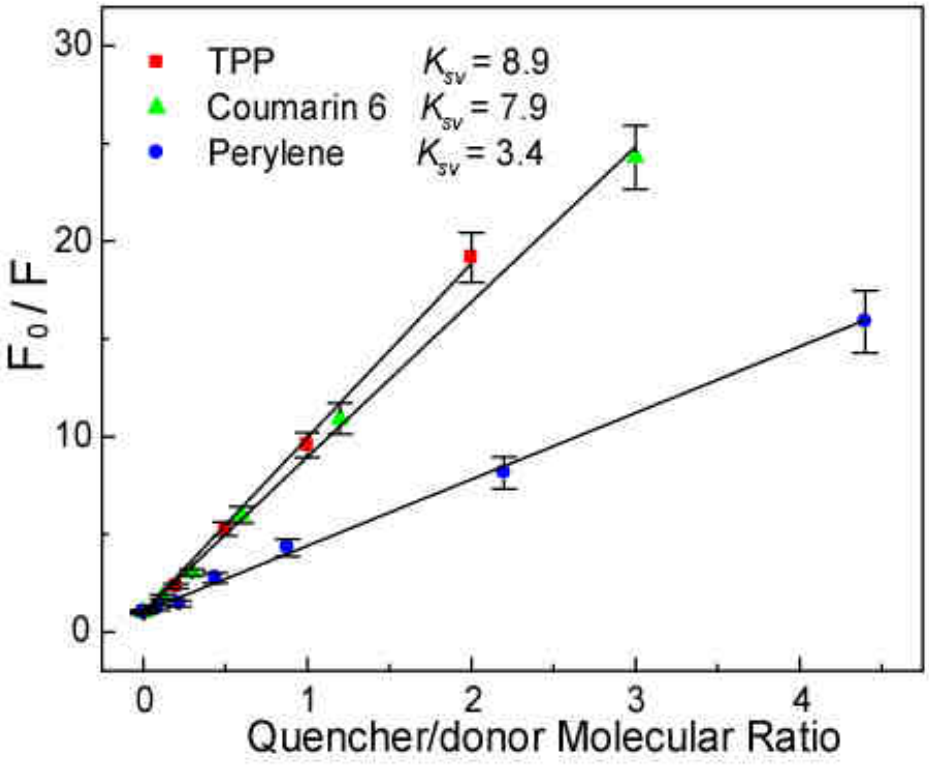

Figure 7.5 Fluorescence quenching of the donor versus molar fraction of quenchers in the dye doped PDHF nanoparticles. The scattered points are experimental results of PDHF fluorescence quenched by the three dye acceptors, while the solid lines represent fits to the Stern-Volmer equation.

The dependence of the PDHF fluorescence intensity on the dye concentration was modeled using the Stern-Volmer relation, which can be expressed as, [118]

$$F_0 / F = 1 + K_{SV}[A], \tag{7.1}$$

where F_0 and F are fluorescence intensities in the absence and presence of acceptor, respectively, K_{SV} is the Stern-Volmer quenching constant, and [A] is the concentration of the acceptor. The quenching constant is obtained from the slope of a linear fit to a plot of F_0 / F versus [A]. If the acceptor concentration is expressed as a molecule fraction, then K_{SV} represents the number of host molecules quenched by a single acceptor. The integrated emission intensities (F_0 and F) of the donor were obtained by decomposing the spectra in Figure 7.4 through a multi-peak Gaussian fitting. The Stern-Volmer analysis (Figure 7.5) indicated that approximately 3, 8, and 9 polymer molecules can be quenched by single molecules of perylene, coumarin 6, and TPP, respectively. The differences in the quenching efficiency per molecule can be attributed to the differences in the Förster radii of the three dyes. The perhaps surprising observation that a single dye molecule can quench one or more polyfluorene chains consisting of tens to hundreds of chromophore units is supported by a number of recent experimental reports which indicate that energy diffusion via rapid intrachain energy transfer is an important factor in determining energy transfer efficiency to acceptor dyes.[130, 142]. In the following sections, we attempt to quantify the relative importance of energy diffusion and Förster transfer by comparing experimental results to the results of simulations which include both energy diffusion and Förster transfer phenomena within the framework of a random walk.

7.3 Förster energy transfer model

Förster radius R_0 is defined as a distance at which the energy transfer rate k_{ET} is equal to the total decay rate ($k_{ET}=\tau_D^{-1}=k_R+k_{NR}$) of the donor in absence of the acceptor. Förster radii for the three dyes using PDHF as the donor were calculated using Equation 2.6. Since the PDHF refractive index is strongly dependent on wavelength over its emission range, the wavelength-dependent refractive index was adopted for the calculation.[136, 143] The spectral overlap between PDHF emission and dye absorption is presented in Figure 7.2. A fluorescence quantum yield of 20% was obtained for the PDHF nanoparticles using a solution of Coumarin 1 in ethanol as a standard.[128] The calculated Förster radii are 2.29 nm, 3.05 nm and 3.14 nm, for PDHF doped with perylene, coumarin 6, and TPP, respectively. The larger Förster radius of TPP is reflected by its large peak absorption coefficient (4.1×10^5 $M^{-1}cm^{-1}$) as compared to Coumarin 6 (5.4×10^4 $M^{-1}cm^{-1}$) and perylene (3.8×10^4 $M^{-1}cm^{-1}$). Coumarin 6 has a moderate molar absorption coefficient, but very good spectral overlap, therefore its Förster radius is comparable to that of TPP. As is clear from a comparison to the Stern-Volmer analysis, acceptors with larger Förster radii exhibit higher quenching efficiencies.

There have been a number of recent studies of energy transfer processes in dye doped polyfluorene thin films.[134-136, 144] The results were interpreted based on a model which assumes that dye molecules are arranged on a perfect cubic lattice within the polymer host. The lattice model is not appropriate for the nanoparticle systems currently under study because the quenching efficiency of the acceptors close to the surface is likely to be different from those close to the center of the particle. Furthermore, the dye

molecules are likely to be more or less randomly distributed in the polymer host, which leads to a number of dye molecules with overlapping Förster radii, particularly at higher dye to polymer ratios. In order to address these issues, we have developed a method for estimating energy transfer efficiency that takes into account the random distribution of the donor and acceptor positions within the confined space of a nanoparticle. The model is described as follows. Assuming that the overall energy transfer rate constant (k'_{ET}) scales linearly with the number of quenchers, the k'_{ET} from a randomly positioned exciton to all the quenchers can be expressed as

$$k'_{ET} = \sum_{j}^{N_A} k_{ET,j} = \sum_{j}^{N_A} \frac{1}{\tau_D} \left(\frac{R_0}{R_j} \right)^6 , \tag{7.2}$$

where N_A is the number of dye molecules per particle, R_j represents the distance between the exciton and the j^{th} dye molecule. Defining quenching efficiency q for a given exciton as $q = k'_{ET} / \left(k_R + k_{NR} + k'_{ET} \right)$, the overall quenching efficiency Q can be calculated by averaging over a large number N_D of randomly generated exciton positions:

$$\frac{F_0 - F}{F_0} = Q = \frac{1}{N_D} \sum_{i}^{N_D} \frac{k'_{ET,i}}{1 + k'_{ET,i}} . \tag{7.3}$$

Due to the sensitivity of the simulation results on the positions of the acceptors, the simulation results must be averaged over many randomly generated sets of acceptor positions as well. It should be noted that this simulation describes only the Förster energy transfer without considering exciton diffusion. The results of the simulations (using Förster radii calculated from the spectral overlap) and comparisons to experimentally determined quenching efficiencies are shown in Figure 7.6. It should be noted that we

elected to use experimental measurements of donor emission quenching as a measure of energy transfer efficiency instead of using acceptor emission, because the latter is not a reliable indicator of energy transfer efficiency due to possible quenching by aggregate species. The scattered data show the experimental results for the three dyes calculated from Figure 7.4, while the dotted curves represent the simulation results using the Förster transfer model. Large discrepancies between the experimental and simulated quenching efficiencies (as high as 50%) were observed for all the three dye species, which indicates that Förster transfer alone is not able to adequately account for the observed quenching behavior in these dye-doped nanoparticles and that other processes are likely to be involved, such as energy diffusion. Excitons in conjugated polymers can migrate along the polymer chain and may hop between chains, processes characterized by an exciton diffusion length, typically on the order of 5-20 nm for conjugated polymers.[127, 144, 145] Simulations of energy transfer which neglect energy diffusion are expected to underestimate the efficiency of energy transfer for such π-conjugated systems, as observed here.

7.4 Combined exciton diffusion and Förster transfer model

Energy transfer from a conjugated polymer to fluorescent dyes is described as occurring in two steps:[135, 136, 142, 144] (1) energy diffusion within the polymer host, and (2) energy transfer from the host to the guest dye molecules. Based on the above picture, we introduce a model which explicitly takes into account the combined effects of exciton diffusion, energy transfer, and particle size. The model is based on a 3D random walk on a discrete cubic lattice. Random walk-based methods have been previously employed to

model exciton diffusion and trapping in molecular crystals.[146, 147] However, the present model differs significantly from these previous models in that the possibility of Förster energy transfer to an acceptor dye is taken into account for each step in the random walk trajectory. The model and simulation methods are described as follows: The exciton is given an initial random position within the nanoparticle. After a time interval of duration Δt the exciton moves a single step of length ε in a random direction, subject to the constraints imposed by the geometry of the particle. Neglecting (for the moment) energy transfer to the dye acceptors, the average number of steps N required for the exciton to travel a distance equal to the exciton diffusion length L_D is given by $N=(L_D/\varepsilon)^2$. The time step size Δt is related to the fluorescence lifetime of the donor (τ_D) by $N\Delta t=\tau_D$. A given number of acceptor dye molecules are randomly distributed within a nanoparticle. At each step the overall energy transfer rate constant k'_{ET} is calculated based on the position of the exciton and the positions of the acceptors according to Equation. 7.2. The probabilities of energy transfer and decay during the time step are calculated as $p = 1 - \exp(-k'_{ET}\Delta t)$ and $p = 1 - \exp(-\Delta t / \tau_D)$, respectively. Comparison of generated random numbers against the probabilities of the two processes is used to determine if the exciton has undergone decay or transfer during the time step, ending the trajectory. If not, the exciton trajectory continues to the next step. Each trajectory is allowed to eventually terminate in either energy transfer or decay. The algorithm was verified by comparison of simulation results (obtained with energy transfer turned off) with the analytical expression for steady-state concentration as a function of distance for a decaying species

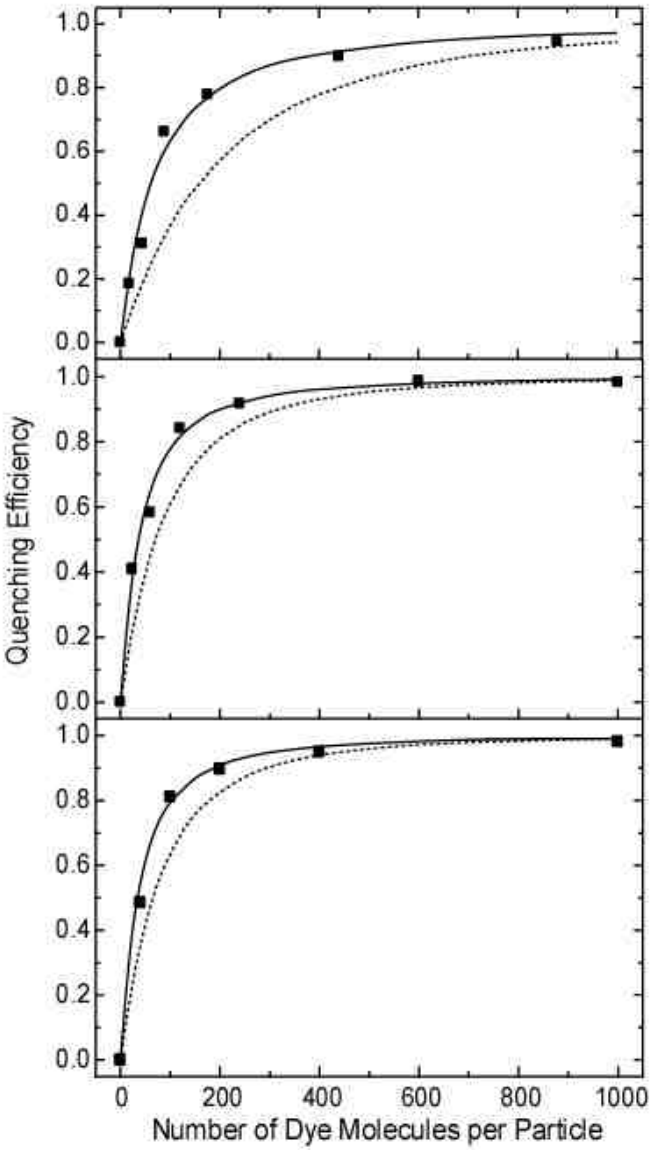

Figure 7.6 Quenching efficiency as a function of the number of dye molecules per particle for the PDHF nanoparticles doped with perylene (top), coumarin 6 (middle), and TPP (bottom). The squares are experimental results. The dotted curves represent the results of the Förster transfer model, while the solid curves represent the results of the combined exciton diffusion and Förster transfer model.

(obeying first-order kinetics, as in radioactive decay) which is diffusing from a point source.[148] It should be noted that, for materials with an optical penetration depth similar to that of the particle radius, the initial distribution of excitons (prior to energy diffusion) would be more heavily weighted towards the surface. However, this is not of major concern in the present case, since the particle radius is a factor of 2-3 smaller than the optical penetration depth.

A comparison of the model results to the experimentally determined quenching efficiencies was performed as follows. The number of acceptor dyes per particle used in the simulations was varied over the range of 0-1000, consistent with the range of experimental data. The same Förster radii used in the previous section were employed for the combined energy diffusion and transfer model. The exciton diffusion length was treated as a fit parameter and evaluated over the range of 6-10 nm. The step length ε was set to a value of 0.1 nm. Values for ε between 0.05 and 0.5 nm were found to yield similar quenching efficiency results, indicating little sensitivity to this parameter provided that it is set to a value well below the Förster radius and the exciton diffusion length. Thousands of exciton trajectories were calculated, and the quenching efficiency was determined by counting the number of trajectories which terminate in energy transfer relative to the total number of trajectories. The efficiencies were also averaged over many random acceptor positions, since the energy transfer efficiency is sensitive to the random placement of acceptors. For a given average number of acceptors per nanoparticle, the actual number of acceptors per nanoparticle is likely to follow a Poisson distribution. However, Poisson statistics were neglected since it was previously determined that it

does not affect the average quenching efficiency for cases where the quenching efficiency per acceptor is below 30 percent (see Chapter 6). A comparison of the calculated energy transfer efficiencies for a range of diffusion length values to the experimental results (Figure 7.6) yields an estimated exciton diffusion length parameter of 8 ± 1 nm for all three dyes. The agreement between theory and experiment is quite good over a large range of dye concentrations. An exciton diffusion length of 8 nm is consistent with reported values for similar materials, which range from 4 to 20 nm.[144, 149, 150] The excellent agreement between the model and experimental results, as compared to the model results obtained without energy diffusion, provides a strong indication of the importance of energy diffusion in this system. An additional issue that should be considered is whether the model assumption that the dyes are positioned randomly is physically reasonable. Entropic considerations and the particle formation kinetics associated with rapid mixing would tend to favor the assumption that dye positions are essentially random. However, depending on the particular dye species, surface free energy could be minimized by segregation of the dye on the surface. Since segregation of the dyes on the surface cannot be ruled out, it is appropriate to consider the effect of such segregation on the quenching efficiency of the dyes and the relative importance of energy diffusion and energy transfer. This issue can be addressed on a qualitative level as follows. If a dye molecule is located on the surface, this would reduce the effective quenching volume of the dye, since about half of the volume defined by the Förster radius of the dye would intersect with the particle. Indeed, simulations in which the dyes were confined to the surface resulted in substantially smaller quenching efficiencies (as

much as a factor of 2 smaller) as compared to the results obtained assuming a random dye distribution within the entire volume of the particle. Thus, a larger exciton diffusion length parameter would be required in order to obtain agreement between the model and the experimental results if this were the case. Based on these considerations, the exciton diffusion length obtained from the comparison between the model results and the experimental results should be taken as a lower estimate of the exciton diffusion length.

Additional simulations were conducted to explore the dependence of quenching efficiency on the exciton diffusion length. For 80 dye molecules per nanoparticle, the quenching efficiency was determined as a function of exciton diffusion length (Figure 7.7a). The points corresponding to $L_D = 0$ were calculated according to Equation 7.3, while the other points were obtained using the combined energy diffusion and Förster transfer model. As can be seen, the quenching efficiency increases monotonically with increasing the exciton diffusion length, approaching unity for L_D values well above the particle size (data not shown). A parameterized expression which takes into account both energy transfer and exciton diffusion was developed as follows. We define an effective energy transfer radius R_{ET} similar to the Förster radius, assuming that R_{ET} depends approximately linearly on the exciton diffusion length (L_D),

$$R_{ET} = R_0 + \alpha \cdot L_D, \tag{7.4}$$

where α is a parameter describing the relative contribution of exciton diffusion to the effective energy transfer radius. Replacing R_0 of conventional Förster theory with the effective energy transfer radius, the quenching efficiency can be written as

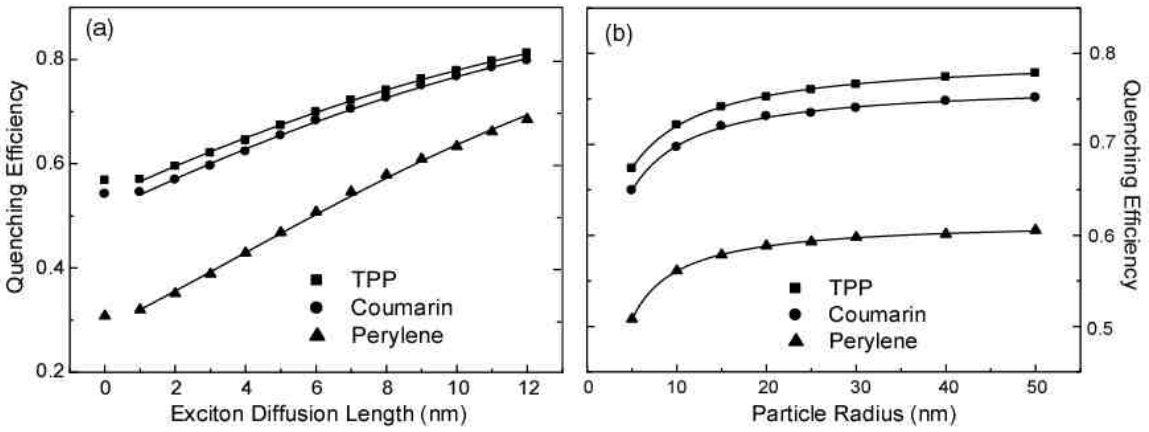

Figure 7.7 Dependence of quenching efficiency on exciton diffusion and particle size. (a) Dependence of the quenching efficiency on the exciton diffusion length for the three dye doped nanoparticles. The starting points in the absence of exciton diffusion were calculated according to Equation 4, while the other points were obtained by the combined energy diffusion and Förster transfer model. The curves are fits to Equation 6. (b) Size dependent quenching efficiency for the particles doped the three different dye species. The number of dye molecules per unit volume is fixed at a value of 0.0057 per nm^3, corresponding to 80 dye molecules in a particle with a radius of 15 nm. The scattered points are simulation results, and the curves merely serve as guides to the eye.

$$Q = \frac{(R_0 + \alpha \cdot L_D)^6}{\overline{R}^6 + (R_0 + \alpha \cdot L_D)^6} \tag{7.5}$$

where $\overline{R}$ represents an effective average distance from a donor to the nearest acceptor. Figure 7.7a shows the fitting curves to the results of by setting $\overline{R}$ and α as parameters. Fits to the combined energy diffusion and transfer simulations yielded excellent fits for all three dye species using parameters in the range of $\overline{R}$ =3.0±0.2 nm and α =0.064±0.001. It should be noticed that the effective energy transfer distance (including energy diffusion) is only 15-20 percent larger than R_0, when using L_D values of 8 nm. There is uncertainty of similar magnitude in typical R_0 values determined from spectral overlap. This indicates the necessity of careful determination of Förster radii as well as the need to obtain additional data for validation such as by systematically varying the acceptor concentration and employing a variety of acceptors.

In order to explore the dependence of quenching efficiency on nanoparticle size, simulations were performed using the combined energy diffusion and Förster transfer model (Figure 7.7b). For each particle size, number of dye molecules per unit volume is fixed at a value of 0.0057 per nm^3, corresponding to 80 dye molecules for a particle with a radius of 15 nm. As can be seen, the quenching efficiency increases monotonically for small particles in the radius range of 5-25 nm, approaching constant values for particle radii above 30 nm. The reason for this size dependence can be interpreted as follows: for smaller particles, the dopant molecules are more likely to be located close to the surface due to the higher surface to volume ratio. The dye molecules near the surface have a smaller effective quenching volume as compared to those farther from the surface (nearer

the particle center), leading to a lower quenching efficiency. As particle radius increases, the surface effect is relatively less significant, and therefore the quenching efficiency increases. For cases in which the particle radius is above 30 nm, well above the Förster radius, the quenching efficiency approaches a constant value corresponding to the bulk solid. The radii of the prepared dye-doped PDHF particles (~13-17 nm) is well below the estimated ~30 nm threshold for bulk quenching behavior, indicating that particle size is an important factor in this case. The apparent size dependence of the energy transfer properties of the nanoparticles points to the possibility of tuning energy transfer parameters using particle size or other nanoscale geometric parameters.

Time-resolved fluorescence measurements were performed to provide detailed information about energy transfer rate constants. Fluorescence decay kinetics traces were obtained using the TCSPC technique. Donor excited state lifetimes were extracted from the kinetics traces using custom software employing an iterative deconvolution method.[50] Statistical analysis of several fits and comparison of lifetime results obtained for Coumarin 6 in ethanol to literature values yields an estimated uncertainty in the reported lifetime of 50 ps or better. A fluorescence lifetime of 330 ps was obtained from the decay curves of the 420 emission of the undoped PDHF nanoparticles. This is consistent with reported lifetimes for similar polyfluorene derivatives which range from 160 to 400 ps in thin films.[135, 136] An increase in the decay rate of PDHF fluorescence is observed as the TPP concentration is increased. For the 0.2 wt% doped sample, the energy transfer rate constant (k'_{ET}) was deduced by subtracting the decay rate constant of undoped nanoparticles (τ_D^{-1} =3.0 ns^{-1}) from the total decay rate constant of the doped nanoparticles

(τ_D^{-1} =5.5 ns^{-1}). The result (k'_{ET} =2.5 ns^{-1}) is consistent the value calculated using the combined energy diffusion and Förster transfer model. The decay time (100 ps) from a more heavily doped sample (0.5 wt%) indicates a clear enhancement of energy transfer rate constant (k'_{ET} =7.0 ns^{-1}) due to the higher dopant concentration, and is also consistent with the results of the simulations. It should be noted that the experimental time resolution was insufficient to observe the complex dynamics that are often observed in systems involving energy transfer to randomly distributed acceptors.[144, 151] Additional experiments with improved time resolution are planned in order to address this question.

7.5 Photobleaching behavior of the dye-doped nanoparticles

The photostability of fluorescent nanoparticles is of critical importance for many fluorescence sensing and imaging applications. The photostability of a fluorescent dye or nanoparticle can be characterized by photobleaching quantum yield (ϕ_B), which is equal to the number of molecules that has been photobleached divided by the total number of photons absorbed over a given time interval.[19] In other words, photobleaching quantum yield is the reciprocal of the number of excitation cycles that a typical molecule endures before it undergoes irreversible photobleaching, and can be expressed as

$$\phi_B = \frac{k_B}{k_R + k_{NR} + k_{ET} + k_B} \tag{7.6}$$

where k_B is the photobleaching rate constant usually related to photochemical reactions involving the excited state of the molecule. Conventional fluorescent dyes such as coumarins and rhodamines exhibit bleaching quantum yields in the range of 10^{-4}-10^{-6}.[19] For typical fluorescent dyes under low excitation intensity, the photobleaching kinetics

follows a single exponential decay curve. However, the photobleaching of conjugated polymers is more complicated, and the mechanism remains poorly understood due to the complex set of interactions involving a large number of species such as excitons, polarons, molecular oxygen, and partially oxidized species of unknown structure.[64] Polyfluorene-based thin films in air often exhibit spectral instability that involves the appearance of an undesired green emission arising from energy transfer to a small number of keto (fluorenone) defects resulting from partial oxidation of the polymer.[152] Similarly, partially oxidized PDHF nanoparticles exhibit green emission due to the presence of fluorenone sites on the polymer backbone.

Figure 7.8a shows the emission spectra of the 0.5% TPP-doped PDHF nanoparticles before and after 2 hours of photobleaching under 380 nm UV light. A comparison between the spectra exhibits clearly an increased green emission around 530 nm, while the emission intensities from the polyfluorene host (430 nm) and the TPP guest (650 nm) are reduced. The photobleaching kinetics data for doped and undoped PDHF nanoparticles are shown in Figure 7.8b. The photobleaching kinetics of the undoped PDHF particles can not be described by a single exponential decay. However, the sum of two exponential functions, with a fast component characterized by a time constant of 600 s (30%) and a slow component characterized by a time constant 3.0×10^4 s (70%), adequately reproduces the photobleaching curve. The observed biexponential photobleaching kinetics could indicate the presence of two or more distinct populations, possibly due to the presence of different phases with distinct morphology and photophysics. It has previously been observed that different phases of polyfluorene

derivatives can be prepared from the same polymer, each with markedly different fluorescence and electronic properties arising from differences in the nanostructure of the material.[116, 153] The observation of multiple decay rates is also consistent with the possibility that chains located near the surface of the particle could be more susceptible to photobleaching as compared to chains located deeper within the nanoparticle. Another possibility is that the combination of energetic disorder and intraparticle energy transfer results in energy transfer from higher energy excitations to states of lower energy. This results in a range of excited state lifetimes, which would give rise to multi-exponential photobleaching kinetics, according to Equation 7.6. It should be mentioned that additional investigations into the effect of energy transfer phenomena on phobleaching kinetics are currently underway. A procedure similar to that described by Eggeling and co-workers [19] was employed to obtain quantitative photobleaching quantum yields from the photobleaching kinetics data. In order to validate the procedure, analysis of photobleaching kinetics for Coumarin 6 was performed, yielding results similar to reported values.[19] The fast bleaching component corresponds to a photobleaching quantum yield of 1.0×10^{-6}, while the slow bleaching component corresponds to a photobleaching quantum yield of 2.6×10^{-8}. Since the fraction of emitted photons associated with the rapidly decaying component is very small, the determination of death number (ϕ_F/ϕ_B) is based on the fluorescence quantum yield (ϕ_F=0.20) and the slow photobleaching component ($\phi_B=2.6\times10^{-8}$), yielding a death number of 7.7×10^{6} photons per undoped PDHF nanoparticle.

We also determined the effect of energy transfer on photostability of the doped nanoparticles. TPP was chosen as the dopant due to its highly red-shifted fluorescence which provides clear separation between donor and acceptor fluorescence. Biexponential fits to the photobleaching kinetic traces of 0.2 wt% TPP-doped nanoparticles of doped particles yield time constants of 1391 s for the fast-bleaching component and 5.8×10^4 s for the slow component in the host photobleaching kinetics, both approximately a factor of two larger than the time constants obtained for undoped particles. Recalling the results from a previous section, the energy transfer efficiency is approximately 50% at the doping fraction of 0.2 wt% TPP. According to the rate picture, an energy transfer efficiency of 50% would reduce the photobleaching rate constant by a factor of two as compared to undoped nanoparticles, consistent with the observed photobleach kinetics. A higher dopant ratio (0.5 wt% TPP) leads to longer time constants for both the two components. Again, this is consistent with the rate picture (Equation 7.6). During the course of the photobleaching kinetics measurement, light also bleaches the dopant molecules (Figure 7.8b), which should result in partial recovery of donor fluorescence, though this phenomenon had no apparent effect on the photobleaching kinetics. The photobleaching kinetics of the acceptor emission at 650 nm emission of the 0.5%TPP-doped sample exhibits a biexponential decrease similar to that of the donor. Regarding the death number for doped nanoparticles, the calculation indicates the death number for the donor's fluorescence is roughly the same to that of the pure PDHF nanoparticles because the lower photobleaching rate is offset by the lower donor quantum yield. However, there is a net increase in total death number per particle when the emission

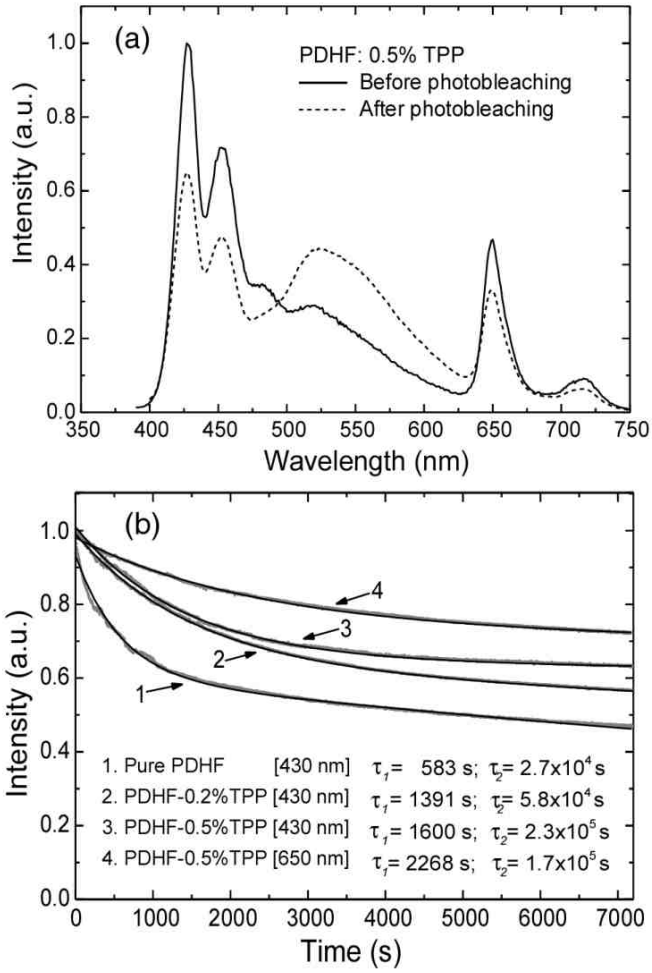

Figure 7.8 Photobleaching behavior of the dye-doped conjugated polymer dots. (a) Fluorescence emission spectra of TPP-doped PDHF (0.5%) before and after 2 hours of photobleaching. (b) Photobleaching kinetics of the pure and TPP-doped PDHF nanoparticles under continuous illumination with 1.0 mW of 380 nm UV light. The wavelengths in brackets indicate the emission collection wavelengths. The black curves result form the fitting by double exponential decay and the time constants are indicated in the Figure.

from the acceptors is included. In the 0.5%TPP-doped sample, the death number for the acceptor's fluorescence is calculated to be 3.2×10^{6} photons per nanoparticle according to the fluorescence quantum yield (ϕ_F = 0.013) and the photobleaching kinetic trace (ϕ_B=4.1×10^{-9}) of the acceptors. The death number of the nanoparticle (considering acceptor emission only) is similar to that of free TPP in solution multiplied by the number of dye molecules per nanoparticle (~100). Extrapolating to the case of heavily doped nanoparticles (negligible donor emission and short donor lifetime), the nanoparticle death number would be largely determined by the number of acceptor molecules per nanoparticle multiplied by the acceptor death number. Since dye loading fractions similar to those typically employed in dye-loaded silica or polystyrene nanospheres can be achieved with the dye-loaded PDHF particles, we tentatively conclude that similar photostability figures of merit could be achieved. Based on these results, we conclude that doping with energy acceptors is a viable strategy for improving photostability of conjugated polymer nanoparticles.

It has been observed that, in some cases, the photobleaching rate is proportional to the triplet state population of the fluorophores,[154] and that triplets can result in complex photobleaching kinetics.[155, 156] If the dopant species are able to act as triplet quencher, it would increase the photostability of the donor. Similarly, oxygen is potent triplet quencher and has been found to increase the fluorescence intensities of conjugated polymers.[157] In addition, singlet oxygen generated by interaction of O_2 with triplet states is also likely to be involved in the production of partially oxidized defect species. While TPP is known to be an efficient singlet oxygen generator, and singlet oxygen is known to

be involved in photobleaching, we observed no reduction in the photostability of TPP-doped particles as compared to undoped particles.

Finally, we consider the nanoparticle figures of merit for fluorescence labeling applications. We previously observed that the conjugated polymer nanoparticles suffered from a reduction in fluorescence quantum yield as compared with the polymers in organic solvent.[46] Blended conjugated polymer nanoparticles were developed later and found to have a slightly higher quantum yield.[106] The dye-doping strategy provides additional options for optimizing nanoparticle optical properties due to the wide range of readily available dyes with quantum yields approaching unity. Furthermore, PDHF as host has efficient light harvesting ability as compared to optically inert polymer or silica materials. Nearly all of the excitation energy absorbed by hundreds of PDHF molecules is transferred to the dye acceptors, which can exhibit a high fluorescence quantum yield. The combination of large per-particle absorptivity and high fluorescence quantum yield results in large improvements in fluorescence brightness. Fluorescence quantum yields of ~40% and a peak absorption cross section of 1.9×10^{-12} cm^2 (assuming 200 polymer molecules for a nanoparticle) were determined for PDHF nanoparticles doped with perylene or coumarin 6 (2 wt%) suspended in water, using a solution of Coumarin 1 in ethanol as a standard.[128] Another significant feature of the dye-doped nanoparticles is their highly red-shifted emission spectrum as compared to pure polymers and typical fluorescent dyes. Differently doped nanoparticles with a variety of emission wavelengths can be simultaneously excited using a single light source, a useful feature for imaging and multiplexed fluorescence detection. Photostability is also an important factor for

many applications. We observed that the dye molecules in the PDHF particles have photostability similar to that of free dyes in solution, as estimated from the photobleaching experiments. Since each particle contains hundreds of dyes, the death numbers and survival times of the dye-doped nanoparticles appear to be hundreds times better than single conventional molecular dyes and similar to dye-loaded polymer spheres of similar dimensions. Based on the extraordinary “light harvesting” capability of the polymer host and the high quantum yield of the dye molecules, the fluorescence brightness of the perylene- and coumarin-doped nanoparticles is estimated to be ~200 times larger than that of single quantum dots, and 40 times higher than that of dye-loaded silica spheres of similar dimensions. The combination of the high brightness, highly red-shifted emission spectrum, and excellent photostability is promising for biological labeling and sensing applications.

CHAPTER 8 POLYMER PHASE AND ENERGY TRANSFER IN POLYFLUORENE DOTS

As a promising class of blue-emitting conjugated polymers, polyfluorenes display complex structure-property relationships.[116] In particular, the dependence of photophysical properties on polymer morphology for poly(9,9-dioctylfluorene) (PFO) has garnered much attention.[158-161] In PFO, distinct phases have been identified: principally a disordered glassy phase and a crystalline β-phase containing planar polymer chains.[162, 163] The presence of β-phase in thin films can be influenced by thermal and vapor treatment of as-cast films or by varying the solvent from which the film is spin-cast.[158, 160, 164] Significantly, the fraction of β-phase in the films was found to affect the generation of polarons and triplet excitons[159, 161, 165] as well as the photoluminescence quantum efficiency.[153] These results indicate that control over conformation is important for optimizing performance.

In this chapter we study on the polymer phase and fluorescence properties of PFO nanoparticles. PFO nanoparticles prepared by the reprecipitation method were observed to exhibit the spectroscopic characteristics of the glassy polymer phase. Addition of organic solvent to the aqueous suspension resulted in the formation of β-phase, presumably by solvent-induced swelling which facilitates formation of the thermodynamically favored β-phase. The β-phase persists after the removal of the organic solvent. The fraction of the polymer in the β-phase was observed to depend on

the concentration of the organic solvent. The resulting mixed-phase PFO nanoparticles exhibit efficient energy transfer from the glassy phase to the β-phase, resulting in narrower, red-shifted fluorescence and increased quantum yield, as compared to the all glassy PFO nanoparticles. The mixed phase nanoparticles also exhibit reduced energy transfer to dye dopants incorporated in the nanoparticles, consistent with competitive energy transfer to polymer chains in the β-phase. The results indicate that the energy transfer and fluorescence properties of PFO nanoparticles can be tailored to a specific application by a combination of doping and control of polymer conformation. The major results presented in this chapter have appeared previously in a published journal article. [57]

8.1 Mixed polymer phase in polyfluorene dots

Poly(9,9-dialkylfluorene)s are known to exhibit complex morphology. For instance, they can form disordered glassy phase, a partially crystalline β-phase, or a liquid crystalline phase, depending on the side-chain structure and thermal treatment.[116] Figure 8.1a shows the chemical structure of the PFO polymer and the β-phase chain segment that can be described as a "planar zigzag" or 2_1 helix conformation.[158] The β-phase formation of PFO in solution can be observed in poor solvent by varying temperature,[166] or in solvent/non-solvent mixtures by increasing the non-solvent content.[116] Here we demonstrate the preparation of PFO nanoparticles with varying fractions of β-phase polymer, and examine the photophysical properties of the mixed phase nanoparticles. Rapid mixing of a dilute solution of PFO in THF (400 ppm, 200 μL) with water (8 mL) under sonication leads to the formation of PFO nanoparticles that exhibit the optical properties of the glassy phase. The THF was removed by partial

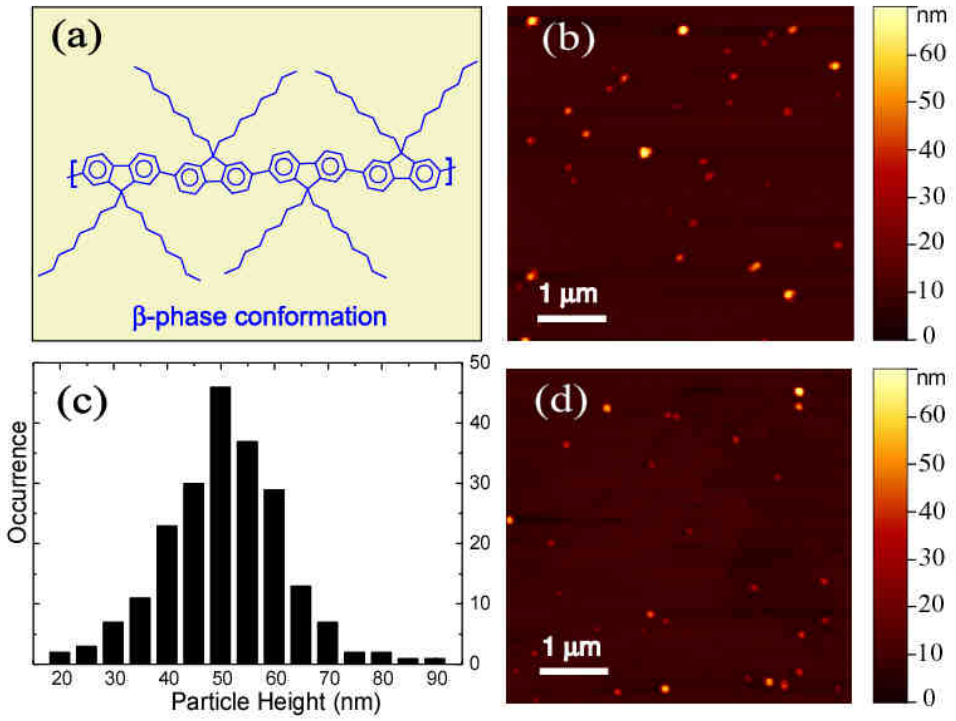

Figure 8.1 β-phase conformation and AFM images of PFO dots. (a) Chemical structure and the β-phase conformation of the conjugated polymer PFO. (b) A representative AFM image of glassy PFO nanoparticles dispersed on mica substrate. (c) Histogram of particle height data taken from AFM images of glassy PFO nanoparticles. (d) A representative AFM image of mixed phase PFO nanoparticles.

vacuum evaporation. The resulting nanoparticle suspensions are clear (non turbid), colorless, and stable for weeks, with no evidence of aggregation or decomposition. For AFM measurement, one drop of the nanoparticle dispersion was placed on a freshly cleaved mica substrate. As indicated in the AFM images of Figure 8.1b, the PFO nanoparticles exhibit an approximately spherical shape. The particle height histogram (Figure 8.1c) shows that most of the nanoparticles possess a particle size in the range of 30 nm to 60 nm, with a small fraction of particles over 70 nm. The mean particle size of ~50 nm corresponds to roughly 280 polymer molecules per nanoparticle, assuming dense packing of the polymer chains.

At low concentration in a good solvent, PFO adopts an elongated rod-like conformation containing predominantly only a single polymer chain.[167] Accordingly, PFO in dilute THF solution exhibits an unstructured absorption spectrum with maximum centered at ~390 nm (Figure 8.2a, solid curve). The fluorescence spectrum exhibits a well-resolved vibronic structure with the 0-0 transition centered at ~420 nm (Figure 8.2b, solid curve). During the nanoparticle preparation, the rapid mixing of a small volume of PFO in THF solution with water leads to a sudden decrease in solvent quality and the formation of nanoparticles due to aggregation of the polymer chains. As indicated in Figure 8.2a (dashed curve), the absorption spectrum of the as-prepared PFO nanoparticles is broadened and blue-shifted as compared to that of the polymer in THF solution. The blue-shifted absorption peak is consistent with an overall decrease in the conjugation length due to bending and kinking of the polymer backbone, and the red tail in the absorption spectrum is indicative of interchain interactions.[46] The as-prepared PFO

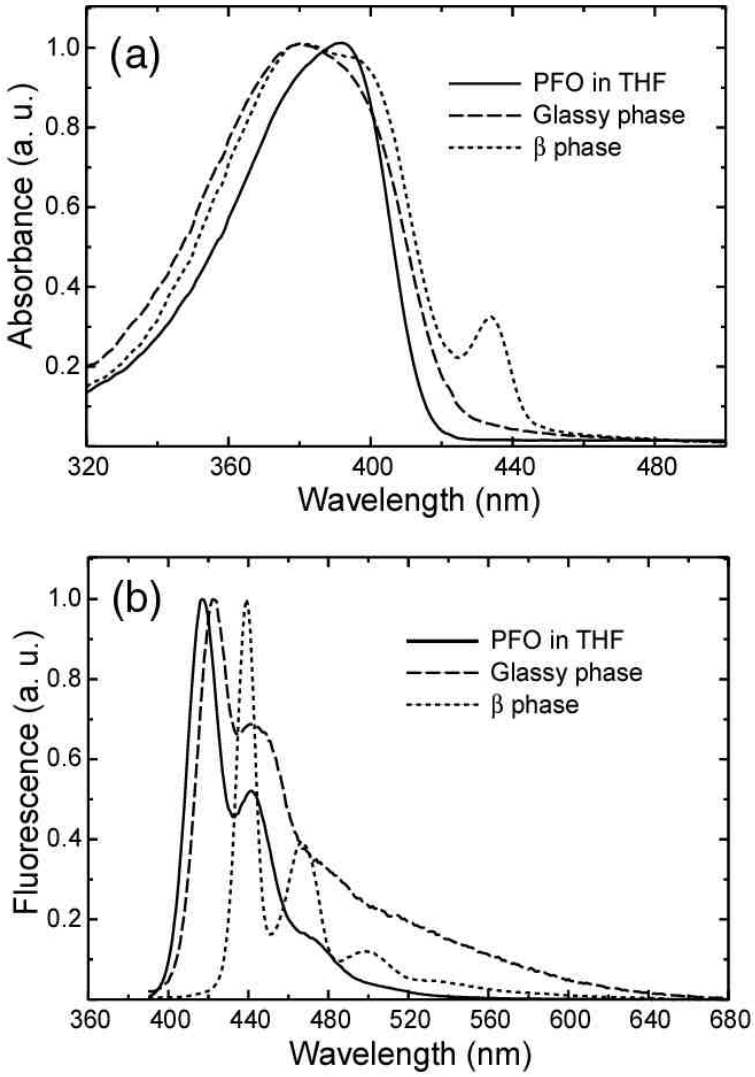

Figure 8.2 Normalized absorption spectra (a) and fluorescence emission spectra (b) of PFO in dilute THF solution (solid), glassy PFO nanoparticles (dashed) and mixed phase nanoparticles (dotted) obtained by toluene swelling.

nanoparticles exhibit a slightly red-shifted fluorescence and a long red tail as compared to the polymer in THF solution. Since the nanoparticles possess a densely packed structure, the red-shift and the long red tail in fluorescence could be ascribed to increased interchain interactions, resulting in a small fraction of red-shifted aggregate species. The resulting energetic disorder, combined with multiple energy transfer, would result in a net red-shift in the fluorescence spectrum as compared to that of the polymer in solution. Based on these observations and comparison to studies correlating optical spectra and x-ray diffraction results of thin films,[158, 160] we conclude that the as-prepared nanoparticles consist of polymer molecules in a dense, disordered "glassy" phase.

Addition of organic solvent to an aqueous suspension of hydrophobic polymer particles is known to induce swelling of the particles. The as-prepared (glassy) PFO nanoparticles exhibited clear changes in their spectroscopic properties upon exposure to either toluene or THF, and the changes persist after removal of the organic solvent. The observed shifts in the UV-Vis absorption and fluorescence spectra are consistent with the formation of a β-phase.[158] The spectroscopic properties of the β-phase PFO differ dramatically from those of the glassy phase – while the π-π^* absorption of the glassy phase is relatively broad and featureless, the β-phase exhibits a narrow, red-shifted, and well-resolved absorption peak at 435 nm, with clear vibronic features superimposed on the main absorption band (Figure 8.2a, dotted curve). The fluorescence of the β-phase also displays a narrow, red-shifted emission peak at 439 nm, and a well-resolved vibronic progression in the emission spectrum (Figure 8.2b, dotted curve). A clear photophysical picture has been derived from observing the spectral similarities between the β-phase of

PFO and the planarized ladder-type poly(para-phenylene) – the more extended π-conjugation in PFO β-phase accounts for the observed bathochromic shift and the sharp vibronic features observed in the spectra.[158] It should be noted that β-phase formation was observed in PFO, but not in poly(9,9-dihexylfluorene) (PDHF) nanoparticles subjected to the same swelling protocol, although previous studies have indicated certain features related to β-phase formation in PDHF films.[168] An alternative method for inducing the formation of β-phase is to anneal the glassy PFO nanoparticles at a temperature above the T_g of the polymer (~75°C [163]). However, thermally annealed PFO nanoparticles (90 °C, for 1 hour) exhibit only a small shoulder, rather than a well-resolved peak, at the red edge of the absorption spectrum (data not shown). A similar small shoulder is present in the absorption spectra of thermally annealed PFO films.[158]

8.2 Swelling controlled polymer phase in polyfluorene dots

We observed that addition of the water-miscible solvent THF can induce β-phase formation with reliable control of the relative fraction of β-phase. Aqueous dispersions of the glassy nanoparticles were mixed with varying amounts of THF to yield a THF/water ratio ranging from 0 to 40 percent by volume. The mixtures were left for 2 hours, and then the THF was removed by partial vacuum evaporation prior to AFM and spectroscopic measurements. It should be noted that, over the range of 0 to 40 percent THF, the swelling step was not observed to induce nanoparticle aggregation or Ostwald ripening. Figure 8.1d shows the AFM results for the PFO nanoparticles swelled with the highest THF/water ratio (40%), which indicate no obvious changes in particle size distribution as compared to the glassy nanoparticles prior to swelling (Figure 8.1b).

However, variation in the solvent/water ratio was observed to result in variations in the relative intensity of the spectroscopic features associated with the β-phase. Figure 8.3a shows the dependence of the absorption spectra of PFO nanoparticles on the THF fraction used in the swelling step. The β-phase absorption peak (435 nm) can be observed at the THF/water ratio of 5%, and the intensity increases upon further increase of the THF/water ratio. This change is also accompanied by a decrease in the 375 nm principal absorption feature, and the appearance of the vibronic structure superimposed on the main absorption. At the highest THF/water ratio (40%) employed in the swelling experiments, the β-phase fraction was estimated to be ~27% by comparing the intensity of β-phase 0-0 peak to the overall absorption from the planarized β-conformation.[160] We found that the THF swelling must be done as a separate step after the glassy nanoparticle formation in order to achieve reliable control of the β-phase fraction. Mixed phase PFO nanoparticles could be directly obtained by reducing the concentration of the polymer in THF (20 ppm) and increasing the amount of the polymer/THF solution (2 mL) relative to water (8 mL) in the reprecipitation – however, the particles prepared by this method exhibit smaller size (7-15 nm). Glassy phase particles were not obtained using this preparation method, likely due to the larger amount of THF employed and its tendency to swell the particles.

Each of the aqueous PFO nanoparticle dispersions was diluted to yield an absorbance of 0.1 at 375 nm, and fluorescence spectra were obtained using an excitation wavelength of 375 nm. As shown in Figure 8.3b, the fluorescence from the PFO glassy phase (~423 nm) decreases dramatically, and is eventually completely quenched as the

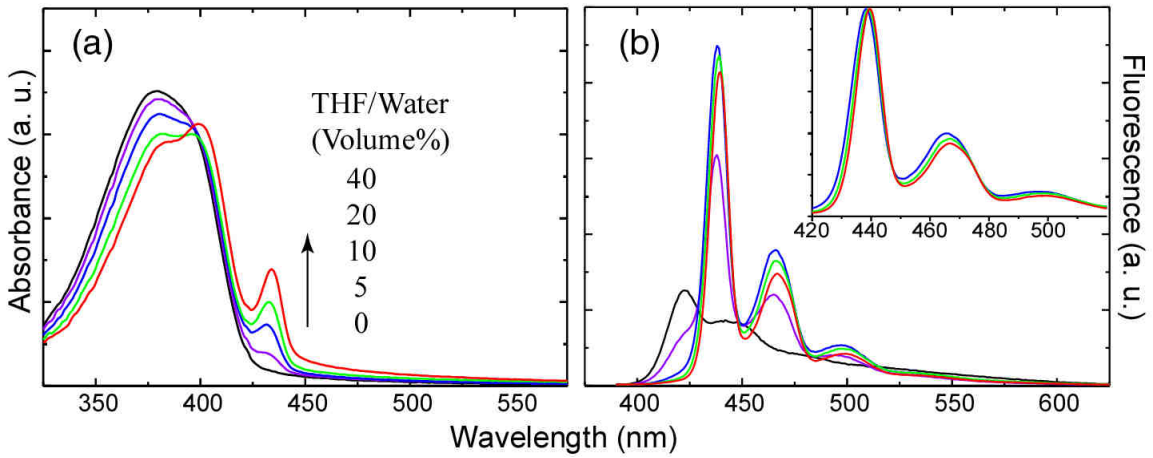

Figure 8.3 Absorption spectra (a) and fluorescence emission spectra (b) of PFO nanoparticles containing varying β-phase fractions. The absorption increase (435 nm) of the β-phase is indicated by an arrow, with increasing the THF/water ratio in the swelling. Each sample was diluted to yield an absorbance of 0.1 at 375 nm, and fluorescence spectra were obtained under the 375 nm excitation. The normalized emission spectra shown in the inset indicates a slight red-shift with increasing β-phase fractions.

THF/water ratio employed in the swelling increases. It should be noted that the observed changes in the fluorescence spectra are not likely due to residual THF, since little or no changes were observed in the spectra after additional vacuum evaporation steps to remove residual THF, indicating any remaining THF has little effect on the particle properties. The fluorescence from the β-conformation (~438 nm) increases and reaches a maximum for the PFO nanoparticles swelled at the THF/water ratio of 10%. Although further increase of the THF/water ratio increases the β-phase fraction (as determined from the absorbance), the nanoparticles exhibit a slight decrease in fluorescence intensity, together with a slight red-shift in the emission wavelength that is observed in the normalized emission spectra (Figure 8.3b inset). This may be due to increased interactions between chains of the β-conformation, or increases in the size of the β-phase domains resulting in an increase in conjugation length. It has previously been observed that increasing the conjugation length of conjugated polymers often results in both a red shift in the emission and a reduction in fluorescence quantum yield,[115] and inter-chain aggregates are known to exhibit weak, red-shifted emission in some cases.[52] Significantly, at some THF ratios the mixed phase particles exhibit an increased fluorescence quantum yield relative to the glassy phase. Fluorescence quantum yields of ~35% were determined for mixed phase nanoparticles (swelled at the THF/water ratio of 10%) and ~21% for the glassy phase nanoparticles, respectively (Coumarin 1 in ethanol was employed as a quantum yield standard). This is in sharp contrast to thin film results,[153] where the glassy phase and β-phase PFO were found to exhibit similar fluorescence quantum yields at room temperature. The spectroscopic characteristics of

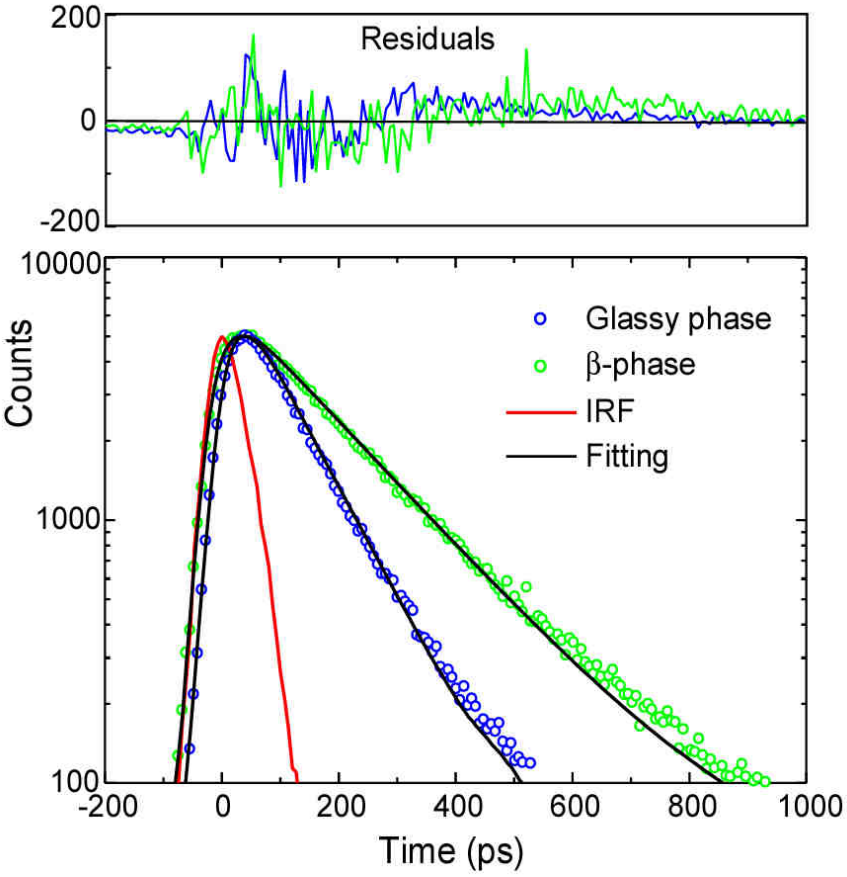

Figure 8.4 Semi-Log plot of fluorescence decays of the glassy and β-phase PFO nanoparticles measured by a TCSPC setup. The red curve shows the instrumental response function (IRF). The scattered symbols represent experimental data, and the solid lines are fitting curves obtained employing an iterative deconvolution method. Residuals are shown above the fits.

the mixed phase nanoparticles, primarily the increased fluorescence quantum yield, narrower emission peak and increased energy gap between excitation and emission as compared to the glassy phase particles, are also promising for fluorescence-based biosensing and imaging applications.

8.3 Exciton trapping by β-phase in polyfluorene dots

The glassy phase emission is completely quenched and the β-phase emission is dominant in the PFO nanoparticles containing only a small fraction of β-phase, indicating significant energy transfer from the glassy phase to β-phase domains. Efficient energy transfer from the glassy polymer to the β-phase has been observed in films as well.[160] These results are not surprising since the large spectral overlap between the glassy phase emission and the β-phase absorption would allow efficient energy transfer to occur via the Förster mechanism. It should be noted that for appreciable energy transfer to occur, both phases must be present in the majority of the nanoparticles – significant particle-to-particle heterogeneity in the relative fraction of β-phase would significantly reduce energy transfer since the inter-particle distances in the dispersion are far too large for appreciable inter-particle energy transfer to occur. Time-correlated single photon counting (TCSPC) technique was used to measure the fluorescence lifetimes of the mixed phase nanoparticles swelled at the THF/water ratio of 10% (Figure 8.4). No rise time due to energy transfer was resolved in the β-phase emission, consistent with previous thin films results that indicate energy transfer occurs within 5 ps,[160, 169] below the time resolution of the TCSPC apparatus. However, the TCSPC measurements indicate a

remarkable difference in fluorescence lifetimes of the glassy phase and β-phase. Fluorescence decay lifetimes were measured at the 0-0 peak for the two types of PFO nanoparticles, and lifetimes of 97 ps for the glassy phase and 178 ps for mixed phase nanoparticles were obtained. The increase in the lifetime for the mixed phase as compared to the glassy phase is also accompanied by an increase in the fluorescence quantum yield. The radiative rate constant k_R and non-radiative decay rate constant k_{NR} of the nanoparticles were determined by combining the quantum yield and fluorescence lifetime results. The obtained values are as follows: k_R=2.2 ns^{-1}, k_{NR}=8.1 ns^{-1} for the glassy phase, and k_R=2.0 ns^{-1}, k_{NR}=3.6 ns^{-1} for the mixed phase nanoparticles. These results indicate that the increased quantum yield for the mixed phase particles is due to their significantly lower non-radiative decay rate, while both types of particles exhibit similar radiative rates. There is currently not sufficient information to determine the origin of this difference in the non-radiative rate. One possibility is that differences in polymer morphology result in different rates of triplet or polaron generation/recombination between the two phases. The swelling process could also reduce disorder, which could reduce the number of the non-radiative channels. Additionally, the effect of disorder on the dipole-dipole coupling of excitons in many fluorescent aggregates[101, 170, 171] including polyfluorene aggregates[172] can lead to changes in radiative rate as well as in the exciton-phonon coupling, which could affect the non-radiative decay rate. Another possibility is that the minority β-phase domains act as exciton traps, reducing exciton mobility and therefore reducing the rate of energy transfer to quencher species such as hole polarons. This possibility is supported by our recent

report on the effect of dopant dyes on the quantum yield and photostability of conjugated polymer nanoparticles.[59]

In order to test the hypothesis that the β-phase domains act as exciton traps that reduce the efficiency of energy transfer to quenchers or other energy acceptors, we measured the effect of polymer morphology on the efficiency of energy transfer in dye-doped PFO nanoparticles. We previously demonstrated that dye-doped and polymer-doped polyfluorene nanoparticles (containing PDHF in the glassy phase) can exhibit efficient energy transfer to the dopant.[59, 106] The efficiency of energy transfer from the polymer to the dopant depends strongly on the spectral overlap between the emission spectrum of the donor and the absorption spectrum of the acceptor. Since the absorption and emission spectra of glassy phase and β-phase PFO are significantly different, polymer morphology is likely to have a strong affect on energy transfer efficiency. TPP-doped glassy nanoparticles were prepared by the reprecipitation method described above, but with 1% TPP relative to polymer in the precursor solution. The β-phase was formed in TPP-doped nanoparticles by THF swelling with a THF/water ratio of 10%. Based on our previous experiments,[59] the actual concentration of TPP dye in the nanoparticles is consistent with the composition of the precursor mixture and a small amount of THF in the swelling step does not lead to appreciable dye leakage. Figure 8.5a shows the absorption spectra of the TPP-doped glassy and β-phase nanoparticles. No obvious absorption peak from TPP is observed due to the low doping concentration, while the β-phase feature appears in the absorption band of PFO. Figure 8.5 b presents the fluorescence spectra of the TPP-doped glassy and β-phase nanoparticles (diluted to yield

an absorbance of 0.1 at the 375 nm excitation wavelength). The TPP-doped glassy nanoparticles exhibit a strong emission from the TPP acceptors, indicating efficient energy transfer from the PFO to the TPP. This is consistent with the Förster transfer mechanism: there is sufficient spectral overlap between the glassy PFO emission and the TPP absorption (inset of Figure 8.5 b), and the Förster radius for this donor-acceptor pair is determined to be 3.6-3.8 nm.[135, 136] However, the mixed phase particles show a clear decrease of the TPP fluorescence combined with the appearance of β-phase emission and a complete quenching of the emission of the glassy phase. The Förster radius for energy transfer from the glassy phase to the β-phase is relatively large as compared to that of TPP,[160] and the effective concentration of the β-phase is relatively high, both of which should result in a significantly higher energy transfer rate from the glassy phase to the β-phase as compared to the energy transfer rate from the glassy phase to the TPP dye. Furthermore, there is a small spectral overlap between the β-phase emission and the TPP absorption, and a relatively large average distance between β-phase polymer chains and the nearest TPP molecule, which should result in very low energy transfer efficiency from the β-phase to the TPP dye. To quantify the competitive energy transfer to the energy acceptors (TPP and β-phase PFO), the energy transfer efficiency (Q) can be calculated from

$$Q = \frac{k_{ET}}{k_R + k_{NR} + k_{ET}}. \tag{8.1}$$

Here the resonance energy transfer rate (k_{ET}) was estimated by the expression,[135, 136]

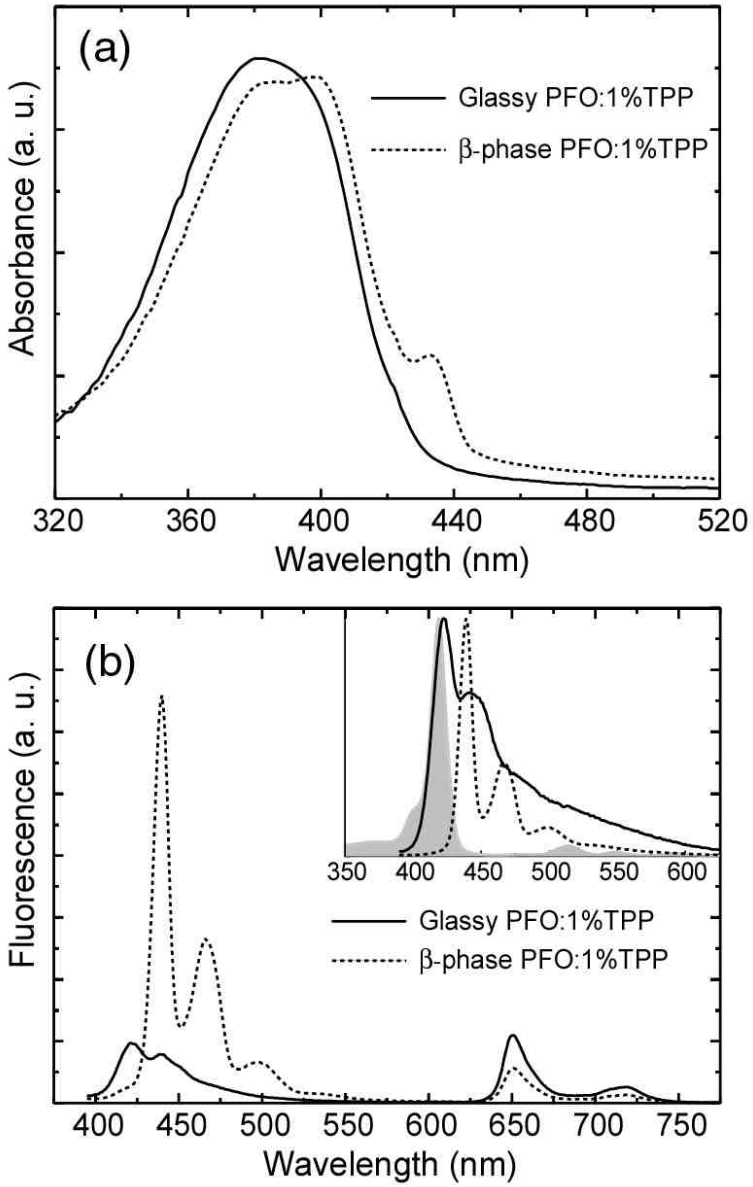

Figure 8.5 Absorption spectra (a) and fluorescence emission spectra (b) of TPP-doped glassy PFO (solid) and β-phase nanoparticles (dotted). The inset shows spectral overlap between the TPP absorption (gray) and fluorescence emission of glassy PFO (solid) and β-phase nanoparticles (dotted).

$$k_{ET} = \left(\frac{k_R}{\phi_A}\right)\left(\frac{I_A}{I_D}\right), \tag{8.2}$$

where I_D and I_A are the emission intensities of the donor and acceptor, and ϕ_A is the quantum yield of the acceptor. The integrated emission intensities (I_D and I_A) of the donor and acceptor can be obtained according to the emission spectra in Figure 8.5b. The fluorescence quantum yield (ϕ_A) of TPP in the PFO host was determined to be 8%. In the TPP-doped glassy nanoparticles, the energy transfer efficiency to TPP was calculated to be 66%. In the β-phase nanoparticles, the overall energy transfer efficiency to both TPP and β-phase PFO is nearly 100% since the donor's fluorescence is completely quenched. The relative transfer efficiencies to TPP and β-phase PFO were estimated to be 31% and 69%, respectively. Based on the above results, it is concluded that the β-phase effectively out competes the TPP as an energy acceptor (at small TPP loading ratios), and the β-phase does not subsequently transfer an appreciable amount of its energy to the TPP – in effect, the β-phase acts as an exciton trap, reducing the efficiency of energy transfer to the TPP. The observed reduction in polymer→dye energy transfer efficiency due to the exciton trapping by the β-phase supports the hypothesis that the higher quantum yield and reduced non-radiative decay rate of (undoped) mixed phase nanoparticles arises from reduced energy transfer to quencher species due to exciton trapping by the β-phase.

CHAPTER 9 ENERGY TRANSFER MEDIATED PHOSPHORESCENCE IN CONJUGATED POLYMER DOTS FOR BIOLOGICAL OXYGEN SENSING

Oxygen is a critical component for many physiological and pathological processes in living cells. In higher organisms, respiratory and cardiovascular systems provide and appropriately distribute oxygen to cells and tissues to maintain oxygen concentration in normal physiological range.[173, 174] Tissue hypoxia has been found to closely relate with the clinical course of a variety of diseases,[175] such as tumor growth,[176, 177] diabetic retinopathy,[178] and rheumatoid arthritis.[179] Therefore, measuring and imaging oxygen levels in live cells and tissue represent a challenging and significant problem in modern biology, physiology, and medicine. Considerable interest has been focused on the development of optical oxygen sensors based on phosphorescence quenching by molecular oxygen.[180-183] Oxygen sensing by phosphorescence quenching is noninvasive, sensitive, somewhat selective for oxygen (although some similar species such as NO can also act as quenchers), and can be implemented for real-time measurements [184, 185] as well as high-resolution oxygen mapping in tissue.[186, 187] While conventional phosphorescent dyes for oxygen sensing are typically based on organometallic complexes[188] and metalloporphyrins containing Pt or Pd,[189] there are continuing efforts to synthesize new chromophores with improved characteristics,[190, 191] or to modify them for applications such as multiphoton luminescent microscopy.[192]

In this Chapter, we present a novel nanoparticle oxygen sensor, which consists primarily of a conjugated polymer (polyfluorene) doped with a phosphorescent platinum porphyrin dye. The conjugated polymer polyfluorene possesses extraordinary "light harvesting" ability, yielding nanoparticle absorption cross-sections exceeding 10^{-12} cm^2 for nanoparticles of ~25 nm in diameter. Efficient energy transfer from the polymer to the phosphorescent dye was observed, resulting in bright phosphorescence that is highly sensitive to the concentration or partial pressure of molecular oxygen. Individual phosphorescent nanoparticles were imaged by fluorescence microscopy, and the observed phosphorescence decreased in direct relation to the partial pressure of oxygen. Nanoparticle uptake by macrophage cells via endocytosis was observed. The small size, extraordinary brightness, excellent sensitivity, and ratiometric emission of the doped conjugated polymer nanoparticles, together with the demonstration of single particle sensing and cellular uptake, indicate the potential of the nanoparticle sensors for quantitative mapping of local molecular oxygen concentration in living cells and tissues.

9.1 Energy transfer in PtOEP-doped conjugated polymer dots

The conjugated polymers employed as the doping host are the polyfluorene derivatives poly(9,9-dihexylfluorene) (PDHF) and poly(9,9-dioctylfluorene) (PFO). Platinum (II) octaethylporphine (PtOEP) served as the oxygen sensitive dye (structures provided in Figure 9.1a). The preparation of the nanoparticle sensors is briefly described as follows. Rapid addition of a tetrahydrofuran (THF) solution containing polyfluorene and PtOEP to water, followed by mixing, leads to the collapse of polymer chains due to the sudden decrease in solvent quality, resulting in nanoparticle formation and

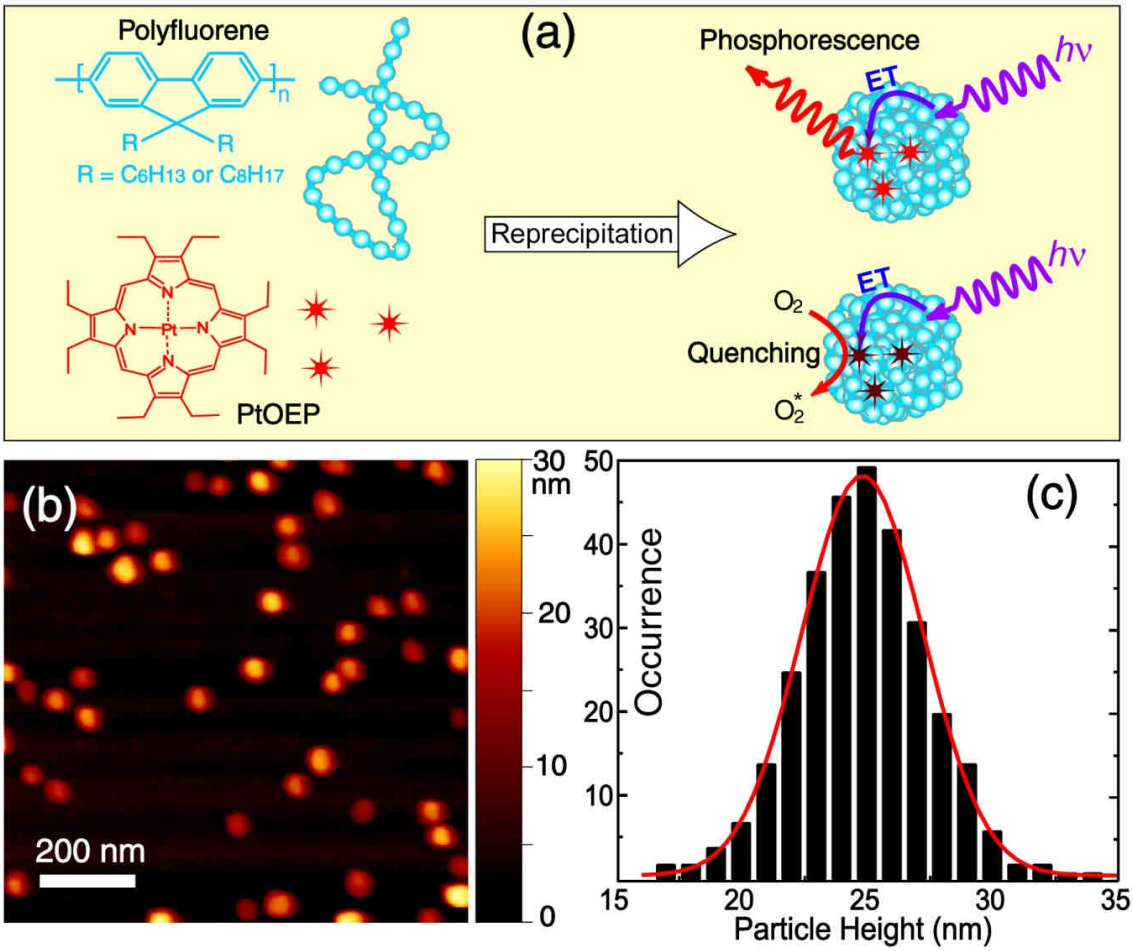

Figure 9.1 PtOEP-doped conjugated polymer dots for oxygen sensing. (a) Schematic illustration of the formation of conjugated polymer dots for oxygen sensing. Chemical structures of the polyfluorenes and platinum porphyrin are also shown on the left. (b) A representative AFM image of PtOEP-doped PDHF dots dispersed on a mica substrate. (c) Histogram of particle height data obtained from the AFM image.

simultaneous entrapment the hydrophobic PtOEP molecules inside the nanoparticles. For PDHF-based particles, the AFM results indicate that the resulting particles are approximately spherical in shape, with particle heights (diameters) in the range of 25±5 nm (Figure 9.1b). For PFO-based particles, it was found that the preparation conditions (in particular, the ratio of THF to water) affected the polymer phase (glassy phase versus β-phase) in the resulting nanoparticles and the polymer phase has a strong effect on the efficiency of energy transfer to dye dopants.[57] In agreement with previous results, the glassy PFO phase particles were found to exhibit more efficient energy transfer to PtOEP than the β-phase PFO particles. The 10 wt% PtOEP-doped PFO particles also exhibit roughly spherical morphology, with particle sizes in the range of 50±10 nm.

Aqueous dispersions of the PtOEP-doped CPdots are clear and stable, with a faint pink color due to the visible absorption peak at 534 nm from PtOEP (Figure 9.2a inset). Our prior results indicated that the ratio of dye to polymer in the CPdots is similar to that of the precursor solution, with no appreciable dye leakage.[59] UV-Vis absorption spectra (Figure 9.2a) are consistent with the dye/polymer weight ratio (1/10) of the precursor solution, and the absorption cross-sections (~380 nm) of PtOEP-doped PDHF and PFO nanoparticles in water were determined to be ~1.9×10^{-12} cm^2 and ~1.2×10^{-11} cm^2, respectively. According to the particle size and the weight ratio of dye to polymer, it is estimated that each doped PDHF particle (~25 nm dia.) consists of ~90 PDHF molecules and ~700 PtOEP molecules. Both PDHF and PtOEP contribute to the nanoparticle absorption at 380 nm, and their relative contributions are estimated at ~80% from PDHF and ~20% from PtOEP, respectively. Similarly, each doped PFO particle (~50 nm dia.)

contains ~270 PFO molecules and ~5500 PtOEP molecules. The large absorption cross-sections of the CPdots (roughly 20 times higher than those of dye-loaded silica or polymer particles of similar dimensions) provides clear indication of the potential brightness advantage of the polyfluorene-based particles.

The Förster radius characterizing the efficiency of energy transfer between the PFO donor and the PtOEP acceptor was calculated to be ~1.7 nm, which is somewhat small due to the non-optimal spectral overlap as shown in Figure 9.2b. However, exciton diffusion in the conjugated polymer host is known to result in a marked improvement in energy transfer efficiency. We previously developed a random walk model for estimating energy transfer efficiency in dye-doped conjugated polymer nanoparticles based on the polymer exciton diffusion length, dye-polymer Förster radius, particle size, and dopant concentration.[59] The model result for the energy transfer efficiency for 10% PtOEP-doped PFO nanoparticles (~50 nm) was ~89%, in good agreement with the experimental value (~87%) obtained from fluorescence spectra (Figure 9.2c). Time-resolved fluorescence measurements were performed to provide information about the rate of energy transfer in the nanoparticles (Figure 9.2d). A fluorescence lifetime of 110 ps was obtained from the decay curves of the 420 nm emission of the undoped PFO dots, and the lifetime was decreased to 18 ps for the 10% PtOEP-doped PFO dots due primarily to energy transfer. The energy transfer rate constant (k_{ET}) was deduced by subtracting the decay rate constant of undoped dots (τ_D^{-1}=9 ns^{-1}) from the total decay rate constant of the doped nanoparticles (τ_D^{-1}=56 ns^{-1}). The result (k_{ET}=47 ns^{-1}) is in good agreement with the value obtained from analysis of the fluorescence spectra and the predictions of the

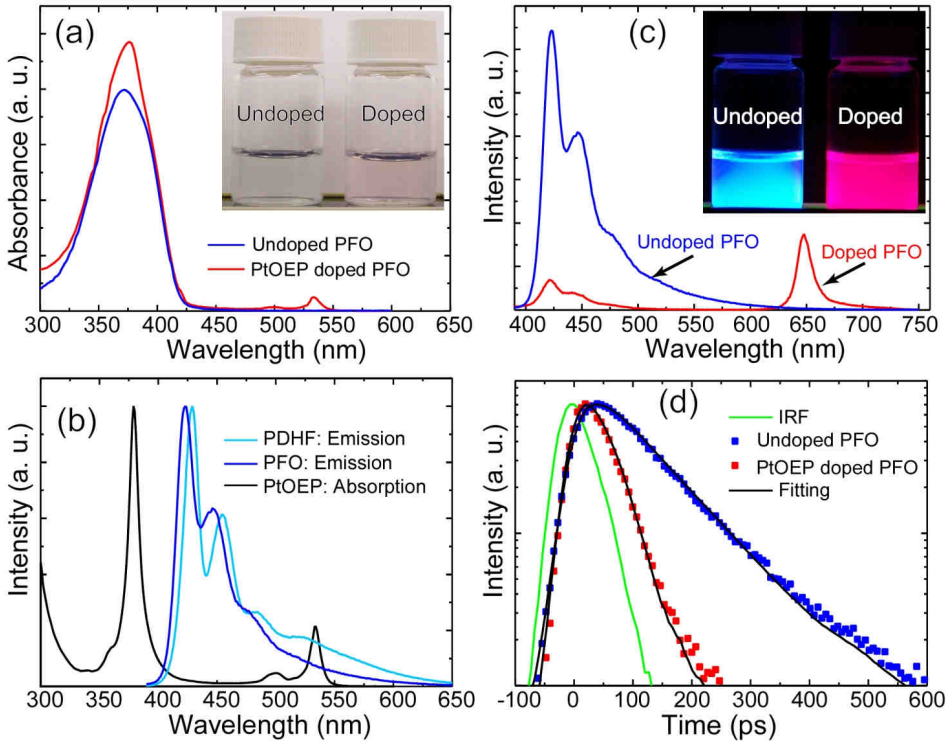

Figure 9.2 Energy transfer in PtOEP-doped conjugated polymer dots. (a) UV-vis absorption spectra of the undoped, PtOEP-doped PFO dots in water. The inset presents aqueous dispersion of PFO dots under room light. (b) Spectral overlap between fluorescence emission of polyfluorene nanoparticles and absorption of the PtOEP dye. (c) Emission spectra of the undoped and PtOEP-doped PFO nanoparticles with an excitation wavelength of 350 nm. The inset shows aqueous dispersion of PFO dots under a UV lamp (365 nm). (d) Fluorescence decays of the undoped and PtOEP-doped PFO dots measured by a TCSPC setup. The green curve shows the instrumental response function (IRF). The scattered symbols represent experimental data, and the solid lines are fits.

nanoparticle energy transfer model. The inset of Figure 9.2c presents a photograph of aqueous nanoparticle dispersions under UV lamp illumination (365 nm), illustrating a clear difference in the fluorescence color of undoped versus doped PFO nanoparticles. The emission spectra in Figure 9.2c were obtained at an excitation wavelength of 350 nm where the absorption of PtOEP is negligible. As compared to the undoped PFO dots, the doped dots exhibited significantly reduced PFO fluorescence and strong red emission (650 nm) from PtOEP, consistent with energy transfer mediated phosphorescence in the doped particles. For the PtOEP-doped PFO dots (nitrogen-saturated solution), the phosphorescence quantum yield was determined to be ~9% by (a dilute solution of tetraphenylporphyrin in toluene was used as a standard). This result is somewhat lower than that of PtOEP doped PFO thin film devices (~20%),[193] likely due to the higher doping concentration in nanoparticles, which leads to increased self-quenching. The nanoparticle phosphorescence brightness, defined as the product of the optical cross section and the phosphorescence quantum yield, is more than 1000 times higher than that of conventional oxygen sensing dyes, and is estimated as roughly 5-10 times higher than that of PtOEP-doped silica particles of similar dimensions at similar dye loading. The enhanced brightness is due to the combination of efficient light harvesting by the polymer and efficient energy transfer to PtOEP.

9.2 PtOEP doped polyfluorene dots for oxygen sensing

Oxygen sensitive phosphorescence is readily observed from aqueous PtOEP-doped CPdot suspensions at different dissolved oxygen concentrations (Figure 9.3). As can be seen from inset, the nitrogen-saturated CPdot suspension exhibits intense red

emission, while the air- and oxygen-saturated samples present weaker emission due to quenching by oxygen. The emission spectra (Figure 9.3a) exhibit a moderate fluorescence (~420 nm) from the PDHF host and oxygen-dependent phosphorescence (~650 nm) from PtOEP dopant. The fluorescence from PDHF is not completely quenched at the current doping concentration, which is attributable to the non-optimal spectral overlap between the donor and acceptor discussed above. Significantly, the residual fluorescence from the donor (~420 nm) remains relatively constant while the acceptor phosphorescence (~650 nm) is highly sensitive to oxygen, facilitating ratiometric sensing, which is useful for applications such as cellular and tissue imaging of oxygen concentration, since the ratio of acceptor to donor fluorescence is relatively insensitive to the local nanoparticle concentration. Defining *R* as the ratio of the emission intensity of the acceptors (sensing dye) to that of the donors (polymer reference), the sensor sensitivity can be expressed by the overall quenching response to dissolved oxygen,[184, 185]

$$Q = (R_{N_2} - R_{O_2}) / R_{N_2}, \tag{9.1}$$

where R_{N_2} and R_{O_2} represent the emission intensity ratios of the sensor in fully deoxygenated and fully oxygenated solution, respectively. The measured *Q* value for the doped CPdot particles is ~95%, similar to other quenching-based sensors.[184] Phosphorescence lifetime measurements provide an alternative method for quantitative oxygen sensing.[42] A comparison of the phosphorescence decays of the 10% PtOEP doped PDHF dots in nitrogen, air, and oxygen-saturated solutions is shown in Figure 9.3b. Each decay curve exhibits single exponential decay kinetics, indicating a homogeneous distribution of the PtOEP molecules inside the nanoparticles. A phosphorescence lifetime

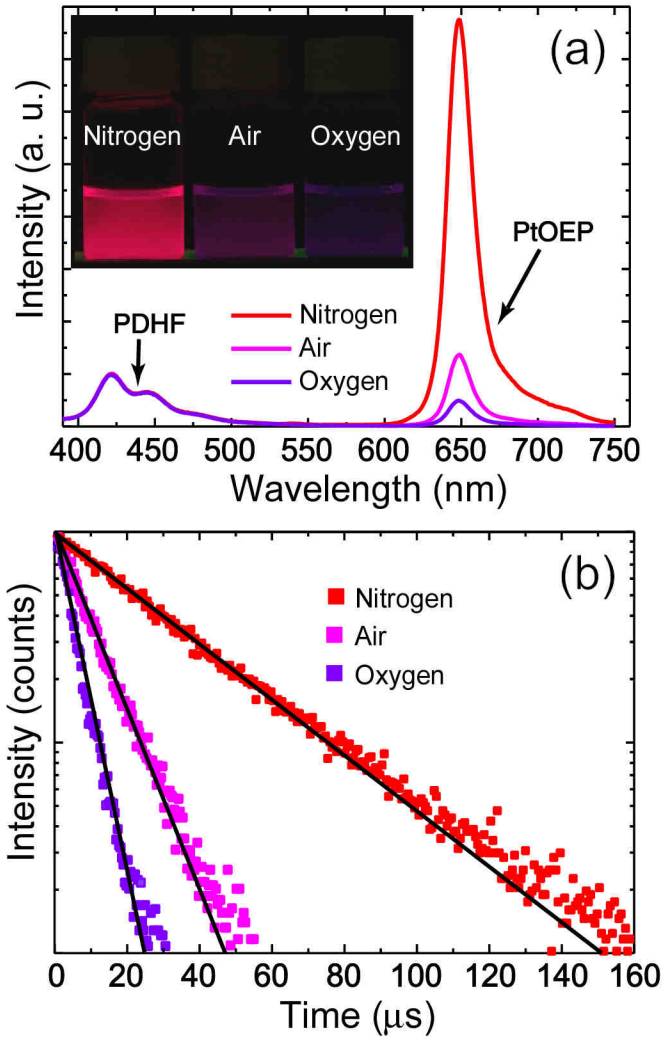

Figure 9.3 Oxygen dependent phosphorescence intensity and lifetime in PtOEP-doped CPdots. (a) Oxygen dependent emission spectra of the 10% PtOEP-doped PDHF dots with an excitation wavelength of 350 nm. The inset illustrates the UV lamp-illuminated emission from the doped PDHF dots in aqueous solutions saturated with nitrogen, air, and oxygen, respectively. (b) Phosphorescence decays of the PtOEP-doped PDHF dots under the same conditions as in (a). The scattered symbols represent experimental data, and the solid lines are fits.

of ~37 μs was obtained for the nitrogen-saturated nanoparticle dispersion, consistent with the lifetime results (30-50 μs) of PtOEP in a variety of organic thin film devices.[193, 194] The phosphorescence lifetime is decreased to ~10 μs for the air-saturated nanoparticle solution, and ~5 μs for the fully oxygenated solution, indicating efficient quenching of phosphorescence by molecular oxygen. Quenching by molecular oxygen is rapidly and completely reversed by subsequent bubbling of N_2 through the nanoparticle suspension.

The large optical cross-section, bright phosphorescence, and high oxygen sensitivity of the doped CPdots show great potential for mapping oxygen concentration in biological systems. The relatively small particle size (~25 nm) is advantageous for cellular uptake and distribution as compared to other particle sensors, which are typically much larger.[184, 185] The small size also provides a large surface-to-volume ratio and a reduced distance that the oxygen must diffuse to reach the dyes, which should lead to excellent response time. The sensitivity, selectivity, and response time also depend on the doping matrix, in this case the conjugated polymer. Polyfluorenes such as PDHF and PFO are hydrophobic glassy polymers, which should exhibit good oxygen permeability while serving as a barrier to interfering ionic species. In a qualitative experiment, a nitrogen-saturated CPdots dispersion was excited by a UV lamp (365 nm). The bright phosphorescence was observed to dim within in a few seconds upon exposure to air, a qualitative indication of adequate oxygen permeability and response time for a wide variety of applications. Additionally, we recently determined that CPdots exhibit extraordinarily large cross-sections for two-photon excitation (as high as 10^5 GM),[68]

which suggests that the nanoparticles are promising for 3D oxygen mapping in tissue using two-photon based imaging techniques.[192]

9.3 Single particle oxygen sensing

Single particle phosphorescence imaging was performed to further test the brightness and sensing capabilities of the CPdot sensors. Single molecule detection of triplet emission in transition metal complexes represents a challenging task, due to typically low phosphorescence quantum yields and very low radiative rates.[195-197] The PtOEP-doped CPdots are expected to present substantially brighter phosphorescence than that of single phosphorescent molecules due to the large number of phosphorescent chromophores per particle (~700 phosphorescent chromophores in a particle of ~25 nm diameter). However, the excitation intensity must be carefully controlled for the case of the PtOEP-doped nanoparticles, since phosphorescence from the doped CPdots is readily saturated under high excitation intensity, while the fluorescence of the donor is less susceptible to saturation effects, resulting in donor polymer emission that greatly exceeds that of the PtOEP, as well as reduced sensitivity of the PtOEP emission to oxygen. Single doped PDHF dots (particle size: ~25 nm) were immobilized on a glass coverslip and imaged using a custom built wide-field epifluorescence microscope. The 405 nm excitation laser was attenuated to an intensity of ~25 mW/cm^2 in the center of the laser spot in the sample plane, corresponding to roughly 5×10^4 photons/sec absorbed per nanoparticle – well below saturation. Single particle phosphorescence images of the CPdots under flowing nitrogen (left) and in air (right) were obtained (Figure 9.4a). Each peak in the image corresponds to a single doped CPdot, exhibiting a near-diffraction-

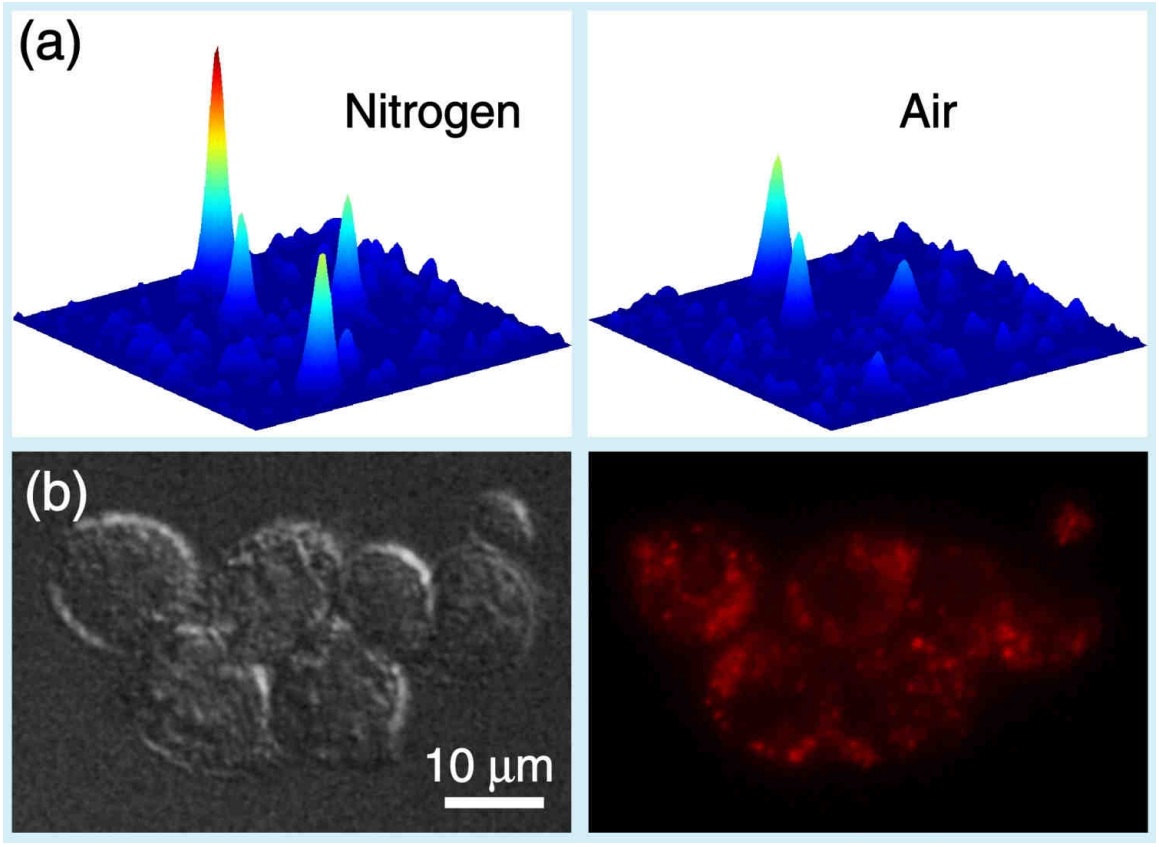

Figure 9.4 Single particle phosphorescence imaging and cellular imaging. (a) Single particle phosphorescence images of the doped CPdots immobilized on a coverslip under nitrogen and air atmosphere, respectively. (b) DIC and phosphorescence images indicating uptake of the nanoparticle sensor by macrophage cells.

limited Airy disk with a full width at half maximum of ~300 nm. Phosphorescence from a single CPdot particle on the coverslip exhibits sensitivity to oxygen content in the atmosphere above the coverslip. The phosphorescence intensity corresponding to a single particle obtained in air atmosphere clearly shows that the phosphorescence is substantially quenched by oxygen. Subsequent imaging on the sample after resuming nitrogen flow shows near-complete recovery of the phosphorescence intensity (Figure 9.4a left). The intensity changes were observed for over several nitrogen-air cycles, with no apparent photobleaching owing to the low excitation intensity employed. The single particle oxygen sensing results provide clear indication that the nanoparticles are sufficiently bright and sensitive for a wide range of imaging and sensing applications.

9.4 Phosphorescence cellular imaging

There is considerable current interest in the use of nanoparticles for intracellular imaging and sensing. A variety of strategies for intracellular delivery and targeting of nanoparticles have been developed.[22, 102] In previous studies, large oxygen sensing particles have also been delivered into living cells by gene gun insertion.[184, 185] Motivated by the notion that the small particle size should facilitate cellular uptake by pinocytosis ("cell drinking"),[198] and the possibility of using such nanoparticles as fluid phase markers to monitor endocytosis, we performed fluorescence microscopy experiments in order to observe nanoparticle uptake by live J774.A1 macrophages. Macrophage cells were plated in microscope dishes, and allowed to incubate for 10 hours with culture media containing doped PDHF dots at a concentration of ~10 pM. An epifluorescence microscope equipped with a Xe arc lamp and appropriate beamsplitter and filters was used to evaluate

nanoparticle uptake. Figure 9.4b presents the differential interference contrast (DIC) image and phosphorescence image of macrophages labeled with the doped CPdots. These images clearly indicate nanoparticle uptake by the cells and show a staining pattern consistent with other widely used fluid-phase markers such as an organic dye conjugated to a high molecular weight dextran. Consistent with fluid-phase uptake of CPdots, these images also show perinuclear labeling and brightly fluorescent vacuoles and organelles (e.g. pinosomes and lysosomes). More diffuse nanoparticle fluorescence was apparently localized in the cytoplasm, which may be due to a population of nanoparticles that are able to cross cell membranes. A detailed understanding of the factors affecting nanoparticle uptake as well as the fate of the nanoparticles requires additional investigation. In addition, sensing of oxygen concentration in specific subcellular organelles will require targeting of the nanoparticles to the organelle via encapsulation and bioconjugation. Nevertheless, the high brightness of the nanoparticles at low loading levels and low excitation levels, as well as the facile uptake by cells, are promising for applications such as determining local oxygen concentration in living cells.

CHAPTER 10 CONCLUSIONS AND OUTLOOK

This dissertation has demonstrated a facile reprecipitation method for preparation of a variety of fluorescent conjugated polymer dots. Quantitative comparisons of the optical properties of the CPdots indicate their fluorescence brightness is a factor of 10^2-10^4 higher than that of conventional fluorescent dyes, and a factor of 10-10^3 higher than that of inorganic quantum dots, depending on particle size that ranges from 5 nm to 30 nm. Single particle fluorescence imaging and kinetic studies indicate much higher emission rates (~10^8 s^{-1}) and little or no blinking of the CPdots as compared to typical results for single dye molecules and quantum dots. Photobleaching results for various CPdots reveal excellent photostability – as many as 10^9 or more photons emitted per nanoparticle prior to irreversible photobleaching. Two-photon excited fluorescence from the CPdot nanoparticles has also been characterized, and their two-photon action cross sections can be as high as 2.0×10^5 GM, to our knowledge the largest reported thus far for a nanoparticle.

We have also utilized energy transfer as a strategy for tuning the emission color, improving nanoparticle photostability and quantum yield, and designing novel sensors. Blended CPdots consisting of a blue-emitting polyfluorene doped with green, yellow, and red-emitting conjugated polymers show improved quantum yield, and enlarged energy gap between absorption and fluorescence as compared to the pure polymer dots. Surprisingly, nearly all of the excitation energy absorbed by hundreds of polyfluorene

molecules is transferred to a single quencher molecule, a phenomenon referred to as "superquenching", which is the basis for highly sensitive biosensors based on fluorescence quenching. We have also investigated the combined effects of energy diffusion and energy transfer in polyfluorene nanoparticles doped with a variety of fluorescent dyes. A stochastic model which takes into account the combined effects of energy diffusion, Förster transfer to the dye, dye concentration, and particle size effects was developed. Comparisons of experimental data to the model results helped to provide a more accurate physical picture of the ultrafast energy diffusion and energy transfer processes that can occur in conjugated polymers. Moreover, the very efficient intra-particle energy transfer could be exploited to design highly sensitive sensors for small molecules such as oxygen. We observed efficient intra-particle energy transfer from the polymer to the phosphorescent dye, resulting in bright phosphorescence that is highly sensitive to the concentration or partial pressure of molecular oxygen. Single particle sensing and cellular uptake were demonstrated, indicating the potential of the nanoparticle sensors for quantitative mapping of local molecular oxygen concentration in living cells and tissues.

In summary, this research involves the design, development, and characterization of highly fluorescent and photostable CPdots. Significant features of these nanoparticles include their small size, high brightness, excellent photostability, fast emission rates, non-blinking, and tunable fluorescent functionalities mediated by energy transfer. These combined features of the CPdots indicate that CPdots are promising probes for demanding fluorescence-based applications such as high speed super-resolution single

molecule/particle tracking in live cells and highly sensitive assays. CPdots would yield substantially improved signal levels for these photon-starved applications that have previously involved multiple dye labeling, quantum dots, or dye-loaded particles, likely increasing the feasibility of such techniques for a wider range of problems. While the results reported here are highly encouraging, CPdots constitute a new and as yet relatively undeveloped nanoparticle technology. Continued efforts will involve additional experiments and development of theory aimed at understanding photophysics, further attempts to improve the optical properties of the nanoparticles, targeted cellular imaging by encapsulation and bioconjugation, and exploration of CPdots for single biomolecule tracking and dynamics in live cells.

REFERENCES

1. Moerner, W. E.; Kador, L., Optical-Detection and Spectroscopy of Single Molecules in a Solid. *Phys. Rev. Lett.* **1989,** 62, 2535-2538.

2. Orrit, M.; Bernard, J., Single Pentacene Molecules Detected by Fluorescence Excitation in a Para-Terphenyl Crystal. *Phys. Rev. Lett.* **1990,** 65, 2716-2719.

3. Betzig, E.; Grubb, S. G.; Chichester, R. J.; Digiovanni, D. J.; Weiner, J. S., Fiber Laser Probe for near-Field Scanning Optical Microscopy. *Appl. Phys. Lett.* **1993,** 63, 3550-3552.

4. Moerner, W. E.; Plakhotnik, T.; Irngartinger, T.; Wild, U. P.; Pohl, D. W.; Hecht, B., Near-Field Optical Spectroscopy of Individual Molecules in Solids. *Phys. Rev. Lett.* **1994,** 73, 2764-2767.

5. Nie, S.; Chiu, D. T.; Zare, R. N., Probing Individual Molecules with Confocal Fluorescence Microscopy. *Science* **1994,** 266, 1018-1021.

6. Moerner, W. E., A Dozen Years of Single Molecule Spectroscopy in Physics, Chemistry, and Biophysics. *J. Phys. Chem. B* **2002,** 106, 910.

7. Moerner, W. E., New Directions in Single-Molecule Imaging and Analysis. *Proc. Natl. Acad. Sci. USA* **2007,** 104, 12596-12602.

8. Dobson, C. M., Protein Folding and Misfolding. *Nature* **2003,** 426, 884-890.

9. Michalet, X.; Weiss, S.; Jager, M., Single-Molecule Fluorescence Studies of Protein Folding and Conformational Dynamics. *Chem. Rev.* **2006,** 106, 1785-1813.

10. Royer, C. A., Probing Protein Folding and Conformational Transitions with Fluorescence. *Chem. Rev.* **2006,** 106, 1769-1784.

11. Smiley, R. D.; Hammes, G. G., Single Molecule Studies of Enzyme Mechanisms. *Chem. Rev.* **2006,** 106, 3080-3094.

12. Yildiz, A.; Forkey, J. N.; McKinney, S. A.; Ha, T.; Goldman, Y. E.; Selvin, P. R., Myosin V Walks Hand-over-Hand: Single Fluorophore Imaging with 1.5 nm Localization. *Science* **2003,** 300, 2061-2065.

13. Ha, T.; Ting, A. Y.; Liang, J.; Caldwell, W. B.; Deniz, A. A.; Chemla, D. S.; Schultz, P. G.; Weiss, S., Single-Molecule Fluorescence Spectroscopy of Enzyme Conformational Dynamics and Cleavage Mechanism. *Proc. Natl. Acad. Sci. USA* **1999,** 96, 893-898.

14. Yu, J.; Xiao, J.; Ren, X. J.; Lao, K. Q.; Xie, X. S., Probing Gene Expression in Live Cells, One Protein Molecule at a Time. *Science* **2006,** 311, 1600-1603.

15. Xie, X. S.; Yu, J.; Yang, W. Y., Perspective - Living Cells as Test Tubes. *Science* **2006,** 312, 228-230.

16. Abbondanzieri, E. A.; Bokinsky, G.; Rausch, J. W.; Zhang, J. X.; Le Grice, S. F. J.; Zhuang, X. W., Dynamic Binding Orientations Direct Activity of Hiv Reverse Transcriptase. *Nature* **2008,** 453, 184-189.

17. Thompson, R. E.; Larson, D. R.; Webb, W. W., Precise Nanometer Localization Analysis for Individual Fluorescent Probes. *Biophys. J.* **2002,** 82, 2775-2783.

18. Plakhotnik, T.; Donley, E. A.; Wild, U. P., Single-Molecule Spectroscopy. *Annu. Rev. Phys. Chem.* **1997,** 48, 181-212.

19. Eggeling, C.; Widengren, J.; Rigler, R.; Seidel, C. A. M., Photobleaching of Fluorescent Dyes under Conditions Used for Single-Molecule Detection: Evidence of Two-Step Photolysis. *Anal. Chem.* **1998,** 70, 2651-2659.

20. Golding, I.; Cox, E. C., Rna Dynamics in Live Escherichia Coli Cells. *Proc. Natl. Acad. Sci. USA* **2004,** 101, 11310-11315.

21. Bruchez, M.; Moronne, M.; Gin, P.; Weiss, S.; Alivisatos, A. P., Semiconductor Nanocrystals as Fluorescent Biological Labels. *Science* **1998,** 281, 2013-2016.

22. Michalet, X.; Pinaud, F. F.; Bentolila, L. A.; Tsay, J. M.; Doose, S.; Li, J. J.; Sundaresan, G.; Wu, A. M.; Gambhir, S. S.; Weiss, S., Quantum Dots for Live Cells, in Vivo Imaging, and Diagnostics. *Science* **2005,** 307, 538-544.

23. Smith, A. M.; Duan, H. W.; Rhyner, M. N.; Ruan, G.; Nie, S. M., A Systematic Examination of Surface Coatings on the Optical and Chemical Properties of Semiconductor Quantum Dots. *Phys. Chem. Chem. Phys.* **2006,** 8, 3895-3903.

24. Liu, W.; Howarth, M.; Greytak, A. B.; Zheng, Y.; Nocera, D. G.; Ting, A. Y.; Bawendi, M. G., Compact Biocompatible Quantum Dots Functionalized for Cellular Imaging. *J. Am. Chem. soc.* **2008,** 130, 1274-1284.

25. Yao, J.; Larson, D. R.; Vishwasrao, H. D.; Zipfel, W. R.; Webb, W. W., Blinking and Nonradiant Dark Fraction of Water-Soluble Quantum Dots in Aqueous Solution. *Proc. Natl. Acad. Sci. USA* **2005,** 102, 14284-14289.

26. Wang, L.; Wang, K. M.; Santra, S.; Zhao, X. J.; Hilliard, L. R.; Smith, J. E.; Wu, J. R.; Tan, W. H., Watching Silica Nanoparticles Glow in the Biological World. *Anal. Chem.* **2006,** 78, 646-654.

27. Hide, F.; DiazGarcia, M. A.; Schwartz, B. J.; Heeger, A. J., New Developments in the Photonic Applications of Conjugated Polymers. *Acc. Chem. Res.* **1997,** 30, 430-436.

28. Friend, R. H.; Gymer, R. W.; Holmes, A. B.; Burroughes, J. H.; Marks, R. N.; Taliani, C.; Bradley, D. D. C.; Dos Santos, D. A.; Bredas, J. L.; Loglund, M.; Salaneck, W. R., Electroluminescence in Conjugated Polymers. *Nature* **1999,** 397, 121-128.

29. So, F.; Krummacher, B.; Mathai, M. K.; Poplavskyy, D.; Choulis, S. A.; Choong, V. E., Recent Progress in Solution Processable Organic Light Emitting Devices. *J. Appl. Phys.* **2007,** 102, 091101.

30. Landfester, K.; Montenegro, R.; Scherf, U.; Guntner, R.; Asawapirom, U.; Patil, S.; Neher, D.; Kietzke, T., Semiconducting Polymer Nanospheres in Aqueous Dispersion Prepared by a Miniemulsion Process. *Adv. Mater.* **2002,** 14, 651-655.

31. Kietzke, T.; Neher, D.; Landfester, K.; Montenegro, R.; Guntner, R.; Scherf, U., Novel Approaches to Polymer Blends Based on Polymer Nanoparticles. *Nature Mater.* **2003,** 2, 408-412.

32. Landfester, K., The Generation of Nanoparticles in Miniemulsions. *Adv. Mater.* **2001,** 13, 765-768.

33. Kurokawa, N.; Yoshikawa, H.; Hirota, N.; Hyodo, K.; Masuhara, H., Size-Dependent Spectroscopic Properties and Thermochromic Behavior in Poly(Substituted Thiophene) Nanoparticles. *Chemphyschem* **2004,** 5, 1609-1615.

34. Chen, L.; McBranch, D. W.; Wang, H. L.; Helgeson, R.; Wudl, F.; Whitten, D. G., Highly Sensitive Biological and Chemical Sensors Based on Reversible Fluorescence Quenching in a Conjugated Polymer. *Proc. Natl. Acad. Sci. USA* **1999,** 96, 12287-12292.

35. Fan, C. H.; Wang, S.; Hong, J. W.; Bazan, G. C.; Plaxco, K. W.; Heeger, A. J., Beyond Superquenching: Hyper-Efficient Quenching Energy Transfer from Conjugated Polymers to Gold Nanoparticles. *Proc. Natl. Acad. Sci. USA USA* **2003,** 100, 6297-6301.

36. Pei, Q. B.; Yang, Y., Efficient Photoluminescence and Electroluminescence from a Soluble Polyfluorene. *J. Am. Chem. Soc.* **1996,** 118, 7416-7417.

37. Ambrose, W. P.; Basche, T.; Moerner, W. E., Detection and Spectroscopy of Single Pentacene Molecules in a Para-Terphenyl Crystal by Means of Fluorescence Excitation. *J. Chem. Phys.* **1991,** 95, 7150-7163.

38. Forster, T., Intermolecular Energy Migration and Fluorescence. *Ann. Phys.* **1948,** 2, 55-75.

39. Ha, T.; Zhuang, X. W.; Kim, H. D.; Orr, J. W.; Williamson, J. R.; Chu, S., Ligand-Induced Conformational Changes Observed in Single Rna Molecules. *Proc. Natl. Acad. Sci. USA* **1999,** 96, 9077-9082.

40. Medintz, I. L.; Clapp, A. R.; Mattoussi, H.; Goldman, E. R.; Fisher, B.; Mauro, J. M., Self-Assembled Nanoscale Biosensors Based on Quantum Dot Fret Donors. *Nature Mater.* **2003,** 2, 630-638.

41. Berggren, M.; Dodabalapur, A.; Slusher, R. E.; Bao, Z., Light Amplification in Organic Thin Films Using Cascade Energy Transfer. *Nature* **1997,** 389, 466-469.

42. Lakowicz, J. R., *Principles of Fluorescence Spectroscopy, Third Edition*. Springer: 2006.

43. Xie, X. S.; Trautman, J. K., Optical Studies of Single Molecules at Room Temperature. *Annu. Rev. Phys. Chem.* **1998,** 49, 441-480.

44. Moerner, W. E.; Orrit, M., Illuminating Single Molecules in Condensed Matter. *Science* **1999,** 283, 1670-1676.

45. Moerner, W. E.; Fromm, D. P., Methods of Single-Molecule Fluorescence Spectroscopy and Microscopy. *Rev. Sci. Instrum.* **2003,** 74, 3597-3619.

46. Wu, C.; Szymanski, C.; McNeill, J., Preparation and Encapsulation of Highly Fluorescent Conjugated Polymer Nanoparticles. *Langmuir* **2006,** 22, 2956-2960.

47. Szymanski, C.; Wu, C.; Hooper, J.; Salazar, M. A.; Perdomo, A.; Dukes, A.; McNeill, J. D., Single Molecule Nanoparticles of the Conjugated Polymer MEH-PPV, Preparation and Characterization by Near-Field Scanning Optical Microscopy. *J. Phys. Chem. B* **2005,** 109, 8543 - 8546.

48. Binnig, G.; Quate, C. F.; Gerber, C., Atomic Force Microscope. *Phys. Rev. Lett.* **1986,** 56, 930-933.

49. Xu, C.; Webb, W. W., Measurement of Two-Photon Excitation Cross Sections of Molecular Fluorophores with Data from 690 to 1050 nm. *J. Opt. Soc. Am. B* **1996,** 13, 481-491.

50. Press, W. H.; Teukolsky, S. A.; Vetterling, W. T.; Flannery, B. P., *Numerical Recipes in C*. Cambridge University Press: Cambridge, 1988.

51. Wu, C.; Bull, B.; Szymanski, C.; Christensen, K.; McNeill, J., Multicolor Conjugated Polymer Dots for Biological Fluorescence Imaging. *ACS Nano* **2008,** 2, 2415-2423.

52. Schwartz, B. J., Conjugated Polymers as Molecular Materials: How Chain Conformation and Film Morphology Influence Energy Transfer and Interchain Interactions. *Annu. Rev. Phys. Chem.* **2003,** 54, 141-172.

53. Chandler, D., Interfaces and the Driving Force of Hydrophobic Assembly. *Nature* **2005,** 437, 640-647.

54. ten Wolde, P. R.; Chandler, D., Drying-Induced Hydrophobic Polymer Collapse. *Proc. Natl. Acad. Sci. USA* **2002,** 99, 6539-6543.

55. Wong, K. F.; Skaf, M. S.; Yang, C.-Y.; Rossky, P. J.; Bagchi, B.; Hu, D.; Yu, J.; Barbara, P. F., Structural and Electronic Characterization of Chemical and Conformational Defects in Conjugated Polymers. *J. Phys. Chem. B* **2001,** 105, 6103-6107.

56. Nguyen, T.-Q.; Martini, I. B.; Liu, J.; Schwartz, B. J., Controlling Interchain Interactions in Conjugated Polymers: The Effects of Chain Morphology on Exciton-Exciton Annihilation and Aggregation in Meh-Ppv Films. *J. Phys. Chem. B* **2000,** 104, 237-255.

57. Wu, C.; McNeill, J., Swelling-Controlled Polymmer Phase and Fluorescence Properties in Polyfluorene Nanoparticles. *Langmuir* **2008,** 24, 5855-5861.

58. Bunz, U. H. F.; Imhof, J. M.; Bly, R. K.; Bangcuyo, C. G.; Rozanski, L.; Vanden Bout, D. A., Photophysics of Poly [P-(2,5-Didodecylphenylene)Ethynylene] in Thin Films. *Macromol.* **2005,** 38, 5892-5896.

59. Wu, C.; Zheng, Y.; Szymanski, C.; McNeill, J., Energy Transfer in a Nanoscale Multichromophoric System: Fluorescent Dye Doped Conjugated Polymer Nanoparticles. *J. Phys. Chem. C* **2008,** 112, 1772-1781.

60. Onodera, T.; Kasai, H.; Okada, S.; Oikawa, H.; Mizuno, K.; Fujitsuka, M.; Ito, O.; Nakanishi, H., Temperature- and Size-Effects on Optical Properties of Perylene Microcrystals. *Opt. Mater.* **2003,** 21, 595-598.

61. Nan, X. L.; Sims, P. A.; Xie, X. S., Organelle Tracking in a Living Cell with Microsecond Time Resolution and Nanometer Spatial Precision. *Chemphyschem* **2008,** 9, 707-712.

62. Levi, V.; Ruan, Q. Q.; Gratton, E., 3-D Particle Tracking in a Two-Photon Microscope: Application to the Study of Molecular Dynamics in Cells. *Biophys. J.* **2005,** 88, 2919-2928.

63. Park, S. J.; Gesquiere, A. J.; Yu, J.; Barbara, P. F., Charge Injection and Photooxidation of Single Conjugated Polymer Molecules. *J. Am. Chem. Soc.* **2004,** 126, 4116-4117.

64. Yan, M.; Rothberg, L. J.; Papadimitrakopoulos, F.; Galvin, M. E.; Miller, T. M., Defect Quenching of Conjugated Polymer Luminescence. *Phys. Rev. Lett.* **1994,** 73, 744-747.

65. Yu, J.; Song, N. W.; McNeill, J. D.; Barbara, P. F., Efficient Exciton Quenching by Hole Polarons in the Conjugated Polymer MEH-PPV. *Isr. J. Chem.* **2004,** 44, 127-132.

66. Dahan, M.; Laurence, T.; Pinaud, F.; Chemla, D. S.; Alivisatos, A. P.; Sauer, M.; Weiss, S., Time-Gated Biological Imaging by Use of Colloidal Quantum Dots. *Opt. Lett.* **2001,** 26, 825-827.

67. Grey, J. K.; Kim, D. Y.; Norris, B. C.; Miller, W. L.; Barbara, P. F., Size-Dependent Spectroscopic Properties of Conjugated Polymer Nanoparticles. *J. Phys. Chem. B* **2006,** 110, 25568-25572.

68. Wu, C.; Szymanski, C.; Cain, Z.; McNeill, J., Conjugated Polymer Dots for Multiphoton Fluorescence Imaging. *J. Am. Chem. Soc.* **2007,** 129, 12904-12905.

69. Hohng, S.; Ha, T., Near-Complete Suppression of Quantum Dot Blinking in Ambient Conditions. *J. Am. Chem. Soc.* **2004,** 126, 1324-1325.

70. Kumar, P.; Lee, T. H.; Mehta, A.; Sumpter, B. G.; Dickson, R. M.; Barnes, M. D., Photon Antibunching from Oriented Semiconducting Polymer Nanostructures. *J. Am. Chem. Soc.* **2004,** 126, 3376-3377.

71. Hollars, C. W.; Lane, S. M.; Huser, T., Controlled Non-Classical Photon Emission from Single Conjugated Polymer Molecules. *Chem. Phys. Lett.* **2003,** 370, 393-398.

72. McNeill, J. D.; Barbara, P. F., Nsom Investigation of Carrier Generation, Recombination, and Drift in a Conjugated Polymer. *J. Phys. Chem. B* **2002,** 106, 4632-4639.

73. Gesquiere, A. J.; Park, S. J.; Barbara, P. F., Hole-Induced Quenching of Triplet and Singlet Excitons in Conjugated Polymers. *J. Am. Chem. Soc.* **2005,** 127, 9556-9560.

74. Yu, J.; Hu, D. H.; Barbara, P. F., Unmasking Electronic Energy Transfer of Conjugated Polymers by Suppression of O-2 Quenching. *Science* **2000,** 289, 1327-1330.

75. Jaiswal, J. K.; Mattoussi, H.; Mauro, J. M.; Simon, S. M., Long-Term Multiple Color Imaging of Live Cells Using Quantum Dot Bioconjugates. *Nat. Biotechnol.* **2003,** 21, 47-51.

76. Derfus, A. M.; Chan, W. C. W.; Bhatia, S. N., Intracellular Delivery of Quantum Dots for Live Cell Labeling and Organelle Tracking. *Adv. Mater.* **2004,** 16, 961-966.

77. Alivisatos, A. P.; Gu, W. W.; Larabell, C., Quantum Dots as Cellular Probes. *Annu. Rev. Biomed. Eng.* **2005,** 7, 55-76.

78. Ow, H.; Larson, D. R.; Srivastava, M.; Baird, B. A.; Webb, W. W.; Wiesner, U., Bright and Stable Core-Shell Fluorescent Silica Nanoparticles. *Nano Lett.* **2005,** 5, 113-117.

79. Wang, L.; Yang, C. Y.; Tan, W. H., Dual-Luminophore-Doped Silica Nanoparticles for Multiplexed Signaling. *Nano Lett.* **2005,** 5, 37-43.

80. Graf, C.; van Blaaderen, A., Metallodielectric Colloidal Core-Shell Particles for Photonic Applications. *Langmuir* **2002,** 18, 524-534.

81. Liz-Marzan, L. M.; Giersig, M.; Mulvaney, P., Synthesis of Nanosized Gold-Silica Core-Shell Particles. *Langmuir* **1996,** 12, 4329-4335.

82. Das, S.; Jain, T. K.; Maitra, A., Inorganic-Organic Hybrid Nanoparticles from N-Octyl Triethoxy Silane. *J. Coll. Int. Sci.* **2002,** 252, 82-88.

83. Enüstün, B. V.; Turkevich, J., Coagulation of Colloidal Gold. *J. Am. Chem. Soc.* **1963,** 85, 3317-3328.

84. Oldenburg, S. J.; Averitt, R. D.; Westcott, S. L.; Halas, N. J., Nanoengineering of Optical Resonances. *Chem. Phys. Lett.* **1998,** 288, 243-247.

85. Denk, W.; Strickler, J. H.; Webb, W. W., 2-Photon Laser Scanning Fluorescence Microscopy. *Science* **1990,** 248, 73-76.

86. Xu, C.; Zipfel, W.; Shear, J. B.; Williams, R. M.; Webb, W. W., Multiphoton Fluorescence Excitation: New Spectral Windows for Biological Nonlinear Microscopy. *Proc. Natl. Acad. Sci. USA* **1996,** 93, 10763-10768.

87. Bhawalkar, J. D.; He, G. S.; Prasad, P. N., Nonlinear Multiphoton Processes in Organic and Polymeric Materials. *Rep. Prog. Phys.* **1996,** 59, 1041-1070.

88. Zipfel, W. R.; Williams, R. M.; Webb, W. W., Nonlinear Magic: Multiphoton Microscopy in the Biosciences. *Nat. Biotechnol.* **2003,** 21, 1368-1376.

89. So, P. T. C.; Dong, C. Y.; Masters, B. R.; Berland, K. M., Two-Photon Excitation Fluorescence Microscopy. *Annu. Rev. Biomed. Eng.* **2000,** 2, 399-429.

90. Albota, M.; Beljonne, D.; Bredas, J. L.; Ehrlich, J. E.; Fu, J. Y.; Heikal, A. A.; Hess, S. E.; Kogej, T.; Levin, M. D.; Marder, S. R.; McCord-Maughon, D.; Perry, J. W.; Rockel, H.; Rumi, M.; Subramaniam, C.; Webb, W. W.; Wu, X. L.; Xu, C., Design of Organic Molecules with Large Two-Photon Absorption Cross Sections. *Science* **1998,** 281, 1653-1656.

91. Wang, H. F.; Huff, T. B.; Zweifel, D. A.; He, W.; Low, P. S.; Wei, A.; Cheng, J. X., In Vitro and in Vivo Two-Photon Luminescence Imaging of Single Gold Nanorods. *Proc. Natl. Acad. Sci. USA* **2005,** 102, 15752-15756.

92. Larson, D. R.; Zipfel, W. R.; Williams, R. M.; Clark, S. W.; Bruchez, M. P.; Wise, F. W.; Webb, W. W., Water-Soluble Quantum Dots for Multiphoton Fluorescence Imaging in Vivo. *Science* **2003,** 300, 1434-1436.

93. Oliveira, S. L.; Correa, D. S.; De Boni, L.; Misoguti, L.; Zilio, S. C.; Mendonca, C. R., Two-Photon Absorption Cross-Section Spectrum of a Pi-Conjugated Polymer Obtained Using the White-Light Continuum Z-Scan Technique. *Appl. Phys. Lett.* **2006,** 88, 021911.

94. Rumi, M.; Ehrlich, J. E.; Heikal, A. A.; Perry, J. W.; Barlow, S.; Hu, Z. Y.; McCord-Maughon, D.; Parker, T. C.; Rockel, H.; Thayumanavan, S.; Marder, S. R.; Beljonne, D.; Bredas, J. L., Structure-Property Relationships for Two-Photon Absorbing Chromophores: Bis-Donor Diphenylpolyene and Bis(Styryl)Benzene Derivatives. *J. Am. Chem. Soc.* **2000,** 122, 9500-9510.

95. Sanchez, E. J.; Novotny, L.; Holtom, G. R.; Xie, X. S., Room-Temperature Fluorescence Imaging and Spectroscopy of Single Molecules by Two-Photon Excitation. *J. Phys. Chem. A* **1997,** 101, 7019-7023.

96. Vanden Bout, D. A.; Yip, W. T.; Hu, D. H.; Fu, D. K.; Swager, T. M.; Barbara, P. F., Discrete Intensity Jumps and Intramolecular Electronic Energy Transfer in the Spectroscopy of Single Conjugated Polymer Molecules. *Science* **1997,** 277, 1074-1077.

97. Hu, D. H.; Yu, J.; Barbara, P. F., Single-Molecule Spectroscopy of Conjugated Polymer Meh-Ppv. *J. Am. Chem. Soc.* **1999,** 121, 6936-6937.

98. Yu, Z. H.; Barbara, P. F., Low-Temperature Single-Molecule Spectroscopy of Meh-Ppv Conjugated Polymer Molecules. *J. Phys. Chem. B* **2004,** 108, 11321-11326.

99. Barbara, P. F.; Gesquiere, A. J.; Park, S. J.; Lee, Y. J., Single-Molecule Spectroscopy of Conjugated Polymers. *Acc. Chem. Res.* **2005,** 38, 602-610.

100. Jonkheijm, P.; Miura, A.; Zdanowska, M.; Hoeben, F. J. M.; De Feyter, S.; Schenning, A. P. H. J.; De Schryver, F. C.; Meijer, E. W., Pi-Conjugated Oligo-(P-Phenylenevinylene) Rosettes and Their Tubular Self-Assembly. *Angew. Chem. Int. Edi.* **2004,** 43, 74-78.

101. Spano, F. C., Modeling Disorder in Polymer Aggregates: The Optical Spectroscopy of Regioregular Poly(3-Hexylthiophene) Thin Films. *J. Chem. Phys.* **2005,** 122, 234701.

102. Medintz, I. L.; Uyeda, H. T.; Goldman, E. R.; Mattoussi, H., Quantum Dot Bioconjugates for Imaging, Labelling and Sensing. *Nat. Mater.* **2005,** 4, 435-446.

103. Clapp, A. R.; Medintz, I. L.; Fisher, B. R.; Anderson, G. P.; Mattoussi, H., Can Luminescent Quantum Dots Be Efficient Energy Acceptors with Organic Dye Donors? *J. Am. Chem. Soc.* **2005,** 127, 1242-1250.

104. Lu, L. D.; Helgeson, R.; Jones, R. M.; McBranch, D.; Whitten, D., Superquenching in Cyanine Pendant Poly(L-Lysine) Dyes: Dependence on Molecular Weight, Solvent, and Aggregation. *J. Am. Chem. Soc.* **2002,** 124, 483-488.

105. Jones, R. M.; Lu, L. D.; Helgeson, R.; Bergstedt, T. S.; McBranch, D. W.; Whitten, D. G., Building Highly Sensitive Dye Assemblies for Biosensing from Molecular Building Blocks. *Proc. Natl. Acad. Sci. USA* **2001,** 98, 14769-14772.

106. Wu, C.; Peng, H.; Jiang, Y.; McNeill, J., Energy Transfer Mediated Fluorescence from Blended Conjugated Polymer Nanoparticles. *J. Phys. Chem. B* **2006,** 110, 14148-14154.

107. Waner, M. J.; Gilchrist, M.; Schindler, M.; Dantus, M., Imaging the Molecular Dimensions and Oligomerization of Proteins at Liquid/Solid Interfaces. *J. Phys. Chem. B* **1998,** 102, 1649-1657.

108. Yang, Z. Q.; Huck, W. T. S.; Clarke, S. M.; Tajbakhsh, A. R.; Terentjev, E. M., Shape-Memory Nanoparticles from Inherently Non-Spherical Polymer Colloids. *Nat. Mater.* **2005,** 4, 486-490.

109. Chen, L. C.; Roman, L. S.; Johansson, D. M.; Svensson, M.; Andersson, M. R.; Janssen, R. A. J.; Inganas, O., Excitation Transfer in Polymer Photodiodes for Enhanced Quantum Efficiency. *Adv. Mater.* **2000,** 12, 1110-1114.

110. Xu, Q. F.; Duong, H. M.; Wudl, F.; Yang, Y., Efficient Single-Layer "Twistacene"-Doped Polymer White Light-Emitting Diodes. *Appl. Phys. Lett.* **2004,** 85, 3357-3359.

111. Gong, X.; Wang, S.; Moses, D.; Bazan, G. C.; Heeger, A. J., Multilayer Polymer Light-Emitting Diodes: White-Light Emission with High Efficiency. *Adv. Mater.* **2005,** 17, 2053-2058.

112. Gong, X.; Ostrowski, J. C.; Bazan, G. C.; Moses, D.; Heeger, A. J.; Liu, M. S.; Jen, A. K. Y., Electrophosphorescence from a Conjugated Copolymer Doped with an Iridium Complex: High Brightness and Improved Operational Stability. *Adv. Mater*. **2003,** 15, 45-49.

113. Babel, A.; Li, D.; Xia, Y. N.; Jenekhe, S. A., Electrospun Nanofibers of Blends of Conjugated Polymers: Morphology, Optical Properties, and Field-Effect Transistors. *Macromol.* **2005,** 38, 4705-4711.

114. Collison, C. J.; Rothberg, L. J.; Treemaneekarn, V.; Li, Y., Conformational Effects on the Photophysics of Conjugated Polymers: A Two Species Model for Meh-Ppv Spectroscopy and Dynamics. *Macromol.* **2001,** 34, 2346-2352.

115. Padmanaban, G.; Ramakrishnan, S., Conjugation Length Control in Soluble Poly[2-Methoxy-5-(-2'-Ethylhexyl)Oxy-1,4-Phenylene-Vinylene] (MEH-PPV): Synthesis, Optical Properties, and Energy Migration. *J. Am. Chem. Soc.* **2000,** 122, 2244-2251.

116. Scherf, U.; List, E. J. W., Semiconducting Polyfluorenes - Towards Reliable Structure-Property Relationships. *Adv. Mater.* **2002,** 14, 477-487.

117. Yang, X. H.; Jaiser, F.; Neher, D.; Lawson, P. V.; Bredas, J. L.; Zojer, E.; Guntner, R.; de Freitas, P. S.; Forster, M.; Scherf, U., Suppression of the Keto-Emission in Polyfluorene Light-Emitting Diodes: Experiments and Models. *Adv. Funct. Mater.* **2004,** 14, 1097-1104.

118. Lakowicz, J. R.; Gryczynski, I.; Gryczynski, Z.; Murphy, C. J., Luminescence Spectral Properties of CdS Nanoparticles. *J. Phys. Chem. B* **1999,** 103, 7613-7620.

119. Dexter, D. L., A Theory of Sensitized Luminescence in Solids. *J. Chem. Phys.* **1953,** 21, 836-850.

120. Turro, N. J.; Yekta, A., Luminescent Probes for Detergent Solutions:A Simple Procedure for Determination of the Mean Aggregation Number of Micelles. *J. Am. Chem. Soc.* **1978,** 100, 5951 - 5952.

121. Lu, L. D.; Jones, R. M.; McBranch, D.; Whitten, D., Surface-Enhanced Superquenching of Cyanine Dyes as J-Aggregates on Laponite Clay Nanoparticles. *Langmuir* **2002,** 18, 7706-7713.

122. Xu, Q. H.; Gaylord, B. S.; Wang, S.; Bazan, G. C.; Moses, D.; Heeger, A. J., Time-Resolved Energy Transfer in DNA Sequence Detection Using Water-Soluble Conjugated Polymers: The Role of Electrostatic and Hydrophobic Interactions. *Proc. Natl. Acad. Sci. USA* **2004,** 101, 11634-11639.

123. Kumaraswamy, S.; Bergstedt, T.; Shi, X. B.; Rininsland, F.; Kushon, S.; Xia, W. S.; Ley, K.; Achyuthan, K.; McBranch, D.; Whitten, D., Fluorescent-Conjugated Polymer Superquenching Facilitates Highly Sensitive Detection of Proteases. *Proc. Natl. Acad. Sci. USA* **2004,** 101, 7511-7515.

124. Pinto, M. R.; Schanze, K. S., Amplified Fluorescence Sensing of Protease Activity with Conjugated Polyelectrolytes. *Proc. Natl. Acad. Sci. USA* **2004,** 101, 7505-7510.

125. Campillo, A. J.; Shapiro, S. L.; Swenberg, C. E., Picosecond Measurements of Exciton Migration in Tetracene Crystals Doped with Pentacene. *Chem. Phys. Lett.* **1977,** 52, 11-15.

126. McNeill, J. D.; Kim, D. Y.; Barbara, P. F., Near Field Scanning Optical Microscopy Investigations of Energy Transfer and Charge Trapping in Doped Tetracene. *J. Phys. Chem. B* **2004,** 108, 11368-11374.

127. Halls, J. J. M.; Pichler, K.; Moratti, S. C.; Holmes, A. B., Exciton Diffusion and Dissociation in a Poly-(P-Phenylenevinylene)/C_{60} Heterojunction Photovoltaic Cell. *Appl. Phys. Lett.* **1996,** 68, 3120-3122.

128. Jones, G.; Jackson, W. R.; Choi, C.; Bergmark, W. R., Solvent Effects on Emission Yield and Lifetime for Coumarin Laser-Dyes - Requirements for a Rotatory Decay Mechanism. *J. Phys. Chem.* **1985,** 89, 294-300.

129. Chan, W. C. W.; Nie, S. M., Quantum Dot Bioconjugates for Ultrasensitive Nonisotopic Detection. *Science* **1998,** 281, 2016-2018.

130. Ego, C.; Marsitzky, D.; Becker, S.; Zhang, J. Y.; Grimsdale, A. C.; Mullen, K.; MacKenzie, J. D.; Silva, C.; Friend, R. H., Attaching Perylene Dyes to Polyfluorene: Three Simple, Efficient Methods for Facile Color Tuning of Light-Emitting Polymers. *J. Am. Chem. Soc.* **2003,** 125, 437-443.

131. Tong, A. K.; Li, Z. M.; Jones, G. S.; Russo, J. J.; Ju, J. Y., Combinatorial Fluorescence Energy Transfer Tags for Multiplex Biological Assays. *Nat. Biotechnol.* **2001,** 19, 756-759.

132. Wang, L.; Tan, W., Multicolor Fret Silica Nanoparticles by Sinlge Wavelength Excitation. *Nano Lett.* **2006,** 6, 84-88.

133. Morris, V. J.; Kirby, A. R.; Gunning, A. P., *Atomic Force Microscopy for Biologists*. Imperial College Press: London, 1999.

134. Virgili, T.; Lidzey, D. G.; Bradley, D. D. C., Efficient Energy Transfer from Blue to Red in Tetraphenylporphyrin-Doped Poly(9,9-Dioctylfluorene) Light-Emitting Diodes. *Adv. Mater.* **2000,** 12, 58-62.

135. Cabanillas-Gonzalez, J.; Fox, A. M.; Hill, J.; Bradley, D. D. C., Model for Energy Transfer in Polymer/Dye Blends Based on Point-Surface Dipole Interaction. *Chem. Mater.* **2004,** 16, 4705-4710.

136. Lyons, B. P.; Wong, K. S.; Monkman, A. P., Study of the Energy Transfer Processes in Polyfluorene Doped with Tetraphenyl Porphyrin. *J. Chem. Phys.* **2003,** 118, 4707-4711.

137. Pschenitzka, F.; Sturm, J. C., Three-Color Organic Light-Emitting Diodes Patterned by Masked Dye Diffusion. *Appl. Phys. Lett.* **1999,** 74, 1913-1915.

138. Peng, A. D.; Xiao, D. B.; Ma, Y.; Yang, W. S.; Yao, J. N., Tunable Emission from Doped 1,3,5-Triphenyl-2-Pyrazoline Organic Nanoparticles. *Adv. Mater.* **2005,** 17, 2070-2073.

139. Zhong, G. Y.; He, J.; Zhang, S. T.; Xu, Z.; Xiong, Z. H.; Shi, H. Z.; Ding, X. M.; Huang, W.; Hou, X. Y., In Situ Photoluminescence Investigation of Doped Alq. *Appl. Phys. Lett.* **2002,** 80, 4846-4848.

140. Jakabovic, J.; Lengyel, O.; Kovac, J.; Wong, T. C.; Lee, C. S.; Lee, S. T., Properties of 4-Dicyanomethylene-2-Methyl-6-(P-Dimethyl-Aminostyryl)-4h-Pyran-Doped Alq Layers as Optically Pumped Lasers. *Appl. Phys. Lett.* **2003,** 83, 1295-1297.

141. Rettig, W.; Majenz, W., Competing Adiabatic Photoreaction Channels in Stilbene Derivatives. *Chem. Phys. Lett.* **1989,** 154, 335-341.

142. Becker, K.; Lupton, J. M., Efficient Light Harvesting in Dye-Endcapped Conjugated Polymers Probed by Single Molecule Spectroscopy. *J. Am. Chem. Soc.* **2006,** 128, 6468-6479.

143. Campoy-Quiles, M.; Heliotis, G.; Xia, R. D.; Ariu, M.; Pintani, M.; Etchegoin, P.; Bradley, D. D. C., Ellipsometric Characterization of the Optical Constants of Polyfluorene Gain Media. *Adv. Funct. Mater.* **2005,** 15, 925-933.

144. Lyons, B. P.; Monkman, A. P., The Role of Exciton Diffusion in Energy Transfer between Polyfluorene and Tetraphenyl Porphyrin. *Phys. Rev. B* **2005,** 71, 235201.

145. Markov, D. E.; Amsterdam, E.; Blom, P. W. M.; Sieval, A. B.; Hummelen, J. C., Accurate Measurement of the Exciton Diffusion Length in a Conjugated Polymer Using a Heterostructure with a Side-Chain Cross-Linked Fullerene Layer. *J. Phys. Chem. A* **2005,** 109, 5266-5274.

146. Rosenstock, H. B., Luminescent Emission from an Organic Solid with Traps. *Phys. Rev.* **1969,** 187, 1166-1168.

147. Powell, R. C.; Soos, Z. G., Generalized Random-Walk Model for Singlet-Exciton Energy Transfer. *Phys. Rev. B* **1972,** 6, 4035-4046.

148. Gamertsfelder, G. R.; Goldhaber, M., The Diffusion Length of C Neutrons in Water *Phys. Rev.* **1942,** 62, 556-557.

149. Stevens, M. A.; Silva, C.; Russell, D. M.; Friend, R. H., Exciton Dissociation Mechanisms in the Polymeric Semiconductors Poly(9,9-Dioctylfluorene) and Poly(9, 9-Dioctylfluorene-Co-Benzothiadiazole). *Phys. Rev. B* **2001,** 63, 165213.

150. Haugeneder, A.; Neges, M.; Kallinger, C.; Spirkl, W.; Lemmer, U.; Feldmann, J.; Scherf, U.; Harth, E.; Gugel, A.; Mullen, K., Exciton Diffusion and Dissociation in Conjugated Polymer Fullerene Blends and Heterostructures. *Phys. Rev. B* **1999,** 59, 15346-15351.

151. Herz, L. M.; Silva, C.; Grimsdale, A. C.; Mullen, K.; Phillips, R. T., Time-Dependent Energy Transfer Rates in a Conjugated Polymer Guest-Host System. *Phys. Rev. B* **2004,** 70, 165207.

152. List, E. J. W.; Guentner, R.; de Freitas, P. S.; Scherf, U., The Effect of Keto Defect Sites on the Emission Properties of Polyfluorene-Type Materials. *Adv. Mater.* **2002,** 14, 374-378.

153. Ariu, M.; Lidzey, D. G.; Sims, M.; Cadby, A. J.; Lane, P. A.; Bradley, D. D. C., The Effect of Morphology on the Temperature-Dependent Photoluminescence Quantum Efficiency of the Conjugated Polymer Poly(9, 9-Dioctylfluorene). *J. Phys: Condens. Matter* **2002,** 14, 9975-9986.

154. Widengren, J.; Rigler, R., Mechanisms of Photobleaching Investigated by Fluorescence Correlation Spectroscopy. *Bioimaging* **1996,** 4, 149-157.

155. Kulzer, F.; Orrit, M., Single-Molecule Optics. *Annu. Rev. Phys. Chem.* **2004,** 55, 585-611.

156. Zondervan, R.; Kulzer, F.; Kol'chenko, M. A.; Orrit, M., Photobleaching of Rhodamine 6g in Poly(Vinyl Alcohol) at the Ensemble and Single-Molecule Levels. *J. Phys. Chem. A* **2004,** 108, 1657-1665.

157. Schindler, F.; Lupton, J. M.; Feldmann, J.; Scherf, U., Controlled Fluorescence Bursts from Conjugated Polymers Induced by Triplet Quenching. *Adv. Mater.* **2004,** 16, 653-657.

158. Grell, M.; Bradley, D. D. C.; Ungar, G.; Hill, J.; Whitehead, K. S., Interplay of Physical Structure and Photophysics for a Liquid Crystalline Polyfluorene. *Macromol.*. **1999,** 32, 5810-5817.

159. Cadby, A. J.; Lane, P. A.; Mellor, H.; Martin, S. J.; Grell, M.; Giebeler, C.; Bradley, D. D. C.; Wohlgenannt, M.; An, C.; Vardeny, Z. V., Film Morphology and Photophysics of Polyfluorene. *Phys. Rev. B* **2000,** 62, 15604-15609.

160. Khan, A. L. T.; Sreearunothai, P.; Herz, L. M.; Banach, M. J.; Kohler, A., Morphology-Dependent Energy Transfer within Polyfluorene Thin Films. *Phys. Rev. B* **2004,** 69, 085201.

161. Hayer, A.; Khan, A. L. T.; Friend, R. H.; Kohler, A., Morphology Dependence of the Triplet Excited State Formation and Absorption in Polyfluorene. *Phys. Rev. B* **2005,** 71, 241302.

162. Grell, M.; Bradley, D. D. C.; Long, X.; Chamberlain, T.; Inbasekaran, M.; Woo, E. P.; Soliman, M., Chain Geometry, Solution Aggregation and Enhanced Dichroism in the Liquid-Crystalline Conjugated Polymer Poly(9,9-Dioctylfluorene). *Acta Polymerica* **1998,** 49, 439-444.

163. Grell, M.; Bradley, D. D. C.; Inbasekaran, M.; Woo, E. P., A Glass-Forming Conjugated Main-Chain Liquid Crystal Polymer for Polarized Electroluminescence Applications. *Adv. Mater.* **1997,** 9, 798-802.

164. Caruso, M. E.; Anni, M., Real-Time Investigation of Solvent Swelling Induced Beta-Phase Formation in Poly(9,9-Dioctylfluorene). *Phys. Rev. B* **2007,** 76, 054207.

165. List, E. J. W.; Kim, C. H.; Naik, A. K.; Scherf, U.; Leising, G.; Graupner, W.; Shinar, J., Interaction of Singlet Excitons with Polarons in Wide Band-Gap Organic Semiconductors: A Quantitative Study. *Phys. Rev. B* **2001,** 6415, 155204.

166. Dias, F. B.; Morgado, J.; Macanita, A. L.; da Costa, F. P.; Burrows, H. D.; Monkman, A. P., Kinetics and Thermodynamics of Poly(9,9-Dioctylfluorene) Beta-Phase Formation in Dilute Solution. *Macromol.* **2006,** 39, 5854-5864.

167. Knaapila, M.; Garamus, V. M.; Dias, F. B.; Almasy, L.; Galbrecht, F.; Charas, A.; Morgado, J.; Burrows, H. D.; Scherf, U.; Monkman, A. P., Influence of Solvent Quality on the Self-Organization of Archetypical Hairy Rods - Branched and Linear Side Chain Polyfluorenes: Rodlike Chains Versus "Beta-Sheets" In Solution. *Macromol.* **2006,** 39, 6505-6512.

168. Teetsov, J. A.; Vanden Bout, D. A., Imaging Molecular and Nanoscale Order in Conjugated Polymer Thin Films with near-Field Scanning Optical Microscopy. *J. Am. Chem. Soc.* **2001,** 123, 3605-3606.

169. Ariu, M.; Sims, M.; Rahn, M. D.; Hill, J.; Fox, A. M.; Lidzey, D. G.; Oda, M.; Cabanillas-Gonzalez, J.; Bradley, D. D. C., Exciton Migration in Beta-Phase Poly(9,9-Dioctylfluorene). *Phys. Rev. B* **2003,** 67, 195333.

170. Manas, E. S.; Spano, F. C., Absorption and Spontaneous Emission in Aggregates of Conjugated Polymers. *J. Chem. Phys.* **1998,** 109, 8087-8101.

171. Hernando, J.; van Dijk, E. M. H. P.; Hoogenboom, J. P.; Garcia-Lopez, J. J.; Reinhoudt, D. N.; Crego-Calama, M.; Garcia-Parajo, M. F.; van Hulst, N. F., Effect of Disorder on Ultrafast Exciton Dynamics Probed by Single Molecule Spectroscopy. *Phys. Rev. Lett.* **2006,** 97, 216403.

172. Long, X.; Malinowski, A.; Bradley, D. D. C.; Inbasekaran, M.; Woo, E. P., Emission Processes in Conjugated Polymer Solutions and Thin Films. *Chem. Phys. Lett.* **1997,** 272, 6-12.

173. Acker, T.; Acker, H., Cellular Oxygen Sensing Need in Cns Function: Physiological and Pathological Implications. *J. Exp. Biol.* **2004,** 207, 3171-3188.

174. Lopez-Barneo, J.; Pardal, R.; Ortega-Saenz, P., Cellular Mechanisms of Oxygen Sensing. *Annu. Rev. Physiol.* **2001,** 63, 259-287.

175. Ikeda, E., Cellular Response to Tissue Hypoxia and Its Involvement in Disease Progression. *Pathol. Int.* **2005,** 55, 603-610.

176. Hockel, M.; Schlenger, K.; Hockel, S.; Aral, B.; Schaffer, U.; Vaupel, P., Tumor Hypoxia in Pelvic Recurrences of Cervical Cancer. *Int. J. Cancer* **1998,** 79, 365-369.

177. Carmeliet, P.; Dor, Y.; Herbert, J. M.; Fukumura, D.; Brusselmans, K.; Dewerchin, M.; Neeman, M.; Bono, F.; Abramovitch, R.; Maxwell, P.; Koch, C. J.; Ratcliffe, P.; Moons, L.; Jain, R. K.; Collen, D.; Keshet, E., Role of Hif-1 Alpha or in Hypoxia-Mediated Apoptosis, Cell Proliferation and Tumour Angiogenesis. *Nature* **1998,** 394, 485-490.

178. Frank, R. N., Diabetic Retinopathy. *New Engl. J. Med.* **2004,** 350, 48-58.

179. Distler, J. H. W.; Wenger, R. H.; Gassmann, M.; Kurowska, M.; Hirth, A.; Gay, S.; Distler, O., Physiologic Responses to Hypoxia and Implications for Hypoxia-Inducible Factors in the Pathogenesis of Rheumatoid Arthritis. *Arthritis. Rheum.* **2004,** 50, 10-23.

180. Demas, J. N.; Degraff, B. A., Design and Applications of Highly Luminescent Transition-Metal Complexes. *Anal. Chem.* **1991,** 63, A829-A837.

181. Preininger, C.; Klimant, I.; Wolfbeis, O. S., Optical-Fiber Sensor for Biological Oxygen-Demand. *Anal. Chem.* **1994,** 66, 1841-1846.

182. Rosenzweig, Z.; Kopelman, R., Development of a Submicrometer Optical-Fiber Oxygen Sensor. *Anal. Chem.* **1995,** 67, 2650-2654.

183. McDonagh, C.; MacCraith, B. D.; McEvoy, A. K., Tailoring of Sol-Gel Films for Optical Sensing of Oxygen in Gas and Aqueous Phase. *Anal. Chem.* **1998,** 70, 45-50.

184. Koo, Y. E. L.; Cao, Y. F.; Kopelman, R.; Koo, S. M.; Brasuel, M.; Philbert, M. A., Real-Time Measurements of Dissolved Oxygen inside Live Cells by Organically Modified Silicate Fluorescent Nanosensors. *Anal. Chem.* **2004,** 76, 2498-2505.

185. Xu, H.; Aylott, J. W.; Kopelman, R.; Miller, T. J.; Philbert, M. A., A Real-Time Ratiometric Method for the Determination of Molecular Oxygen inside Living Cells Using Sol-Gel-Based Spherical Optical Nanosensors with Applications to Rat C6 Glioma. *Anal. Chem.* **2001,** 73, 4124-4133.

186. Rumsey, W. L.; Vanderkooi, J. M.; Wilson, D. F., Imaging of Phosphorescence - a Novel Method for Measuring Oxygen Distribution in Perfused Tissue. *Science* **1988,** 241, 1649-1651.

187. Vinogradov, S. A.; Lo, L. W.; Jenkins, W. T.; Evans, S. M.; Koch, C.; Wilson, D. F., Noninvasive Imaging of the Distribution in Oxygen in Tissue in Vivo Using near-Infrared Phosphors. *Biophys. J.* **1996,** 70, 1609-1617.

188. Carraway, E. R.; Demas, J. N.; Degraff, B. A.; Bacon, J. R., Photophysics and Photochemistry of Oxygen Sensors Based on Luminescent Transition-Metal Complexes. *Anal. Chem.* **1991,** 63, 337-342.

189. Mills, A.; Lepre, A., Controlling the Response Characteristics of Luminescent Porphyrin Plastic Film Sensors for Oxygen. *Anal. Chem.* **1997,** 69, 4653-4659.

190. Borisov, S. M.; Klimant, I., Ultrabright Oxygen Optodes Based on Cyclometalated Lridium(Iii) Coumarin Complexes. *Anal. Chem.* **2007,** 79, 7501-7509.

191. Zhang, G.; Chen, J.; Payne, S. J.; Kooi, S. E.; Demas, J. N.; Fraser, C. L., Multi-Emissive Difluoroboron Dibenzoylmethane Polylactide Exhibiting Intense Fluorescence and Oxygen-Sensitive Room-Temperature Phosphorescence. *J. Am. Chem. Soc.* **2007,** 129, 8942-8243.

192. Brinas, R. P.; Troxler, T.; Hochstrasser, R. M.; Vinogradov, S. A., Phosphorescent Oxygen Sensor with Dendritic Protection and Two-Photon Absorbing Antenna. *J. Am. Chem. Soc.* **2005,** 127, 11851-11862.

193. Lane, P. A.; Palilis, L. C.; O'Brien, D. F.; Giebeler, C.; Cadby, A. J.; Lidzey, D. G.; Campbell, A. J.; Blau, W.; Bradley, D. D. C., Origin of Electrophosphorescence from a Doped Polymer Light Emitting Diode. *Phys. Rev. B* **2001,** 63, 235206.

194. Baldo, M. A.; O'Brien, D. F.; You, Y.; Shoustikov, A.; Sibley, S.; Thompson, M. E.; Forrest, S. R., Highly Efficient Phosphorescent Emission from Organic Electroluminescent Devices. *Nature* **1998,** 395, 151-154.

195. Mei, E. W.; Vinogradov, S.; Hochstrasser, R. M., Direct Observation of Triplet State Emission of Single Molecules: Single Molecule Phosphorescence Quenching of Metalloporphyrin and Organometallic Complexes by Molecular Oxygen and Their Quenching Rate Distributions. *J. Am. Chem. Soc.* **2003,** 125, 13198-13204.

196. Vacha, M.; Koide, Y.; Kotani, M.; Sato, H., Single Molecule Detection and Photobleaching Study of a Phosphorescent Dye: Organometallic Iridium(Iii) Complex. *Chem. Phys. Lett.* **2004,** 388, 263-268.

197. Hu, D. H.; Lu, H. P., Single-Molecule Triplet-State Photon Antibunching at Room Temperature. *J. Phys. Chem. B* **2005,** 109, 9861-9864.

198. Pratten, M. K.; Lloyd, J. B., Pinocytosis and Phagocytosis - the Effect of Size of a Particulate Substrate on Its Mode of Capture by Rat Peritoneal-Macrophages Cultured Invitro. *Biochim. Biophys. Acta* **1986,** 881, 307-313.